================= **PHYSICS** =================

On Sound Propagation in a Nonstationary Ocean

O. A. Godin

Presented by Academician L.M. Brekhovskikh March 28, 2002

Received March 28, 2002

Properties of the ocean considered as an acoustic medium vary over a wide range of spatial and temporal scales. Both the position and shape of ocean boundaries, as well as the speed of sound c and the flow velocity $\mathbf{u}$, vary in time under the action of tides, surface and internal waves, mesoscale vortices, and other hydrophysical processes. When numerically simulating the sound propagation in a medium, its unsteadiness is usually disregarded, because the relative changes ε of its parameters are small for time intervals on the order of the sound-propagation time [1, 2]. Although effects caused by the nonstationarity are small compared to nonuniformity effects, the allowance for the unsteadiness becomes necessary in applications based on the reciprocity principle of sound fields in quiescent stationary media, as well as in the case of sufficiently large lengths of the ray paths. The tomographic reconstruction of a flow-velocity field by the method of reciprocal transmission of sound [3, 4] and the time-reversal mirror [5, 6] are the most topical examples of such applications.

In this paper, we substantiate the quasi-stationary approximation suggested in [7], which is a simple method allowing us to describe the effect of the nonstationarity on sound fields using well-developed mathematical models of sound propagation in nonuniform stationary fluids. We consider the quasi-stationary approximation only as applied to ocean acoustics even though similar problems arise also in atmospheric acoustics and in ultrasound technology of measuring flow velocities.

The propagation of short waves in a medium whose parameters smoothly vary with time can be considered in the ray approximation [8] and requires that space–time rays between a source and a receiver be found in the four-dimensional space (x, y, z, t). A similar description in terms of normal modes is possible in the case of weakly interacting modes [9] when the space–time rays for the modes should be found in three-dimensional space (x, y, t). In both cases, the dimensionality of a

nonstationary problem to be solved exceeds by unity that of a stationary problem. This leads to a considerable increase in the amount of calculations required. In the weak-nonstationarity limit ($\varepsilon \longrightarrow 0$), it is sufficient to allow for only phase terms on the order of $O(\varepsilon)$ which accumulate with the distance, while corrections proportional to ε can be ignored in the mode amplitudes and in the field amplitudes along the rays. As is shown below, dominant terms of the expansion in powers of ε can be found analytically without evaluating the space–time rays numerically.

We now consider for definiteness the multimode propagation in a horizontal, nonuniform, and nonstationary waveguide in the presence of a flow. In the approximation of vertical modes and horizontal rays, the acoustic pressure acquires the form

$$p = \sum_n A^{(n)}(\mathbf{r}, z, t)\exp(i\psi^{(n)}(\mathbf{r}, t)), \qquad (1)$$

where the sum is taken over the mode orders and the phases satisfy the eikonal equation

$$k = \xi_n(\omega, \alpha; \mathbf{r}, t), \quad \mathbf{k} = \nabla\psi^{(n)},$$
$$\omega = -\frac{\partial\psi^{(n)}}{\partial t}. \qquad (2)$$

The local-mode propagation constants ξ_n are considered as given functions of the horizontal vector $\mathbf{r} = (x, y, 0)$, time t, frequency ω, and direction of the wave vector $\mathbf{k} = k(\cos\alpha, \sin\alpha, 0)$. Here, $\xi_n = \xi_{n0}(\omega, \alpha; \mathbf{r}) + \mu_n(\omega, \alpha; \mathbf{r}, t)$, where ξ_{n0} and μ_n are propagation constants for a corresponding stationary medium and their time-dependent perturbances, respectively. Introducing the Hamiltonian $H(\mathbf{k}, \omega; \mathbf{r}, t) = 0.5(k^2 - \xi_n^2)$, we obtain from Eqs. (2) the ray equations (cf. the steady case [10, Sect. 7.3])

$$\frac{d\mathbf{r}}{d\tau} = \mathbf{k} + \frac{\partial\xi_n}{\partial\alpha}(\sin\alpha, -\cos\alpha, 0), \quad \frac{dt}{d\tau} = \xi_n\frac{\partial\xi_n}{\partial\omega},$$
$$\frac{d\mathbf{k}}{d\tau} = \xi_n\nabla\xi_n, \quad \frac{d\omega}{d\tau} = -\xi_n\frac{\partial\xi_n}{\partial t}. \qquad (3)$$

The parameter τ entering into Eqs. (3) determines a point on the space–time ray of a mode.

Shirshov Institute of Oceanology,
Russian Academy of Sciences,
ul. Krasikova 23, Moscow, 117557 Russia

Expanding both the phase and the azimuth angle entering into Eqs. (2) in power series of ε,

$$\psi^{(n)} = \psi_0 + \psi_1 + \dots, \quad \alpha = \alpha_0 + \alpha_1 + \dots \,,$$

we arrive at

$$(\nabla \psi_0)^2 = \xi_{n0}^2, \tag{4}$$

$$2\nabla \psi_0 \nabla \psi_1 = -\frac{\partial \xi_{n0}^2}{\partial \omega}\frac{\partial \psi_1}{\partial t}$$

$$+ \xi_{n0}^{-2}\frac{\partial \xi_{n0}^2}{\partial \alpha}\left(\frac{\partial \psi_1}{\partial y}\frac{\partial \psi_0}{\partial x} - \frac{\partial \psi_0}{\partial y}\frac{\partial \psi_1}{\partial x}\right) + 2\xi_{n0}\mu_n. \tag{5}$$

Here, ξ_{n0}, μ_n, and derivatives of ξ_{n0} are taken for $\omega = -\dfrac{\partial \psi_0}{\partial t}$ and $\alpha = \alpha_0$. With regard to Eqs. (3), Eq. (5) is reduced to

$$\frac{\partial \psi_1}{\partial \tau} = \xi_{n0}\mu_n\big|_{\omega = \omega_s, \, \alpha = \alpha_0(\tau), \, \mathbf{r} = \mathbf{r}_0(\tau), \, t = t_0(\tau)}. \tag{6}$$

The quantity $(\mathbf{r}_0(\tau), t_0(\tau))$ is a point on the unperturbed space–time ray, the derivative being taken along the unperturbed mode ray,

$$t_0 = t_s + \int_{\mathbf{r}_s}^{\mathbf{r}} dl\, \xi_{n0}\left[\xi_{n0}^2 + \left(\frac{\partial \xi_{n0}}{\partial \omega}\right)^2\right]^{-\frac{1}{2}}\frac{\partial \xi_{n0}}{\partial \omega}, \tag{7}$$

t_s is the time of the signal emission, and $\omega_s = -\dfrac{\partial \psi_0}{\partial t}$ is the excitation frequency conserved along the unperturbed space–time ray. We then integrate along the coordinate projection of the unperturbed space–time ray (i.e., along the mode ray in the stationary limit) and use the well-known expression for the phase ψ_0 of the acoustic field excited by a stationary monochromatic source (see [10], Sect. 7.3). As a result, we have

$$\psi^{(n)}(\mathbf{r}, t) = \psi_0 + \psi_1 + O(\varepsilon^2)$$

$$= \int_{\mathbf{r}_s}^{\mathbf{r}} \xi_n \frac{\mathbf{k}_0}{k_0} d\mathbf{r} - \omega_s t + O(\varepsilon^2)$$

$$= \int_{\mathbf{r}_s}^{\mathbf{r}} dl\, \xi_n\left[1 + \xi_{n0}^{-2}\left(\frac{\partial \xi_{n0}}{\partial \alpha}\right)^2\right]^{-\frac{1}{2}} - \omega_s t + O(\varepsilon^2). \tag{8}$$

Here, $\mathbf{r}_s$ is the radius vector of the source and $\mathbf{k}_0 = \nabla \psi_0$ and $dl = |d\mathbf{r}|$ are the wave vector and the arc-length differential of the mode ray in the stationary waveguide, respectively.

In the quasi-stationary approximation, an auxiliary medium is introduced, with its parameters assumed to be independent of time and coincident with the corresponding parameters of the actual medium at an arbitrary moment of time $t = t_{\text{ret}}$. The phase of a mode is

evaluated as an integral (taken along the ray $\mathbf{r}_0(l)$ in the stationary medium) of the propagation constant of the mode, which is evaluated at the time $t_0(l)$ of the signal arrival at the point under consideration in the auxiliary medium [7]:

$$\psi_q^{(n)}(\mathbf{r}, t) = \int_{\mathbf{r}_s}^{\mathbf{r}} dl\left(\frac{dx_0}{dl}\cos\alpha_0 + \frac{dy_0}{dl}\sin\alpha_0\right)$$

$$\times \xi_n(\omega_s, \alpha_0(l); \mathbf{r}_0(l), t_0(l)) - \omega_s t. \tag{9}$$

Within the framework of perturbation theory, we choose an unperturbed medium such that it coincides with the auxiliary medium in the quasi-stationary approximation. In other words, we assume that $\xi_{n0}(\omega, \alpha; \mathbf{r}) = \xi_{n0}(\omega, \alpha; \mathbf{r}, t_{\text{ref}})$. As directly follows from the comparison of Eqs. (8) and (9), $\psi^{(n)} - \psi_q^{(n)} = O(\varepsilon^2)$; i.e., the quasi-stationary approximation yields a correct expression for the principal term of the phase disturbance, which is caused by the nonstationarity. However, this approximation does not allow us to correctly evaluate quadratic corrections. This can be easily verified in the case of straight-line mode rays when the problem is solved exactly.

With the instantaneous phase given, the frequency ω and the travel time T for a mode are determined from the relationships

$$\omega = -\frac{\partial \psi}{\partial t} \quad \text{and} \quad \frac{\partial[\psi^{(n)}(\mathbf{r}, t_s + T) - \psi^{(n)}(\mathbf{r}_s, t_s)]}{\partial \omega} = 0.$$

It follows from Eq. (9) in the quasi-stationary approximation that

$$\omega_q = \omega_s - \int_{\mathbf{r}_s}^{\mathbf{r}} dl\left(\frac{dx_0}{dl}\cos\alpha_0 + \frac{dy_0}{dl}\sin\alpha_0\right)$$

$$\times \frac{\partial \xi_n}{\partial t}(\omega_s, \alpha_0(l); \mathbf{r}_0(l), t_0(l)), \tag{10}$$

$$T_q = \frac{\partial}{\partial \omega_s}\int_{\mathbf{r}_s}^{\mathbf{r}} dl\left(\frac{dx_0}{dl}\cos\alpha_0 + \frac{dy_0}{dl}\sin\alpha_0\right)$$

$$\times \xi_n(\omega_s, \alpha_0(l); \mathbf{r}_0(l), t_0(l)). \tag{11}$$

Just as the phase, both the frequency and the travel time found in the quasi-stationary approximation differ from their exact values by terms on the order of $O(\varepsilon^2)$. It should be emphasized that in order to evaluate the quantities $\psi_q^{(n)}$, T_q, and ω_q, it is sufficient to find the mode rays between the source and the receiver only in the auxiliary stationary medium. Thus, in the case of an nonstationary medium, the quasi-stationary approximation allows dominant terms of the wave perturbed by the effect of nonstationarity to be found in quadratures without analyzing rays in the time-dependent medium. The result obtained is similar to the property of rays in

a stationary medium, which being well known is widely used in linear tomography [3]. Namely, to evaluate the travel time with an accuracy to the terms of the second order, it is sufficient to integrate the perturbed value of the slowness along an unperturbed ray.

We now compare the quasi-stationary approximation to the frozen-medium one. The validity of the latter is implied in most studies devoted to ocean acoustics. In this approximation, the medium is considered invariable (frozen) during the propagation of an acoustic signal. The corresponding expression for the mode phase is obtained by substituting t_{ref} for $t_0(l)$ in Eq. (9). This result differs from $\psi_{\mathrm{q}}^{(n)}$ and, therefore, from the exact phase value $\psi^{(n)}$ by terms on the order of $O(\varepsilon)$. Terms of the same order arise when the frozen-medium approximation is used for evaluating both the travel time and the mode frequency, with $\omega = \omega_{\mathrm{s}} = \mathrm{const}$ [see Eq. (10)].

In the important particular case of a quiescent medium, the mode propagation constants are independent of the direction of the wave vector. In this case, the expressions for the phase, frequency, and travel time of the mode are simplified. Specifically, it should be assumed in Eqs. (8)–(11) that

$$\frac{\partial \xi_{n0}}{\partial \alpha} \equiv 0 \quad \text{and} \quad \cos\alpha_0 \frac{dx}{dl} + \sin\alpha_0 \frac{dy}{dl} \equiv 1.$$

The analysis of the quasi-stationary approximation within the framework of geometrical acoustics is similar to that considered above for the mode representation of an acoustic field. Namely, the eikonal, the time of travel along a ray, and the instantaneous frequency are given by the expressions

$$\psi_{\mathrm{q}} = \omega_{\mathrm{s}}(T_{\mathrm{q}} - t), \quad T_{\mathrm{q}} = \int_{\mathbf{r}_{\mathrm{s}}}^{\mathbf{r}} \frac{dl}{V(\mathbf{r}_0(l), t_0(l))},$$

$$t_0(l) = t_{\mathrm{s}} + \int_{\mathbf{r}_{\mathrm{s}}}^{\mathbf{r}(l)} \frac{dl'}{V_0(\mathbf{r}_0(l'))}, \tag{12}$$

$$\omega_{\mathrm{q}} = \omega_{\mathrm{s}}\left[1 + \int_{\mathbf{r}_{\mathrm{s}}}^{\mathbf{r}} dl \frac{1}{V^2}\frac{\partial V}{\partial t}\bigg|_{\mathbf{r} = \mathbf{r}_0(l),\, t = t_0(l)}\right]. \tag{13}$$

Here, the integral is taken along the unperturbed ray $\mathbf{r} = \mathbf{r}_0(l)$ between a source at the point $\mathbf{r}_{\mathrm{s}} = (x_{\mathrm{s}}, y_{\mathrm{s}}, z_{\mathrm{s}})$ and a receiver at $\mathbf{r} = (x, y, z)$ in the stationary medium, $t_0(l)$ is the time of travel along the unperturbed ray, $V = \mathbf{u}\dfrac{d\mathbf{r}}{dl} + \left[c^2 - u^2 + \left(\mathbf{u}\dfrac{d\mathbf{r}}{dl}\right)^2\right]^{1/2}$ is the group wave velocity, $c(\mathbf{r}, t)$ is the speed of sound, $u(\mathbf{r}, t)$ is the flow velocity, and V_0 is the value of V in the stationary medium. For simplicity, we assume that in the medium there are no bound-

aries varying with time and that $c^{-1}\left(\left|\dfrac{\partial c}{\partial t}\right| + \left|\dfrac{\partial \mathbf{u}}{\partial t}\right|\right) = O(\varepsilon)$. The estimations obtained above for accuracies of both of the approximations under study also remain valid in the case of geometrical acoustics.

We now consider the traveling-time nonreciprocity, which is defined as the difference between the time T_+ of travel of an acoustic signal from a point A to a point B and the time T_- of the backward travel. According to the reciprocity principle ([10], Sect. 4.2), $T_+ = T_-$ in a quiescent stationary nonuniform medium. The differences $T_+ - T_-$ measured in the ocean are used as input data for solving the inverse problem of the tomographic reconstruction of flow velocity fields ([3], Sect. 3), because such measurements in the stationary case allow us to separate out relatively weak effects due to flows from more pronounced effects caused by unknown variations in the sound-velocity field. In the case of a nonstationary medium, the nonreciprocity arises even if flows are absent.

It follows from Eq. (12) that with an accuracy to the first order in both ε and the ratio $\dfrac{u}{c}$, the traveling-time nonreciprocity is given by the relationships

$$T_+ - T_- = \int_{\mathbf{r}_A}^{\mathbf{r}_B} dl \left[\frac{1}{c(\mathbf{r}_0(l), t_+(l))} - \frac{1}{c(\mathbf{r}_0(l), t_-(l))}\right.$$
$$\left. - \frac{d\mathbf{r}_0}{dl} \frac{\mathbf{u}(\mathbf{r}_0(l), t_+(l)) + \mathbf{u}(\mathbf{r}_0(l), t_-(l))}{c_0^2(\mathbf{r}_0(l))}\right], \tag{14}$$

$$t_+(l) = t_A + \int_{\mathbf{r}_A}^{\mathbf{r}(l)} \frac{dl'}{c_0(\mathbf{r}_0(l'))}, \quad t_-(l) = t_B + \int_{\mathbf{r}(l)}^{\mathbf{r}_B} \frac{dl'}{c_0(\mathbf{r}_0(l'))}. \tag{15}$$

Here, the integral is taken along the ray between the points A and B in the quiescent stationary medium; t_+ and t_- are the arrival times for signals traveling from the points A and B, respectively, in the same medium; and t_A and t_B are the time moments of the signal emission at the corresponding points. In the stationary case, Eq. (14) is reduced to the well-known expression ([3, Sect. 3]).

The traveling-time nonreciprocity evaluated in the frozen-medium approximation is given by formula (14) with t_{ref} substituted for t_+ and t_-. In this approximation, the contribution due to the nonstationarity of speed of sound completely disappears. This result is consistent with the fact mentioned above that the use of the frozen-medium approximation leads to errors of the same (first) order in ε as the desired quantity itself. In other words, the frozen-medium approximation, in contrast to the quasi-stationary one, turns out to be too rough to be applicable for analyzing the traveling-time nonreciprocity.

The contribution of flows and of temporal variations in the speed of sound to the acoustic nonreciprocity were estimated on the basis of Eq. (14) in the problems on the sound transmission through an internal gravity wave soliton propagating on a continental shelf [11] and through the thermocline lens of Mediterranean water in the Atlantic ocean [12]. The estimates show that the ratio of these contributions can be both much more and much less than unity. Thus, the contribution of temporal variations in the speed of sound to the non-reciprocity can be either dominant or negligible and should be estimated under actual conditions of tomographic experiments. Data on the frequency shift of an incoming signal [see Eqs. (10) and (13)] and on the change in the shift with time can be used for separating the contributions considered above. The quasi-stationary approximation provides an adequate method to relate all these acoustic quantities to hydrophysical parameters along the acoustic-signal path.

ACKNOWLEDGMENTS

REFERENCES

1. L. M. Brekhovskikh and Yu. P. Lysanov, *Fundamentals of Ocean Acoustics* (Gidrometeoizdat, Leningrad, 1982; Springer, New York, 1991).

2. F. B. Jensen, W. A. Kuperman, M. B. Porter, and H. Schmidt, *Computational Ocean Acoustics* (AIP, New York, 1994).

3. W. Munk, P. Worcester, and C. Wunsch, *Ocean Acoustic Tomography* (Cambridge Univ. Press, Cambridge, 1995).

4. O. A. Godin, D. Yu. Mikhin, and D. R. Palmer, Izv. Acad. Nauk, Ser. Fiz. Atm. Okeana **36** (1), 141 (2000).

5. W. A. Kuperman, W. S. Hodgkiss, and H. C. Song, J. Acoust. Soc. Am. **103**, 25 (1998).

6. P. Roux and M. Fink, J. Acoust. Soc. Am. **107**, 2418 (2000).

7. O. A. Godin, J. Acoust. Soc. Am. **108**, 2544 (2000).

8. V. M. Babich, V. S. Buldyrev, and I. A. Molotkov, *Space–Time Ray Method: Linear and Non-Linear Problems* (Leningradsk. Gos. Univ., Leningrad, 1985).

9. R. Barridge and G. Weinberg, in *Wave Propagation and Underwater Acoustics,* Ed. by J. B. Keller and J. S. Papadakis (Springer, Heidelberg, 1977; Mir, Moscow, 1980, pp. 76–125).

10. L. M. Brekhovskikh and O. A. Godin, *Acoustics of Layered Medium II: Point Source and Bounded Beams* (Nauka, Moscow, 1989; Springer, Berlin, 1992 and 1999).

11. T. P. Stanton and L. A. Ostrovsky, Geophys. Res. Lett. **25** (14), 2695 (1998).

12. D. Yu. Mikhin, O. A. Godin, O. Boebel, and W. Zenk, J. Atmos. Ocean. Technol. **14** (4), 938 (1997).

Translated by V. Chechin

=========== **PHYSICS** ===========

Wide-Angle Parabolic Equations for Sound in a 3D Inhomogeneous Moving Medium

O. A. Godin

Presented by Academician L.M. Brekhovskikh March 28, 2002

Since the parabolic approach [1; 2; 3, Sect. 7.6] is numerically efficient and describes diffraction effects with reasonable accuracy, it is successfully used for simulating wave fields in inhomogeneous media. In particular, this approach is extensively used in atmospheric and ocean acoustics [4]. For describing sound fields in a moving medium, a 2D wide-angle parabolic equation was derived in [5]. Solutions of this equation satisfy the reciprocity principle and the law of energy conservation, which express the fundamental symmetries of a true wave field. In practice, the exact validity of the reciprocity principle in the absence of flows and the correct reproduction of flow-induced deviations from reciprocity are necessary for the application of the parabolic approximation to the problems of ocean tomography, where the nonreciprocity of acoustic fields measured in experiments concerning the counter propagation of sound is used for reconstructing the flow-velocity field.

In this study, results [5] are generalized such that the parabolic approximation simultaneously becomes more accurate and is extended to inhomogeneous 3D media with a flow.

We assume that a fluid density and the velocities c and $\mathbf{u}$ of sound and flow, respectively, are time-independent but depend arbitrarily on the vertical coordinate z and weakly on the horizontal coordinates x and y. The problem has three small parameters: the Mach number $M = \dfrac{u}{c}$, the ratio κ between the characteristic vertical and horizontal scales of inhomogeneities, and the narrow-angle parameter ε equal to the characteristic relative deviation of mode propagation constants from a certain constant k_0. In a moving medium, the acoustic pressure p satisfies the wave equation [3, Sect. 4.1]

$$\frac{d}{dt}\left[\frac{d}{dt}\left(\frac{1}{\rho c^2}\frac{dp}{dt}\right) - \mathrm{div}\left(\frac{\nabla p}{\rho}\right)\right] + 2\nabla u_m \frac{\partial}{\partial x_m}\left(\frac{\nabla p}{\rho}\right)$$
$$= b + O(\kappa M^2), \tag{1}$$

Shirshov Institute of Oceanology,
Russian Academy of Sciences,
Nakhimovskiĭ pr. 36, Moscow, 117851 Russia

$$b = \frac{d}{dt}\left[\frac{dA}{dt} - \mathrm{div}\left(\frac{\mathbf{F}}{\rho}\right)\right] + 2\nabla u_m \frac{\partial}{\partial x_m}\left(\frac{\mathbf{F}}{\rho}\right). \tag{2}$$

Here, $\dfrac{d}{dt} = -i\omega + \mathbf{u}\nabla$ for monochromatic waves of frequency ω, a and $\mathbf{f}$ are the volume densities of the volume-velocity and extraneous-force sources, respectively. Let the Ox axis be directed along the primary direction of wave propagation and $\mu = \left|\dfrac{y}{x}\right| \ll 1$ in the region essentially affecting the sound field in the plane $y = 0$. In this case, it follows from Eq. (1) that the field complex envelope $\psi = p\exp(-ik_0 x)$ satisfies the equation

$$\frac{\partial \psi}{\partial x} = \frac{ik_0}{2}\hat{S}\psi + \frac{1}{2\rho}\frac{\partial\rho}{\partial x}\psi - \frac{\rho b}{2k_0\omega}e^{-ik_0 x}$$
$$+ O((\varepsilon + \mu + M)(\varepsilon + \mu + \kappa)), \tag{3}$$

$$\hat{S}p = \frac{\rho\beta^3}{k_0^2}\nabla_{\mathrm{T}}\left(\frac{\beta\nabla_{\mathrm{T}}p + \dfrac{ik_0^2\mathbf{u}_{\mathrm{T}}p}{\omega}}{\rho\beta^3}\right) + \beta\left(\frac{k^2\beta^2}{k_0^2} - 1\right)p$$
$$+ \frac{i}{\omega}\mathbf{u}_{\mathrm{T}}\nabla_{\mathrm{T}}p. \tag{4}$$

The operator $\hat{S}$ acts on the coordinates transverse to the primary propagation direction; $\nabla_{\mathrm{T}} = \left(0, \dfrac{\partial}{\partial y}, \dfrac{\partial}{\partial z}\right)$ and $\mathbf{u}_{\mathrm{T}} = (0, u_2, u_3)$. The flow-velocity components u_2 and u_3 transverse to the primary propagation direction are explicitly involved in the operator $\hat{S}$, whereas the longitudinal component u_1 appears through the factor $\beta = 1 - \dfrac{k_0 u_1}{\omega}$. It follows from definition (4) that arbitrary fields p and p_1 satisfy the identity

$$\iint (\rho\beta^3)^{-1}(p_1\hat{S}p - p\hat{S}p_1)\,dy\,dz = 0 \tag{5}$$

in a waveguide that is unbounded along the transversal coordinates or has free and absolutely rigid boundaries.

Here, $\hat{S}_1$ is operator (4), where $\mathbf{u}_T$ is replaced by $-\mathbf{u}_T$. Identity (5) plays the key role in the following analysis of reciprocity and acoustic-energy conservation in the parabolic approximation.

Approximately expressing derivatives ψ_{xx} and ψ_{xxx} involved in (1) in terms of $\hat{S}$ and neglecting the terms of the order of $pO(\varepsilon(\varepsilon^2 + \mu^2) + \mu^4 + M(\varepsilon + \mu + M^2) + \kappa(\kappa + \varepsilon^2 + M))$ and $bO(\kappa)$, we obtain after a number of transformations

$$\frac{\partial}{\partial x}\left[\frac{1}{(\rho\beta^3)^{1/2}}\left(1 + \frac{\hat{S}}{4}\right)p\right] = \frac{ik_0}{(\rho\beta^3)^{1/2}}\left(1 + \frac{3\hat{S}}{4}\right)p$$

$$- \frac{1}{2k_0(\rho\beta^3)^{1/2}}\left(1 + \frac{\hat{S}}{4}\right)^{-1}\frac{\rho b}{\omega}. \qquad (6)$$

In the 2D problem $\left(\text{i.e., for } \dfrac{\partial}{\partial y} = 0 \text{ and } u_2 = 0\right)$, Eq. (6) becomes the familiar generalized 2D Claerbout equation, which was considered for the case of small vertical flows $\{u_3 = O(\kappa u)\}$ [5] and for a stationary medium [3, Sect. C.3].

As a rule, the characteristic values of the parameter ε in geophysical applications exceed μ, M, and κ by 1–3 orders of magnitude, and the accuracy of the parabolic approximation based on (6) is limited by the rejected terms $pO(\varepsilon^3)$. For increasing the accuracy with respect to the parameters ε and μ, similar to the case of a stationary medium [6], we consider the parabolic equation

$$\frac{\partial}{\partial x}[(\rho\beta^3)^{-1/2}\Phi_2(\hat{S})p] = ik_0(\rho\beta^3)^{-1/2}\Phi_1(\hat{S})\Phi_2(\hat{S})p$$

$$- (\rho\beta^3)^{-1/2}[2\omega k_0\Phi_2(\hat{S})]^{-1}\rho b, \qquad (7)$$

where $\Phi_N(a)$ are the analytic functions that satisfy the condition $\Phi_N(a^*) = [\Phi_N(a)]^*$ and approximate the functions $(1 + a)^{1/2N}$, $N = 1, 2$. Efficient numerical methods of solving parabolic equations are developed for the cases where pseudodifferential operators are approximated by rational functions $\Phi_N(\hat{S})$ [4, 7–10]. When

$$\Phi_1(a) = \left(1 + \frac{3a}{4}\right)\left(1 + \frac{a}{4}\right)^{-1}, \quad \Phi_2(a) = 1 + \frac{a}{4}, \quad (8)$$

Eq. (7) is the generalized 3D Claerbout equation (6). In a stationary medium, Eq. (7) becomes the parabolic 3D equation that conserves energy and provides arbitrarily high accuracy with respect to the parameters ε and μ owing to the choice of the functions Φ_N. The properties of flows appear in Eq. (7) through the operator $\hat{S}$, fac-

tor β, and quantity b, which is defined in Eq. (2) and describes the sources of sound.

We consider the reciprocity properties inherent in the solutions of Eq. (7). Let a solution p of Eq. (7) be the sound field generated for $x > x_0$ by sources arranged with density b in the neighborhood of the cross section $x = x_0$ of the waveguide in the initial medium, whereas p_1 be the field generated for $x < x_1$ by sources arranged with density b_1 in the neighborhood of the cross section $x = x_1 > x_0$ in the medium with an inverted flow [i.e., where the velocity of flows is $-\mathbf{u}(\mathbf{r})$]; p_1 satisfies Eq. (7) where b and $\hat{S}$ are replaced by b_1 and $\hat{S}_1$, respectively. Multiplying Eq. (7) by $(\rho\beta^3)^{-1/2}\Phi_2(\hat{S}_1)p_1$ and $(\rho\beta^3)^{-1/2}\Phi_2(\hat{S})p$, summing the results, integrating over volume, and using Eq. (5), we obtain

$$\iiint(\rho\beta^2)^{-1}(bp_1 - b_1p)dxdydz = 0. \qquad (9)$$

This identity expresses the flow-inversion theorem [3, Sect. 8.4] and shows that certain characteristics of a field generated by point sources of sound are invariant when the source and observation point are interchanged and the flow is simultaneously inverted. Comparison of (9) and (2) with the flow-inversion theorem for true sound fields [3, Sect. 8] shows that the invariant characteristics are reproduced by the parabolic approximation with an accuracy of $O\{(\varepsilon + \mu)M(\varepsilon + \mu + M + \kappa)\}$. In particular, Eq. (9) for $\mathbf{u} = 0$ coincides with the exact relationships of the sound-field symmetry with respect to the source–receiver rearrangement. In other words, acoustic nonreciprocity in parabolic approximation (7), as well as in the true sound field, is completely caused by flows.

In the source-free region, the flow-inversion theorem is expressed by the identity following from Eqs. (7) and (5):

$$\frac{\partial}{\partial x}\iint dydz\,j_1 = 0,$$

$$j_1 = \frac{k_0}{2\omega\rho\beta^3}\Phi_2(\hat{S})p\Phi_2(\hat{S}_1)p_1, \qquad (10)$$

where the integration is performed over the waveguide cross section $x = \text{const}$. For generalized Claerbout equation (6), the local relationship

$$\nabla\mathbf{j} = 0, \quad j_1 = \frac{k_0}{2\omega\rho\beta^3}\left(1 + \frac{\hat{S}}{4}\right)p\left(1 + \frac{\hat{S}_1}{4}\right)p_1,$$

$$\mathbf{j}_T = \frac{p_1\nabla_T p - p\nabla_T p_1}{4i\omega\rho\beta^2} + \frac{k_0^2 pp_1\mathbf{u}_T}{2\omega^2\rho\beta^3} \qquad (11)$$

is also valid. Relationships (11) were derived similar to identity (9), but without integration over volume.

In the medium with real values of ρ, c, and $\mathbf{u}$, i.e., without absorption, the complex conjugate field p^* and field p_1 satisfy the same parabolic equation. Therefore,

Eqs. (9)–(11) remain to be valid when p_1 is replaced by p^*. In this case, Eqs. (10) and (11) express the law of energy conservation for solutions of Eq. (7). Equation (10) physically means that the acoustic-energy flow is constant when a wave propagates along a waveguide, and the quantity $\mathbf{j}$ in Eqs. (11) has the meaning of power-flow density averaged over the wave period. The quantity $\mathbf{j}$ and the exact power-flow density $\mathbf{J}$ [3, Sect. 8.6] in a moving medium can be compared similarly to the 2D case [5]; it turns out that the two expressions are asymptotically close when Eq. (6) is applicable:

$$\mathbf{j} = \mathbf{J}[1 + O((\varepsilon + \mu + M + \kappa)^2)].$$

If there are interfaces in the fluid, i.e., surfaces on which ρ, c, and $\mathbf{u}$ are discontinuous, then the parabolic equation must be supplemented by boundary conditions. Boundary conditions consistent with the parabolic equation can be derived by replacing an abrupt interface by a thin transition layer with the further passage to the limit in the thickness of this layer [3, Sect. C.3.3]. Equivalently, we can require that the parabolic equation be satisfied everywhere in space in the generalized-function sense. In this case, boundary conditions follow from the balance of singularities in the left-hand and right-hand sides of the parabolic equation at the interface. For simplicity, we assume that the sound sources are not at the interface. Then, for the interface $x = \mathrm{const}$, which is perpendicular to the primary wave-propagation direction, it follows from Eq. (7) that

$$\left\lfloor (\rho\beta^3)^{-1/2}\Phi_2(\hat{S})p \right\rfloor_\Gamma = 0, \tag{12}$$

where $[f]_\Gamma$ is the jump of the function on the surface Γ. For other interfaces, the type of the boundary condition depends on their orientation and on the choice of the functions Φ_1 and Φ_2 approximating the roots of operators. We here present only the results for generalized Claerbout equation (6). Let $\mathbf{N} = (N_1, N_2, N_3)$ be the normal to the interface Γ. If $N_1 = 0$, two boundary conditions must be satisfied:

$$[p]_\Gamma = 0, \quad \left[\frac{1}{\rho\beta^2}\mathbf{N}\nabla_\mathrm{T}p + \frac{ik_0}{\omega}\frac{\mathbf{N}\mathbf{u}_\mathrm{T}p}{\rho\beta^3}\right]_\Gamma = 0. \tag{13}$$

If $N_2^2 + N_3^2 = 0$, boundary condition (12) [where Φ_2 is given by Eq. (8) for parabolic equation (6)] must be satisfied. If $N_1(N_2^2 + N_3^2) \neq 0$, both boundary condition (12) and boundary condition (13) must be satisfied. In all these cases, the number of imposed boundary conditions is equal to the order of differential equation (7) or (6), respectively, relative to the derivative along the normal to the interface. As would be expected, the direct test shows that the above boundary conditions guarantee the continuity of the normal component for the power-flow density $\mathbf{j}$ given by Eqs. (10) and (11) at the interface.

To use the parabolic equation for simulating scattering by irregular surfaces, it is important to find boundary conditions for perfect (free and absolutely rigid) interfaces. These boundary conditions follow from the above at the interface when the density of one medium tends to zero or to infinity. For a free interface, $p = 0$ if $N_1(N_2^2 + N_3^2) = 0$, whereas $p = 0$ and $\hat{S}p = 0$ if $N_1(N_2^2 + N_3^2) \neq 0$. At an absolutely rigid interface, $\Phi_2(\hat{S})p = 0$ if $N_2^2 + N_3^2 = 0$, $\mathbf{N}(\omega\beta\nabla_\mathrm{T}p + ik_0p\mathbf{u}_\mathrm{T})$ if $N_1 = 0$, and both last boundary conditions must be satisfied simultaneously if $N_1(N_2^2 + N_3^2) \neq 0$. For $N_2^2 + N_3^2 = 0$, the above energy-conserving boundary conditions are valid not only for solutions to Eq. (6), but also in the more general case of Eq. (7).

For estimating the asymptotic accuracy of the parabolic approximation based on Eq. (7), we compare the solutions to this equation and to exact equations of linear acoustics in the ray approximation. Substituting the field in the form of the Debye series $p = A\exp(ik_0\theta)$, where $A = A_0 + (ik_0)^{-1}A_1 + \ldots$, and A_j and θ is independent of k_0 in the leading order in $\frac{1}{k_0}$ into Eq. (7), we obtain the equation

$$\zeta = \Phi_1(\alpha), \quad \alpha = \beta\left(\frac{\omega^2\beta^2}{k_0^2 c^2} - 1\right) - \frac{2k_0\mathbf{v}_\mathrm{T}\mathbf{u}_\mathrm{T}}{\omega} - \beta\mathrm{v}_\mathrm{T}^2. \tag{14}$$

Here, $\mathbf{v} = \nabla\theta$ and ζ is the value of $\frac{\partial\theta}{\partial x}$ in the parabolic approximation. Equation (14) approximates the exact eikonal equation $\frac{\omega}{k_0} = c\mathrm{v} + \mathbf{u}\mathbf{v}$ [3, Sect. 5.1.3]. Let $\Phi_1(a) = (1 + a)^{1/2}$. Comparing the exact ($\mathrm{v}_1$) and approximated ($\zeta$) values of $\frac{\partial\theta}{\partial x}$, we obtain the leading phase-error term of the parabolic approximation, which is accumulated with distance, in the form

$$\delta\theta \sim k_0x|\mathrm{v}_1 - \zeta| = k_0xO(M(\varepsilon + \mu)^2).$$

If $\Phi_1(a)$ approximates $(1 + a)^{1/2}$ with an accuracy of $O(a^m)$, $\delta\theta = k_0xO(M(\varepsilon + \mu)^2 + (M + \varepsilon + \mu)^m)$ because $\alpha = O(M + \varepsilon + \mu)$ in Eq. (14). For generalized Claerbout equation (6), $m = 3$, and the expression obtained for $\delta\theta$ agrees with the results obtained above by estimating the terms rejected when deriving Eq. (6). The accuracy of the approximation $\Phi_2(a) \approx (1 + a)^{1/4}$ does not affect the phase error but affects the agreement between power flows $\mathbf{J}$ and $\mathbf{j}$ and, therefore, the amplitude error of parabolic-equation solutions.

The parabolic approximation is applicable up to the distances $x \ll \dfrac{\delta\theta}{k_0}$ from the source. Since $\varepsilon \gg M + \mu$ in

the geophysical applications, the region of applicability of the generalized Claerbout equation in moving and stationary media as well as in the 2D and 3D problems are virtually identical. The choice of high-order approximations for Φ_N extends the region of applicability and improves the accuracy of Eq. (7) compared to Eq. (6).

Thus, we here proposed a class of wide-angle parabolic wave equations for sound in a 3D inhomogeneous moving fluid. These equations provide higher accuracy than the familiar wide-angle parabolic equations [4, 5, 10–14] for moving media and are consistent with the law of energy conservation and with the flow-inversion theorem in the parabolic approximation.

ACKNOWLEDGMENTS

REFERENCES

1. F. D. Tappert, in *Wave Propagation and Underwater Acoustics,* Ed. by J. B. Keller and J. S. Papadakis (Springer, New York, 1977; Mir, Moscow, 1980, pp. 180–226).

2. S. M. Rytov, Yu. A. Kravtsov, and V. I. Tatarskiǐ, *Principles to Statistical Radiophysics* (Nauka, Moscow, 1978; Springer, Berlin, 1987), Part 2.

3. L. M. Brekhovskikh and O. A. Godin, *Acoustics of Layered Medium II: Point Source and Bounded Beams* (Nauka, Moscow, 1989; Springer, Berlin, 1999).

4. D. Lee, A. D. Pierce, and E.-C. Shang, J. Comput. Acoust. **8**, 527 (2000).

5. O. A. Godin, Dokl. Akad. Nauk **361**, 329 (1998) [Dokl. Phys. **43**, 393 (1998)].

6. O. A. Godin, Dokl. Akad. Nauk **373**, 607 (2000) [Dokl. Phys. **45**, 367 (2000)].

7. K. V. Avilov, in *Acoustics of the Ocean Medium* (Nauka, Moscow, 1989), pp. 10–19.

8. M. D. Collins, J. Acoust. Soc. Am. **92**, 2069 (1992).

9. M. D. Collins, R. J. Cederberg, D. B. King, and S. A. Chin-Bing, J. Acoust. Soc. Am. **100**, 178 (1996).

10. D. Mikhin, J. Comput. Acoust. **9**, 183 (2001).

11. O. A. Godin and A. V. Mokhov, in *Proceedings of the European Conference on Underwater Acoustics, Luxembourg*, Ed. by M. Weydert (Elsevier, London, 1992), p. 280.

12. Yu. S. Kryukov, Akust. Zh. **43** (3), 421 (1997) [Acoust. Phys. **43**, 360 (1997)].

13. V. E. Ostashev, D. Juvé, and P. Blanc-Benon, Acust. Acta Acust. **83** (3), 455 (1997).

14. L. Dallois, P. Blanc-Benon, and D. Juvé, J. Comput. Acoust. **9**, 477 (2001).

Translated by V. Bukhanov

═══════════════════ **PHYSICS** ═══════════════════

On the Thermal Stability of the Microcrystalline Structure in Single-Phase Metallic Materials

M. V. Degtyarev, L. M. Voronova, V. V. Gubernatorov, and T. I. Chashchukhina

Presented by Academician O.A. Bannykh April 3, 2002

In the problem of deformation and annealing of metals and alloys, the urgent question on the thermal stability of the microcrystalline structure exhibiting unique properties remains open. At present, the following methods of retarding crystal (grain) growth are well known and widely used: (1) texture retardation; (2) inhibition by segregation and by disperse particles of the second phase; (3) grooves of thermal etching; and (4) weak (down to 1%) deformation of the recrystallized material [1, 2].

From general concepts on crystallite growth, an additional method for stabilizing the grain structure follows. If in a polycrystalline material a honeycomb structure with an equal crystallite size and balanced triple junction is obtained, then the system can reside in the quasi-stable state as long as wished [1]. However, this method has not yet been confirmed experimentally and is not applied, due to fundamental difficulties in the formation of the above structure. Nevertheless, these difficulties to some extent can be avoided by using shear plastic deformation under a high hydrostatic pressure. Severe strains realized by this method form in a material a homogeneous microcrystalline structure [3].

In the present paper, we have studied the thermal stability on isothermal heating of a microcrystalline structure with a different homogeneity. The structure was obtained in single-phase iron as a result of shear plastic deformation under pressure.

We studied iron of 99.97% purity with a content of $C \leq 0.003$; $Mn \leq 0.006$; $Si < 0.009$; $Cr < 0.008$; and $Ni < 0.003\%$. Specimens 5 mm in diameter and 0.3 mm thick were deformed by shear under a pressure of 6 GPa. In order to provide different structure homogeneities, the rotation angle of an anvil was chosen to be 1 or 5 revolutions. True logarithmic shear strains at a distance of 1.5 mm from the center of the deformed specimens attained $e = 6$ and 8, respectively. The deformed specimens were annealed in a salt bath at 200°C with a holding of 1 to 64 h. In order to avoid contact with salt, the specimens were placed into a box made of permalloy foil.

We investigated the material structure at a distance of 1.5 mm from the center of the specimen by the electron-microscopy method. The size of microcrystallites was determined by their bright-field and dark-field images in $(110)_\alpha$-type reflection. Not less than 200 separate measurements were performed, which provided an error lower than 10%. Then, size histograms and microcrystallite-size distributions were plotted according to the measurement results for microcrystallite diameters. The microstructure inhomogeneity was calculated according to the full width at half-maximum

The effect of treatment on the microcrystalline-structure parameters

Treatment	d_{min}, μm	d_{max}, μm	d_{av}, μm	d_{prob}, μm	FWHM	v, μm h^{-1}
$e = 6$	0.03	0.75	0.19	0.1	0.17	
$e = 6$, 200°C, 1 h	0.05	1.2	0.35	0.2	0.33	0.16
$e = 6$, 200°C, 64 h	0.14	2.6	0.74	0.4	0.69	0.009
$e = 8$	0.02	0.75	0.15	0.07	0.13	
$e = 8$, 200°C, 1 h	0.04	0.75	0.19	0.12	0.17	0.04
$e = 8$, 200°C, 64 h	0.04	0.75	0.22	0.13	0.19	0.001

Institute of Metal Physics, Ural Division, Russian Academy of Sciences,
ul. Sof'i Kovalevskoĭ 18, Yekaterinburg, 620219 Russia
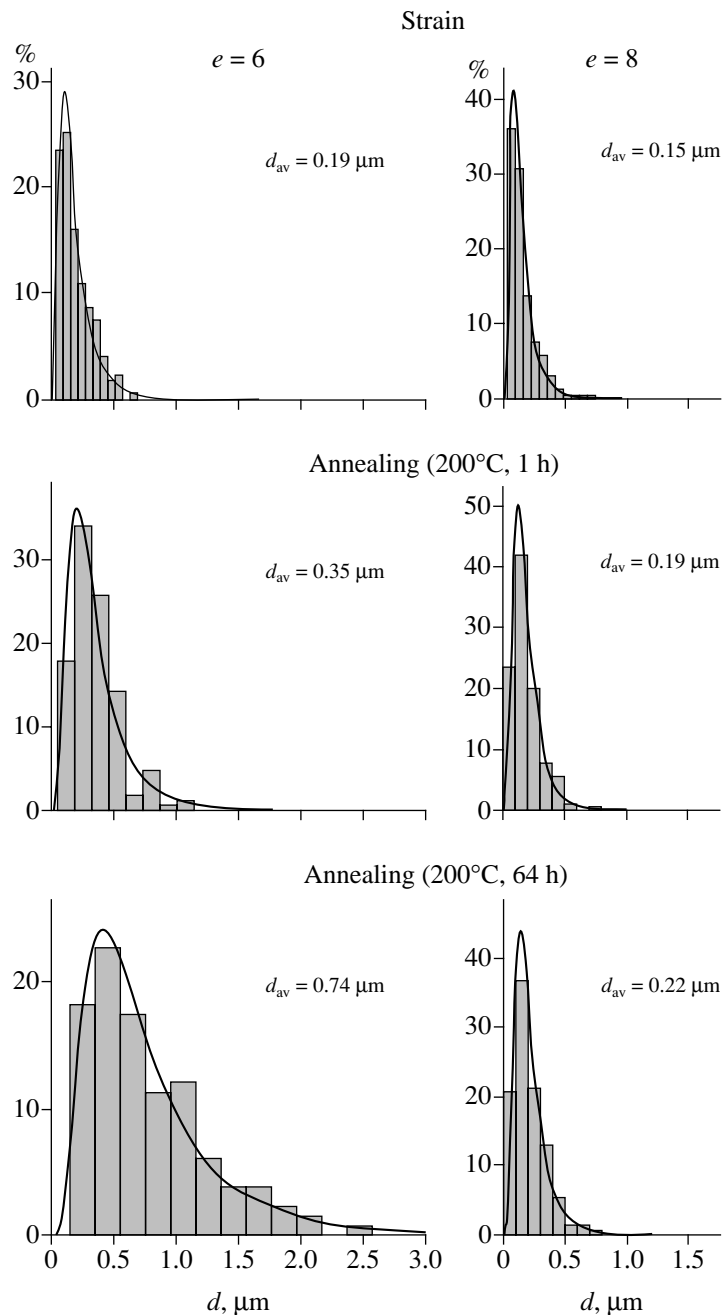*E-mail: highpress@imp.uran.ru*

Fig. 1. Histograms of microcrystallite size distributions obtained after deformation and annealing of specimens at 200°C.

(FWHM) for the microcrystallite-size distribution obtained.

The parameters of the microcrystalline structure and of the microcrystallite-size distribution, which were measured after deformation and annealing of the specimens, are presented in the table and shown in Fig. 1.

With an increase in the logarithmic strain e from 6 to 8, the minimal size of microcrystallites decreases from 0.03 to 0.02 μm. In both cases, the size of the largest microcrystallites does not exceed 0.8 μm. An increase in the degree of strain is accompanied by a decrease in the fraction of the largest crystallites and a shift of the size-distribution maximum to smaller values (from 0.1 to 0.07 μm). The average microcrystallite size decreases from 0.19 to 0.15 μm. The FWHM of the size distribution decreases from 0.17 to 0.13 μm, which testifies to the improvement of the structure homogeneity.

After a strain of $e = 6$ and 1-h annealing, large microcrystallites increase up to 1.2 μm. The most probable microcrystallite size grew by a factor of two (from 0.1 to 0.2 μm). The FWHM attained 0.33 μm. The increase in the annealing duration to 64 h resulted in a growth of both small and large microcrystallites and a

shift of the size-distribution maximum towards larger sizes (0.4 μm). The FWHM increased to 0.69 μm.

On annealing specimens deformed with the strain $e = 8$, we observed other kinetics of the microcrystallite growth. Holding for both 1 and 64 h did not lead to a significant change in the size distribution of microcrystallite: the size of the largest of them remained unchanged. The fraction of microcrystallites with a size of 0.3–0.7 μm increased only slightly. The most probable and the average microcrystallite size grew negligibly, by less than a factor of two. After holding for 1 and 64 h, the FWHM attained 0.17 and 0.19 μm, respectively.

The microcrystallite growth rate calculated by a change in the average size of the annealing time depends on the degree of strain. The average growth rate after 1-h holding was 0.16 and 0.04 μm in the case of $e = 6$ and 8, respectively. The further isothermal holding for 64 h led to the reduction in the growth rate to 0.009 and 0.001 μm h^{-1}; i.e., the difference in the growth rate increased all the more. This is the fact that constitutes a fundamental feature of the method under consideration of the structure stabilization. When stabilizing the grain structure, e.g., by disperse particles of the second phase, the initial fine grains grow more rapidly than initial coarse grains [4].

Figure 2 presents the microstructure after the annealing of deformed specimens with $e = 6$ and 8. Annealing after a severe strain resulted in the appearance of microcrystallites of a regular hexagonal shape (Fig. 2a). The angles in junctions of these microcrystallites are close to equilibrium ones. After smaller deformation, as a result of annealing, finely divided microcrystallites appear in the structure. Their shape is close to the equilibrium one. Along with them, multiangular large growing microcrystallites with concave boundaries are observed (Fig. 2b).

Electron microscopy analysis of the structure by the dark-field method after both degrees of strain and holding for 1 h revealed a difference in the misorientation of growing microcrystallites. After the strain with $e = 6$, certain neighboring microcrystallites have a close orientation (Fig. 2c). In the case of further increasing the holding time, microcrystallite merging can occur, which leads to the formation of separate coarse grains. After the strain with $e = 8$, close orientations of neighboring microcrystallites were not observed. As was shown in [5] when investigating iron of the same purity as in the present study, the shear strain with $e = 6$ under pressure forms an axial torsion texture. The increase of the strain to $e = 8$ destroys the texture, and the material state approaches the textureless one. This provides a chaoticity of microcrystallite misorientations after a severe strain. As a result, some microcrystallites do not get advantages in their growth, which leads to the improvement of the homogeneity and stability of the structure with respect to isothermal annealing.
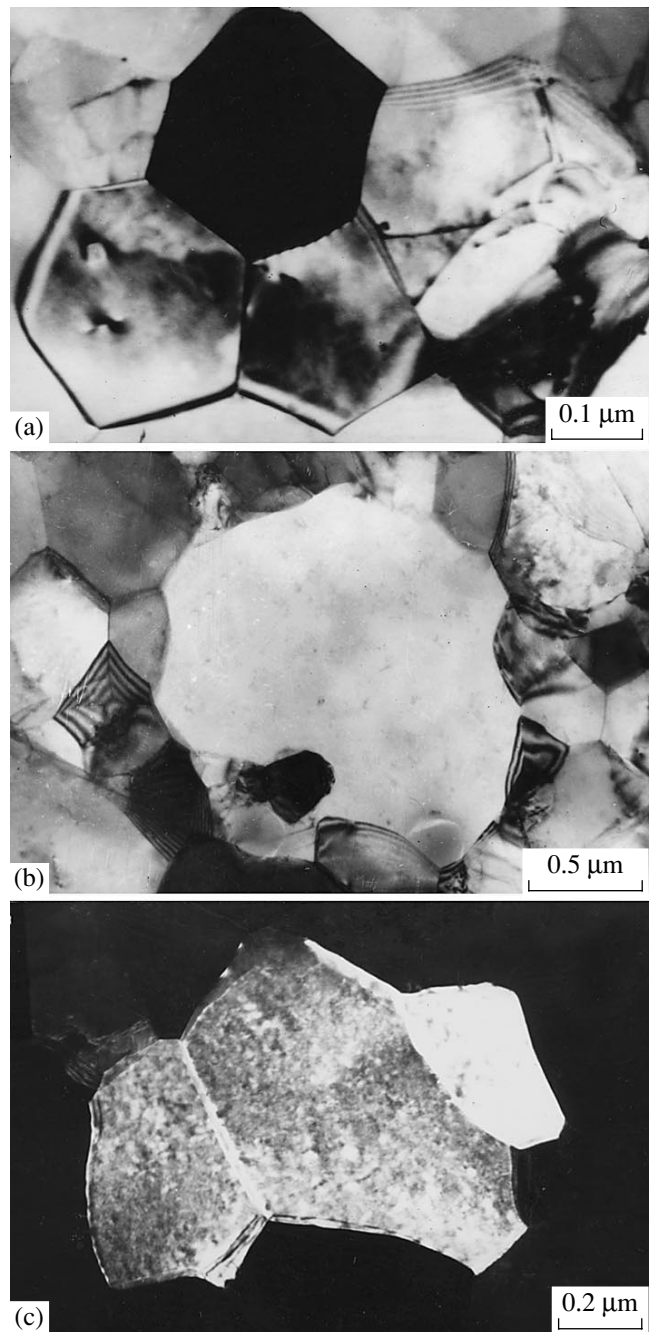
Fig. 2. Microstructure of iron after a strain with (a) $e = 8$ and (b, c) $e = 6$ and annealing at 200°C: (a, b) 64 and (c) 1 h. The image is obtained by the dark-field method in the $(110)_\alpha$-type reflection.

The application of severe plastic shear strain under hydrostatic pressure opens a new outlook on the elevation of thermal stability of single-phase materials with the microcrystalline structure.

The high degree of the size homogeneity of the microcrystalline structure and the absence of a texture in a material strongly deformed by shear under pressure hampers the growth of individual microcrystallites on

heating. In this case the increase in the structure regularity occurs at the expense of the perfection of microcrystallite boundaries and shape in the conditions of a low growth rate. The resulting perfect single-phase structure manifests a high thermal stability with an increase in the duration of isothermal annealing. This can provide a perfect set of properties (including strength and plasticity) of such a microcrystalline material.

ACKNOWLEDGMENTS

REFERENCES

1. S. S. Gorelik, *Recrystallization of Metals and Alloys* (Metallurgiya, Moscow, 1978).

2. B. K. Sokolov, Izv. Akad. Nauk SSSR, Ser. Fiz. **46** (4), 693 (1982).

3. N. A. Smirnova, V. I. Levit, V. P. Pilyugin, *et al.*, Fiz. Met. Metalloved. **61**, 1170 (1986).

4. B. N. Balandin, B. K. Sokolov, and V. V. Gubernatorov, Fiz. Met. Metalloved. **49**, 590 (1980).

5. A. M. Patselov, *Cand. Sci. (Phys.-Math.) Dissertation*, Yekaterinburg: Inst. of Metal Phys., 1999.

Translated by G. Merzon

=== **PHYSICS** ===

The Effect of Boron on the Thermal Stability
of Polycrystalline Carbonado Diamonds

Academician A. V. Elyutin, A. A. Ermolaev, A. I. Laptev, and A. V. Manukhin

Received May 13, 2002

Polycrystalline diamond as an instrumental material is subjected to the action of high temperatures during both fabrication of diamond tools and their exploitation. As a result, strength properties of diamond polycrystals decrease. The elevation of the temperature below which heating polycrystals does not lead to the deterioration of their physicomechanical properties is an important practical task. The increase in thermal stability of diamonds allows more rigorous regimes to be applied while processing materials and, hence, the efficiency of the diamond processing to be elevated. This also allows us to improve the quality of a diamond tool owing to the employment of more durable refractory binders at its fabrication.

It is well known that boron affects the increase in the oxidation-onset temperature and the decrease in the oxidation intensity of both polycrystalline [1] and monocrystalline diamonds [2]. Carbonado polycrystals are obtained by synthesis of a carbon material in the presence of catalyzing alloys based on iron, nickel, and cobalt, which promote the transformation of these polycrystals into diamond. The carbonado polycrystals consist of both diamond crystallites and an intercrystallite binder.

The goal of this paper is to elucidate the effect of boron on the elevation of the thermal stability of polycrystalline carbonado diamonds. A possibility is shown by purposefully doping an initial catalyzing alloy that promotes the graphite-diamond transformation to affect the thermal stability of carbonado as a whole and to open the mechanism of the phenomenon. We have established that the thermal stability of polycrystalline carbonado diamond depends not only on the intensity of its interaction with oxygen but on the relation between the thermal-expansion coefficients of diamond crystallites and a metal-ceramic binder. The regularity established allows us to develop an approach to the purposeful doping of carbonado polycrystals with the aim of obtaining the desired properties.

The catalyzing alloy of the (20Cr–80Ni)–B composition was prepared by methods of the powder metallurgy from powders of nickel (PNK–OT4 GOST 9722-79), chromium (PKh1, TU 14-1-14-74), and amorphous boron (MRTU 6-02-293-64). Polycrystals were synthesized at a pressure of 8.0 GPa at a temperature of 1800–2000 K, the duration of the synthesis being 15 s. The mass of the polycrystal formed was 0.8–1.0 carat.

For determining the chemical composition of the polycrystal, its spectral analysis was carried out by the method developed in the Institute of Synthetic Materials of the Ukrainian Academy of Sciences. The method is based on the burning of the preform placed in the crater of the carbon electrode in an alternating-current arc ($I = 12$–14 A) and the photographing of spectra by an ISP-30 spectrograph. The boron concentration was determined by the method of three standards. S-3 (OSCh-7-4) spectrally pure graphite was the basis for the preparation of standards. The boron content in a polycrystal as a function of its content in the initial Kh20N80 agent alloy is shown in Fig. 1.

The ability of retaining strength properties in the case of heating carbonado was studied according to the change in the strength of the ARK4 diamond abrasive powder (fraction 400/315). The powder was obtained by milling diamond polycrystals synthesized with the employment of catalyzing alloys having a different boron content.
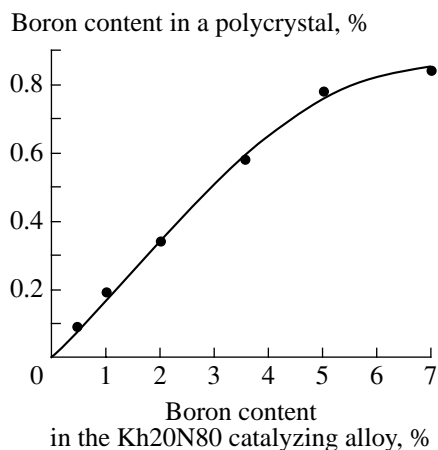

Fig. 1. Effect of the boron content in the Kh20N80 catalyzing alloy on the boron content in a polycrystal.

Moscow Institute of Steels and Alloys,
Leninskiǐ pr. 4, Moscow, 117936 Russia
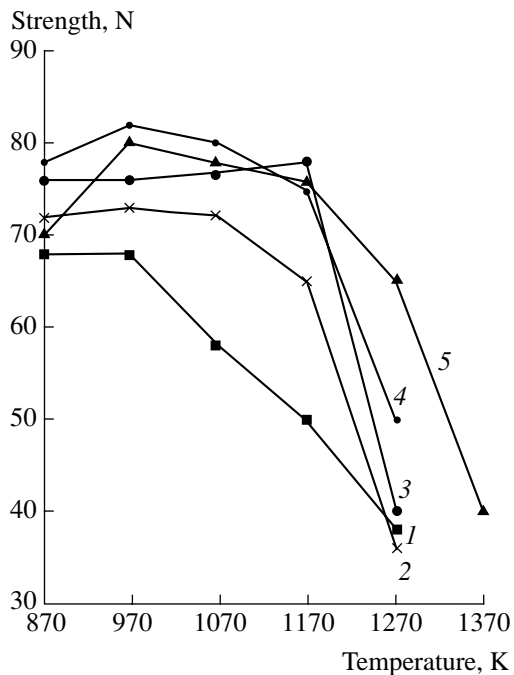
Strength, N

Fig. 2. Strength of the ARK4 400/315 diamond abrasive powder as a function of the calcination temperature in ambient air. The boron content in the catalyst is: (*1*) 0, (*2*) 0.5, (*3*) 2, (*4*) 3.5, and (*5*) 7%.

Diamond grains were processed by the following method. Ceramic crucibles with the ARK4 400/315 powder were introduced into a muffle furnace heated to an assigned temperature. After their heating to the furnace temperature and 5-min holding, they were cooled in ambient air. The temperature was measured with a chromel–alumel thermocouple with an accuracy of ±10 K. Thermally treated and initial powders were subjected to strength testing at a PA-4E test machine in accordance with the GOST 9206-80 procedure. The results of these tests are shown in Fig. 2. As follows from the data presented, the effect of treatment temper-
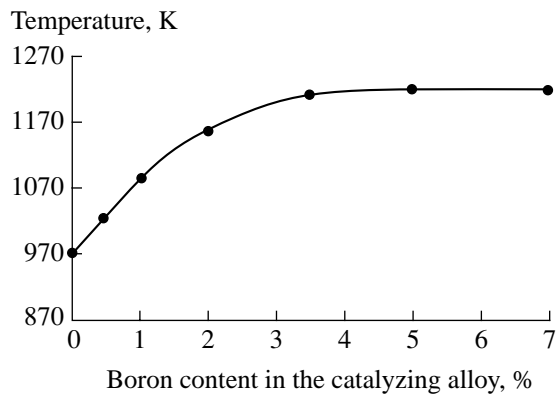
ature on the strength of a polycrystal depends on the boron content in the catalyzing alloy. The effect of the boron content in the catalyzing alloy on the temperature (for which the 5-min exposure results in the loss of ARK4 400/315 strength more than by 5%) is presented in Fig. 3. Introducing boron elevates the thermal stability of diamond polycrystals from 970 to 1220 K.

By annealing a boron-containing diamond powder in ambient air, a film of B_2O_3 boron oxide is formed, which hinders the oxidation of the powder. In order to assess the effect caused by the presence of this film on the increase in the heat resistance of boron-containing polycrystals, annealing of ARK4 400/315 powder was carried out for 15 min at a temperature of 1270 K in vacuum. The results of the tests for the strength of boron-containing diamond powders annealed in vacuum for 15 min and calcined in ambient air for 5 min at a temperature of 1270 K are shown in Fig. 4. It follows from the data presented that doping a catalyzing alloy with more than 3% of boron reduces the loss of ARK4 400/315 strength after the thermal treatment in both ambient air and vacuum. Therefore, the positive effect of boron on the thermal resistance of the diamond powder cannot be explained by only the enhancement of its resistance to oxidation. Boron enters into a polycrystal in the form of nickel borides, whose coefficients of thermal expansion are closer to those of diamond than the coefficient of thermal expansion of the catalyzing alloy [3, 4]. When heating, a noticeable difference in the coefficients of thermal expansion of the diamond and inclusions presented by the catalyzing alloy results in the appearance of significant thermal stresses that lower the strength of diamond grains [5]. In addition to an increase in the resistance to the oxidation of diamond, introducing boron into a catalyzing alloy reduces thermal stresses caused by heating and thereby increases the thermal stability of polycrystalline diamond. The estimation of the contribution of each of the processes under consideration determining the effect of
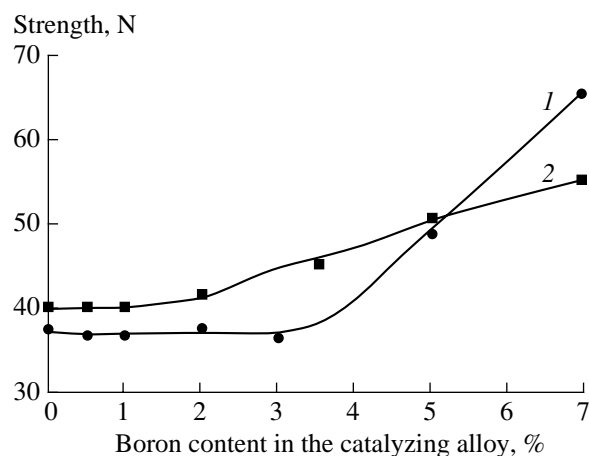

Fig. 3. Effect of the boron content in the catalyzing alloy on the thermal stability of ARK4 400/315 (exposure at this temperature results in a decrease in the strength).

Fig. 4. Effect of the boron content in the catalyzing alloy on the strength of ARK4 400/315 diamond powder after the thermal treatment at 1270 K: (*1*) air, 5 min; (*2*) vacuum, 15 min.

boron on the thermal stability of polycrystalline diamond needs further study.

Thus, doping of a catalyzing alloy with boron results in the formation of borides in a polycrystal, which enhance its stability to the oxidation and lower its thermal stresses as a result of heating due to a decrease in the coefficient of thermal expansion of the inclusions (binders), which increases the thermal stability of diamond from 970 to 1220 K.

REFERENCES

1. V. V. Loparev, V. I. Veprintsev, A. V. Manukhin, *et al.*, Sverkhtverd. Mater., No. 6, 11 (1984).

2. N. F. Kirova, N. A. Kolchemanov, and Yu. M. Ryvkin, Sint. Almazy, No. 2, 17 (1976).

3. *Properties, Synthesis, and Application of Refractory Compounds. Handbook*, Ed. by T. Ya. Kosolapova (Metallurgiya, Moscow, 1986).

4. *Compound Materials. Handbook*, Ed. by D. M. Karpinos (Naukova Dumka, Kiev, 1985).

5. V. N. Bakul', N. V. Tsypin, and V. G. Gargin, in *Physicochemical Problems of Superhard Material Synthesis* (Inst. Synth. Mater. Acad. Nauk Ukr. SSR, Kiev, 1978), pp. 141–144.

Translated by T. Galkina

Noise-Induced Transition and $\dfrac{1}{f}$ Fluctuations while Intersecting Nonequilibrium Phase Transitions

Corresponding Member of the RAS V. P. Koverda and V. N. Skokov

Received May 15, 2002

Flicker noise $\left(\dfrac{1}{f} \text{ noise}\right)$ is a widespread phenomenon in nature [1]. It is observed in radio engineering devices, in solid-state physics, in fracture mechanics, in chemical reactions, etc. An intrinsic feature of systems with noise lies in the fact that the power spectrum in this case is inversely proportional to the frequency f. Such a dependence suggests that a considerable part of the fluctuation energy is associated with slow processes and, moreover, implies a possibility of huge catastrophic surges in the system.

Although the problem on the origin of the $\dfrac{1}{f}$ noise is fairly general, to a large extent, it remains unresolved. The physical picture of this phenomenon has not been elucidated to date, and mechanisms responsible for such a fluctuation spectrum are often unclear. The dynamics of fluctuations in certain systems nonconventional from the standpoint of flicker-noise studies was investigated in [2–8]. We imply systems in boiling-crisis regimes, under explosive boiling of superheated-liquid jets, in oscillatory regimes of combustion, and in arc electric discharge. The presence of low-frequency intense pulsations with a power spectrum inversely proportional to the frequency was established in both crisis and transient regimes of the processes under investigation. An elementary source of fluctuations with the $\dfrac{1}{f}$ power spectrum was first revealed in these experiments. This allowed the kinetics of the source to be systematically affected in experiments.

A new model of the flicker noise was formulated on the basis of the experiments performed in [3, 9].

Institute of Thermal Physics, Ural Division,
Russian Academy of Sciences, Pervomaĭskaya ul. 91,
Yekaterinburg, 620219 Russia

According to the model, fluctuations with a $\dfrac{1}{f}$ power spectrum originate in a system as a result of simultaneously interacting phase transitions in the presence of sufficiently intense white noise. In the case of a concentrated system, the simplest stochastic equations describing the dynamics of fluctuations take the form

$$
\begin{aligned}
\frac{d\phi}{dt} &= -\phi\psi^2 + \psi + \Gamma_1(t), \\
\frac{d\psi}{dt} &= -\phi^2\psi + 2\phi + \Gamma_2(t).
\end{aligned}
\tag{1}
$$

Here, ϕ and ψ are dynamical variables (order parameters), while Γ_1 and Γ_2 are Gaussian δ-correlated noises that can have various realizations but identical variances provided that the equations are written out in the form of Eqs. (1). The factor ϕ entering into the second term of the second equation specifies a certain macroscopic flux in the system under consideration.

In order to numerically integrate Eqs. (1), we write them out in the form [3]

$$
\begin{aligned}
\phi_{i+1} &= (\phi_i + \psi_i\Delta t)(1 + \psi_i^2\Delta t)^{-1} + \xi_i\Delta t^{0.5}, \\
\psi_{i+1} &= (\psi_i + 2\phi_i\Delta t)(1 + \phi_i^2\Delta t)^{-1} + \eta_i\Delta t^{0.5},
\end{aligned}
\tag{2}
$$

where ξ_i and η_i are Gaussian sequences of random numbers with zero mean value and a standard deviation σ.

In the absence of an external noise, the system of equations (1) describes a relaxation process with $\phi \sim t^{-\frac{1}{2}}$ and $\psi \sim t^{\frac{1}{2}}$ as $t \longrightarrow \infty$. However, under the action of an external noise, this process transforms into the stationary stochastic processes described by the functions $\phi(t)$ and $\psi(t)$ [3, 9]. Over a wide range of the integration steps ($0.05 < \Delta t < 0.3$), a noise intensity ($\sigma_c = 0.8$) can be chosen in such a manner that the power spectra of fluctuations of $\phi(t)$ and $\psi(t)$ have the forms of $\dfrac{1}{f}$ and $\dfrac{1}{f^2}$, respectively, for noise intensities close to this value. The power spectra of fluctuations of $\phi(t)$ and

$\psi(t)$ obtained from numerical solutions to Eqs. (2) are shown in Fig. 1. Such frequency dependences of the power spectra appear also for $\Delta t < 0.005$ but for larger realization lengths. Therefore, if we had a true source of white noise being a sequence of the δ-functions following in infinitesimal intervals one after another, and could integrate such equations, then system (1) would exhibit for the corresponding power spectra the asymptotic $\frac{1}{f}$ and $\frac{1}{f^2}$ behavior as $f \longrightarrow 0$.

Noise-induced transitions in system (1) are one of its notable features. As was proposed in [10], such transitions could be found according to the number and positions of extrema of the probability-density distributions.

The numbers of extrema of the probability-density distributions $P(\psi)$ and $P(\sqrt{\phi^2\psi^2})$ for both the variable ψ and the quantity $\sqrt{\phi^2\psi^2}$, respectively, vary with the external-noise intensity in system (1); i.e., there occur two transitions induced by the noise. The positions of these extrema are adequate characteristics of transitions between stationary states of system (1). They can be identified as macroscopic stationary states of the system, while the variables ψ and $\sqrt{\phi^2\psi^2}$ represent order parameters for nonequilibrium phase transitions.

In order to illustrate these noise-induced transitions, we numerically solved system (2) with various standard deviations for the sequences of Gaussian random numbers. For a given integration step Δt at the same value of σ, the probability density for corresponding quantities was evaluated by averaging over 256 realizations containing 16384 integration time steps.

The first transition caused by a change in the number of extrema of the probability density $P(\psi)$ occurs at large intensities of the external noise ($\sigma \simeq 2\sigma_c$) and have a trivial character. In this case, the variables $\phi(t)$ and $\psi(t)$ become statistically equal. At large intensities of the external noise, the differences in the two equations of system (1) become insubstantial; as a result, the fluctuations of $\phi(t)$ and $\psi(t)$ are described by the Lorentz spectrum.

The formation of the $\frac{1}{f}$ and $\frac{1}{f^2}$ power spectra is related to the behavior of the probability density $P(\sqrt{\phi^2\psi^2})$ of the quantity $\sqrt{\phi^2\psi^2}$. If $0 < \sigma < \sigma_c$, the probability density $P(\sqrt{\phi^2\psi^2})$ has two maxima corresponding to two stationary states (Fig. 2, curve *1*). There occurs a transition at the point $\sigma = \sigma_c = 0.8$ (Fig. 2, curve *2*), because for $\sigma > \sigma_c$, the zero stationary point becomes stable (Fig. 2, curve *3*).

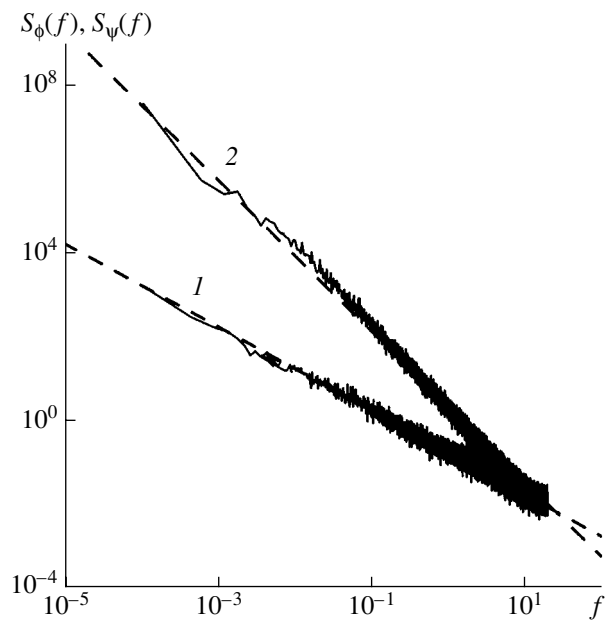It is remarkable that the critical value of the external-noise intensity, at which a qualitative change in

Fig. 1. Power spectra of fluctuations (*1*) $\phi(t)$ and (*2*) $\psi(t)$ obtained from numerical solutions to Eqs. (2) and averaged over various realizations. The dashed lines represent the dependences (*1*) $\frac{1}{f}$ and (*2*) $\frac{1}{f^2}$.
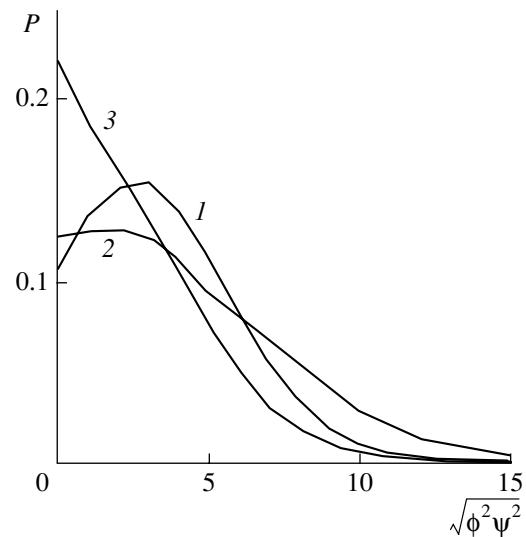

Fig. 2. Stationary probability-density distributions $P(\sqrt{\phi^2\psi^2})$ for system (2), which are calculated with the integration step $\Delta t = 0.1$: (*1*) $\sigma < \sigma_c$, (*2*) $\sigma = \sigma_c$, and (*3*) $\sigma > \sigma_c$; $\sigma_c = 0.8$.

macroscopic properties of system (1) takes place, just corresponds to the flicker spectrum. This is responsible for both the existence of a fairly wide interval of the external-noise intensities and the lack of a "fine tuning" of the system with respect to the flicker-noise behavior. This property is illustrated in Fig. 3, where the averaged value $\langle \sqrt{\phi^2\psi^2} \rangle$ (the fourth moment) is shown as a function of the external-noise intensity.
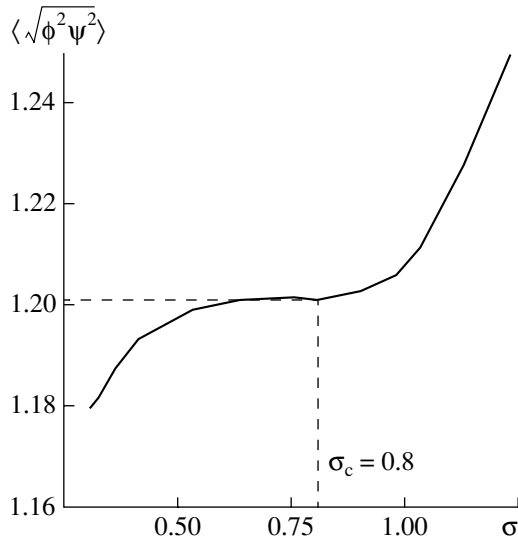
Fig. 3. Averaged value $\langle \sqrt{\phi^2 \psi^2} \rangle$ as a function of the external-noise intensity, $\Delta t = 0.1$.

Equations (1) can be generalized to the case of spatially distributed systems [8]:

$$\frac{\partial \phi}{\partial t} = D \frac{\partial^2 \phi}{\partial x^2} - \phi \psi^2 + \psi + \Gamma_1(x, t),$$

$$\frac{\partial \psi}{\partial t} = -\phi^2 \psi + \phi + \Gamma_2(x, t), \tag{3}$$

where D is the diffusion coefficient. The potential

$$\Phi = \phi^2 \psi^2 - \phi \psi + \frac{1}{2} D (\nabla \phi)^2$$

corresponds to system (3), which will be a stationary system as $t \longrightarrow \infty$ if the external noise is absent.

It is easy to generalize the conditions of a noise-induced transition to the case of a distributed system. Using cyclic boundary conditions for system (3), we found the critical value $\sigma_c = 0.7$, which corresponds to the flicker spectrum as in the case of a concentrated system.

Thus, the intersection and interaction of two nonequilibrium phase transitions can lead to the formation of a source of fluctuations with a $\frac{1}{f}$ power spectrum.

Using numerical methods, we have shown that noise-induced transitions take place in a system of two nonlinear stochastic differential equations describing the generation of fluctuations with the flicker power spectrum. The intensities of the external noise for which the critical transition occurs correspond to a $\frac{1}{f}$ power spectrum. Such a behavior does not require a fine tuning and suggests that the criticality of the system is induced by the noise.

ACKNOWLEDGMENTS

REFERENCES

1. Sh. M. Kogan, Usp. Fiz. Nauk **145**, 285 (1985) [Sov. Phys. Usp. **28**, 170 (1985)].
2. V. P. Koverda, V. N. Skokov, and V. P. Skripov, Pis'ma Zh. Éksp. Teor. Fiz. **63**, 739 (1996) [JETP Lett. **63**, 775 (1996)].
3. V. P. Koverda, V. N. Skokov, and V. P. Skripov, Zh. Éksp. Teor. Fiz. **113**, 1748 (1998) [JETP **86**, 953 (1998)].
4. V. N. Skokov, V. P. Koverda, and A. V. Reshetnikov, Pis'ma Zh. Éksp. Teor. Fiz. **69**, 590 (1999) [JETP Lett. **69**, 636 (1999)].
5. V. N. Skokov, A. V. Reshetnikov, and V. P. Koverda, Teplofiz. Vys. Temp. **38**, 786 (2000).
6. A. V. Reshetnikov, N. A. Mazheĭko, V. P. Koverda, *et al.*, Dokl. Akad. Nauk **380**, 176 (2001) [Dokl. Phys **46**, 612 (2001)].
7. A. V. Reshetnikov, A. V. Vinogradov, V. P. Koverda, and V. N. Skokov, Dokl. Akad. Nauk **374**, 481 (2000) [Dokl. Phys. **45**, 515 (2000)].
8. V. N. Skokov, V. P. Koverda, and A. V. Reshetnikov, Zh. Éksp. Teor. Fiz. **119**, 535 (2001) [JETP **92**, 535 (2001)].
9. V. P. Koverda and V. N. Skokov, Dokl. Akad. Nauk **366**, 316 (1999) [Dokl. Phys. **44**, 350 (1999)].
10. W. Horsthemke and R. Lefever, *Noise Induced Transitions. Theory and Applications in Physics, Chemistry and Biology* (Springer, Heidelberg, 1984; Mir, Moscow, 1987).

Translated by V. Chechin

The Effect of Associates with an Arbitrary Stoichiometry on Mixing Thermodynamics in Liquid Alloys

K. Yu. Shunyaev, Academician N. A. Vatolin, and V. L. Lisin

Received May 7, 2002

The model of an ideal association solution is one of the models successfully used in calculating thermodynamic characteristics of multicomponent liquid systems. Traditionally, the model is applied to solutions that have stable compounds in their solid phases. In this case, it is usually assumed that a melt consists of individual atoms of initial components and of one or several associates with a fixed stoichiometry and a minimum size. The equilibrium constants responsible for a reaction of the formation of the associates from initial components and, often, the stoichiometries of associates are adjustable parameters [1–4]. The possibility of the existence of associates composed of individual atoms was considered in the general theory of an ideal association solution [1, 5, 6]. However, only recently, a number of studies have appeared in which the existence of self-associates was taken into account in calculating particular systems [7, 8]. In [9–14], it was shown that the consideration of the self-association, even in the case of allowance for only the configurational contribution into entropy, is sufficient to qualitatively explain features of the thermodynamic properties of the process of melting metals and of thermodynamic characteristics of melting and mixing liquid eutectic alloys.

The successful use of self-associates in calculating properties of pure metals and simple eutectics makes it possible to assume that, in multicomponent melts, associates with an arbitrary stoichiometry can also exist. If we admit the existence of such associates, then, evidently, their effect must first of all be manifested in systems characterized by infinite solubility in the solid and liquid phases. However, for both simple eutectics and systems containing a stable compound in the solid phase, the consideration of associates with an arbitrary stoichiometry may, in principle, affect the magnitudes of calculated properties, as well as the qualitative pattern of their behaviors. The goal of this study is to develop a general scheme that takes into account associates with an arbitrary stoichiometry in the model of an ideal association solution and to analyze the effect of these associates on the behavior of the thermodynamic

characteristics of mixing and on a position of the liquidus line.

We now consider a binary system $A_c B_{1-c}$ whose components in the liquid phase form a solution with the complete mutual dissolution. We present this solution as an ideal solution consisting of the $A_n(i)$, $B_n(j)$, and $A_n B_m(i, j, q)$ associates. (Here, n and m are the numbers of corresponding atoms in the complex and i, j, and q are, respectively, the numbers of nearest-neighbor pairs of the AA, BB, and AB types in the complex.) Next, we assume that the energy of the complex is determined by the sum of energies of the nearest-neighbor pairs and restrict our consideration by only configurational contributions into the entropy. Then, the molar fractions of the complexes are related to each other by the following equations [10]:

$$x_{A_{n,i}} = K_{A_{n,i}} x_{A_1}^n = \exp\left(\frac{\alpha_A i}{kT}\right) x_{A_1}^n = t_A^i x_{A_1}^n,$$

$$x_{B_{n,j}} = K_{B_{n,j}} x_{B_1}^n = \exp\left(\frac{\alpha_B j}{kT}\right) x_{B_1}^n = t_B^j x_{B_1}^n, \tag{1}$$

$$x_{A_n B_m}(i, j, q) = K_{A_n B_m} x_{B_1}^n$$

$$= \exp\left(\frac{\alpha_A i + \alpha_B j + \alpha_{AB} q}{kT}\right) x_{A_1}^n x_{B_1}^m = t_A^i t_B^j t_{AB}^q x_{A_1}^n x_{B_1}^n,$$

where $x_{A_{n,i}}$, $x_{B_{n,j}}$, $x_{A_n B_m}$, x_{A_1}, and x_{B_1} are the molar fractions of the complexes $A_{n,i}$, $B_{n,j}$, and $A_n B_m$ and of the individual atoms A_1 and B_1, respectively; α_A, α_B and α_{AB} are the binding energies (taken with the opposite sign) of the AA, BB, and AB nearest-neighbor pairs; and $K_{A_{n,i}}$, $K_{B_{n,i}}$, and $K_{A_n B_m}$ are the corresponding equilibrium constants.

In this case, the system of balance equations for determining concentrations of single atoms takes the form

$$\sum_n \sum_i x_{A_{n,i}} + \sum_n \sum_j x_{B_{n,j}} + \sum_{n,m} \sum_{i,j,q} x_{A_n B_m} = 1,$$

$$c = \frac{\sum_n \sum_i n x_{A_{n,i}} + \sum_{n,m} \sum_{i,j,q} x_{A_n B_m}}{\sum_n \sum_i x_{A_{n,i}} + \sum_n \sum_j x_{B_{n,j}} + \sum_{n,m} \sum_{i,j,q} (n+m) x_{A_n B_m}}. \tag{2}$$

Institute of Metallurgy, Ural Division,
Russian Academy of Sciences,
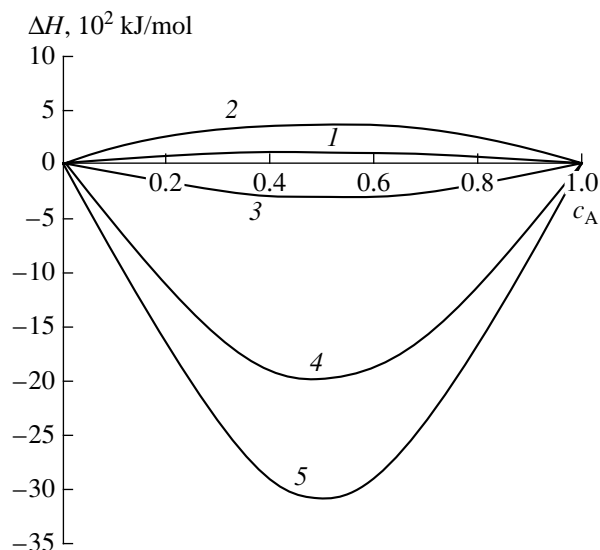*ul. Sof'i Kovalevskoĭ 18, Yekaterinburg, 620219 Russia*

Fig. 1. Dependence of the mixing enthalpy of a model alloy at $T = 1100$ K for different values of the energy parameter: $W =$ (*1*) 0; (*2*) –3000; (*3*) 3000; (*4*) 10000; and (*5*) 13000.
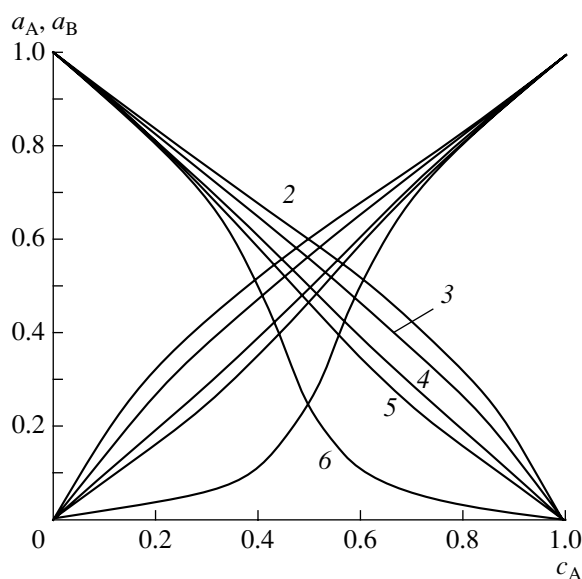

Fig. 2. Activities of components of a model alloy at $T = 1100$ K for different values of the energy parameter: $W =$ (*2*) –3000, (*3*) 3000, (*4*) 10000, (*5*) 13000, and (*6*) 30000.

The solution to the system of equations (1) makes it possible to find the molar fractions of single atoms in the solution. Afterwards, it is not difficult to calculate the thermodynamic characteristics of the system (see, e.g., [1–4, 10–13]). It is especially easy to express activities of the components in the most simple form

$$a_A = \frac{x_{A_1}}{x_{A_1}^0}, a_B = \frac{x_{B_1}}{x_{B_1}^0}, \quad (3)$$

where $x_{A_1}^0$ and $x_{B_1}^0$ are the fractions of the single atoms in the corresponding pure components at the temperature under consideration.

For performing calculations, it is necessary to know the energy parameters α_A, α_B, and α_{AB}, as well as the number of nearest-neighbor pairs of different types in

the associates. The energy parameters α_A and α_B can be estimated from the meting temperatures of the pure components [9]. Therefore, the quantity α_{AB} remains the only varied parameter. We can count the total number of pairs in the associate on the basis of the assumption that the local structure of a corresponding crystal remains unchanged in the liquid [9, 12]. In the preliminary analysis of potentialities of our model, we employ the approximation of a linear chain for the associate structure, as was done for simple eutectics in [10]. Such a simplification makes it possible to readily perform the summation in Eq. (2). In this case, in accordance with the analysis performed in [10], the loss in the accuracy of the calculated properties is no more than 10%.

Figures 1 and 2 and Table 1 show the calculated results for some properties of a model alloy whose components have melting temperatures of 700 and

Table 1. Properties of an equi-atomic model melt at $T = 1100$ K as a function of the energy parameter W

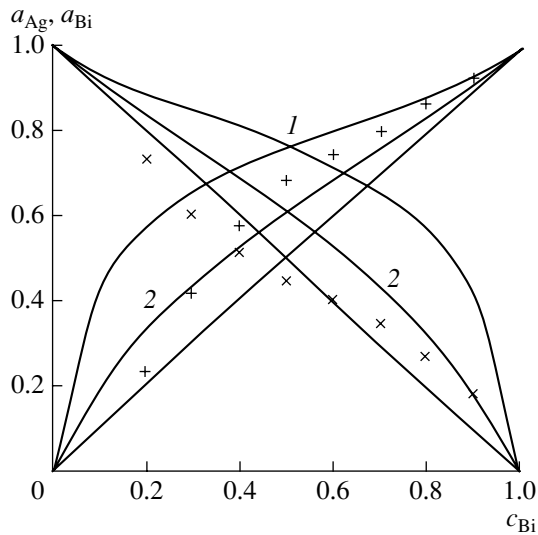| W, 10^3 J/mol	ΔH^M, J/mol	ΔG^M, J/mol	ΔS^M, J/(mol K)	a_A
–60	289	–3535	3.476	0.68
–30	515	–3670	3.805	0.669
–10	641	–4159	4.364	0.635
–6	534	–4382	4.469	0.619
–3	370	–4600	4.518	0.605
–2	295	–4684	4.526	0.54
0	104	–4872	4.524	0.587
3	–300	–5210	4.464	0.566
10	–1987	–6329	3.947	0.501
30	–12460	–12590	0.122	0.253

Fig. 3. Activities of components of Ag–Bi alloy at $T = 1000$ K. The calculations are performed with allowance for (*1*) only self-associates and (*2*) associates with an arbitrary stoichiometry (+ and × are the experimental points taken from [15]).
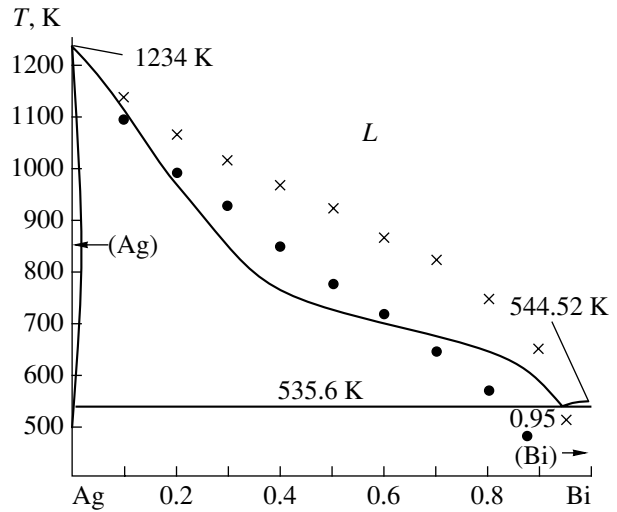

Fig. 4. Phase diagram of the Ag–Bi system [15]. The calculations of the position of the liquidus line are performed with allowance for (●) only self-associates and (×) associates with an arbitrary stoichiometry.

1000 K. The parameters α_A and α_B were determined from the melting temperatures of the components, while the parameter $W = [\alpha_{AB} - 0.5(\alpha_A + \alpha_B)]$ varied. As was expected, the model allows us to describe both positive and negative deviations from the ideal behavior. Note that the negative deviations can be arbitrarily large, whereas, at large positive values of *W*, the behavior of thermodynamic characteristics of mixing becomes the same as for systems with the strong interaction of components. Another situation is observed for negative values of *W* when the formation of pairs of the AB type is unprofitable from the energy standpoint. For small values of *W*, an increase in positive values of the mixing enthalpy is observed, as long as the energy loss can be compensated by the configurational entropy. On further increasing the value of *W*, the mixing enthalpy

begins to decrease. The mixing entropy also passes through its maximum but at other considerably smaller values of *W*. At the same time, activities of the components and the mixing free energy vary monotonically (Table 1). Moreover, it turned out that the model can describe the situation when the mixing enthalpy is negative and positive deviations from the Raoult law are observed for activities of the components. This is an additional illustration in favor of the model proposed. Despite the fact that this model contains only one varied parameter (of the interchange-energy type), it is capable of treating a much more diverse range of behaviors compared to other similar models. For example, unlike the model of a regular solution, in which the sign of the deviation of all properties from ideality is determined by only the sign of the energy parameter, in

Table 2. Calculated and experimental properties of liquid Ag–Bi alloys at $T = 1000$ K. Subscripts correspond to (*1*) calculation with allowance for only self-associates; (*2*) calculation with allowance for associates with an arbitrary stoichiometry. The experimental results are taken from [15]

c_{Bi}	ΔH_1	ΔH_2	$\Delta H_{exp.}$	$-\Delta G_1$	$-\Delta G_2$	$-\Delta G_{exp.}$
	J/mol			J/mol		
0.2	398	276	473	1728	3047	4305
0.3	474	352	699	2017	3655	4489
0.4	514	396	946	2175	3992	5100
0.5	525	410	1222 ± 210	2226	4102	4945 ± 1050
0.6	508	395	1540	2177	3995	4515
0.7	462	350	1711	2022	3660	3920
0.8	380	273	1582	1735	3053	3096
0.9	246	160	1046	1243	2055	1954
1.0	0	0	0	0	0	0

our model, such an unambiguous dependence is absent. The character of a property is determined as a resulting value obtained from several contributions, e.g., from the direct pair contribution into the energy and an indirect configurational contribution. In this case, the result depends on the value of the energy parameter, the melt temperature, and the melting temperatures of the components.

The calculated results for the mixing thermodynamic characteristics and the position of the liquidus line for the binary Ag–Bi system are presented in Figs. 3 and 4 and in Table 2 (the value of the parameter *W* is equal to –3500 J/mol). For comparison, the calculation results obtained within the model taking into account only self-association of the components are also presented. As is seen, in the latter case, the agreement between the calculated and experimental results becomes considerably better for the entire totality of calculated properties.

ACKNOWLEDGMENTS

REFERENCES

1. I. Prigogine and R. Defay, *Chemical Thermodynamics* (Longmans Green & Co., London, 1954; Nauka, Novosibirsk, 1966).

2. K. Wasai and K. Mukai, J. Japan Inst. Met. **46** (3), 266 (1982).

3. F. Sommer, Z. Metallkd. **73** (2), 72 (1982).

4. R. Schmid and Y. A. Chang, CALPHAD: Comput. Coupling Phase Diagrams Thermochem. **9** (4), 363 (1985).

5. H. Kehiaian, Bull. Acad. Pol. Sci., Ser. Sci., Chim. **12** (7), 497 (1964).

6. A. G. Morachevskiĭ, A. G. Mokrievich, and E. A. Maĭorova, Zh. Obshch. Khim. **59** (9), 1927 (1989).

7. M. Ivanov, Z. Metallkd. **82** (1), 53 (1991).

8. R. N. Singh and F. Sommer, Z. Metallkd. **83** (7), 533 (1992).

9. N. K. Tkachev, K. Yu. Shunyaev, A. N. Men', and N. A. Vatolin, Rasplavy **2** (1), 3 (1988).

10. N. K. Tkachev, K. Yu. Shunyaev, A. N. Men', and N. A. Vatolin, Dokl. Akad. Nauk SSSR **302**, 153 (1988).

11. K. Yu. Shunyaev and N. A. Vatolin, Dokl. Akad. Nauk **332**, 167 (1993) [Dokl. Phys. **38**, 391 (1993)].

12. K. Yu. Shunyaev and N. A. Vatolin, Rasplavy, No. 5, 28 (1993).

13. K. Yu. Shunyaev and N. A. Vatolin, Metally, No. 5, 96 (1995).

14. K. Yu. Shunyaev, N. C. Tkachev, and N. A. Vatolin, Thermochim. Acta **314**, 299 (1998).

15. R. Hultgren, P. R. Desai, D. T. Hawkins, *et al.*, *Selected Values of the Thermodynamic Properties of Binary Alloys* (ASM, Metal Park Ohio), 1973).

Translated by Yu. Vishnyakov

=========== **PHYSICS** ===========

An Analytical Model of the Active Medium and the Optimum Resonator for a CO Laser

I. I. Litvinov

Presented by Academician B.V. Bunkin May 23, 2002

Received May 24, 2002

Electric-discharge CO lasers have a uniquely high efficiency and energy extraction per unit volume of gas flow rate [1–4]. The processes of excitation and lasing in them involve a large number (up to ~100) of vibrational levels (with allowance for VV′ exchange with N_2 molecules). Therefore, theoretical models of these lasers are complicated, and basic results are usually obtained in cumbersome computer calculations. In addition, a number of problems remain.

Even in the first calculations, it was shown that the efficiency of CO lasers is significantly higher (~50–70%) [5, 6] than experimental values ~20–40% [2–4]. In order to bring the calculations and experiments into agreement, the pumping efficiency η_p of the vibrational levels in CO molecules, which is normally very high (up to ~95%), was artificially reduced (down to ~75%) [7]. At the same time, experimental evidence has been published that the efficiency of CO lasers can be very high (~60% [1]), which agrees with theoretical values without fitting the parameters. For some reason, these data are ignored. However, they demonstrate that other causes can also be responsible for underestimating the efficiency in experiments.

For example, the efficiency of solid-state lasers was also overestimated [8] even in quite adequate models [9]. Now, this problem is solved by simultaneously fitting the pumping efficiency η_p' (with allowance for the Stokes losses) and the coefficient of internal losses α_i, which determine the resonator efficiency η_R' and the total efficiency of a laser ($\eta_l = \eta_p' \eta_R'$). For this aim, it is sometimes necessary, on the contrary, to increase the calculated efficiency and to decrease η_R' (due to increasing α_i), for which agreement in the optimum transmission of the output mirror T_2 is also achieved. As a result, the effects from η_p' and α_i are separated, and they are determined simultaneously as a pair.

—————————

Scientific Council on Cybernetics,
Russian Academy of Sciences,
ul. Vavilova 40, Moscow, 117333 Russia

However, the situation for solid-state lasers is much simpler. For these lasers, it is possible to independently (experimentally) determine the basic laser parameters of an active medium—unsaturated gain k_0, saturation intensity I_0, and loss factor α_i—because exclusively simple (linear) kinetics for four-level media enabled one to develop the theory of the optimum resonator [10, 11]. Thus, theory and experiment can successfully complement each other in this case.

For CO lasers, it would be desirable to construct an equally simple model that would retain the main features of actual media. But such a model has not been developed yet. Moreover, the true place of the active media of CO lasers among the other known types of *N*-level media is also unknown. Here, even parameters k_0 and I_0 are not defined properly, and parameter α_i for CO lasers is completely absent. However, almost all separate elements of such a model have already been available for a long time. These are the familiar analytical model of the active medium of CO lasers [12–14] and the resonator model mentioned above [10, 11]. Although the characteristics of the active medium of CO lasers are much different, this problem can be completely solved.

1. FOUNDATIONS OF AN ANALYTICAL MODEL OF THE ACTIVE MEDIUM FOR CO LASERS

As is known [12], the active medium in CO lasers operates principally on the anharmonicity of vibrational levels in a CO molecule with the key role of nonlinear (pair) VV exchanges, i.e., has no analogs among other known types of linear *N*-level systems. However, under reasonable assumptions, this complex system can be described by one differential equation for the level distribution function f_v. This equation has the form of a conservation law for the flux of quanta F_v in v (per CO molecule):

$$\frac{dF_v}{dv} = -P_{v+1} f_v - \frac{I_v k_v}{h\nu_v}. \tag{1}$$

Here, the first and second terms on the right-hand side are the rate of the VT relaxation on a given level v and

the rate of the depopulation of this level in the resonator with intensity I_v and gain k_v (per CO molecule). In this section, the basic notation corresponds to the notation used in [13].

In the simplest case, the expression for flux F_v has the form

$$F_v = \left(\frac{2Q_{10}}{\delta_{vv}^3}\right)(v+1)^2 f_v^2 \left(\frac{2\Delta E}{T} - \frac{d^2 \ln f_v}{dv^2}\right). \quad (2)$$

Here, Q_{10} is the constant of the pair VV exchange between the two lower levels, δ_{vv} is the inverse VV-exchange radius, $\Delta E = 19.1$ K is the anharmonicity energy, and T is the temperature of the gas mixture.

At small values $v < i^*$, the solution to Eqs. (1) and (2) for f_v is close to the left branch (falling off steeply) of the Treanor formula [12, 13]

$$f_v = f_0 \exp\left(\frac{E_1 v}{T_1} - \frac{\Delta E v(v-1)}{T}\right). \quad (3)$$

Here, $E_1 = 3084$ K is the energy of the first vibrational level; T_1 is the filling temperature of lower levels, which is determined by the pumping power density $w_p = \eta_p j_e E = \eta_p w_{el}$, where η_p is the pumping efficiency; and i^* is the minimum point in the Treanor formula. At $T \sim 100$ K, $i^* \sim 4$–6.

Conversely, the solution to Eq. (1) for $v > i^*$ (in the absence of lasing) has a long section (up to $v \sim 20$–40), where f_v decreases smoothly (plateau region). Further, this section is replaced by a section where f_v falls steeply due to the sharp (exponential) rise in the weak term responsible for the VT exchange in Eq. (1).

The smallness of the VT-exchange term in Eq. (1) on the plateau is equivalent to the constant flux of quanta in v ($F_v \approx F_0 = $ const). Therefore, f_v becomes much simpler:

$$f_v = \frac{c}{v+1}, \quad F_0 = \frac{4Q_{10}\Delta E}{\delta_{vv}^3 T} c^2. \quad (4)$$

The flux F_0 is related to the constant c (the filling factor of the levels) by a nonlinear dependence: $F_0 \sim c^2$, or, conversely, $c \sim \sqrt{F_0}$.

The gain entering into Eq. (1) has the form

$$k_v = \sigma_v \left(\gamma_v f_v + \frac{df_v}{dv}\right), \quad (5)$$

where σ_v is the amplification cross section and γ_v is the rotary factor. For the lasing zone ($v \sim 5$–15), we have $\sigma_v \approx \sigma_0(v+1)$ and $\gamma_v \approx \gamma_m = \frac{2Bj_m}{T} \approx$ const, where

$j_m \approx \sqrt{\frac{T}{B}}$ and $B \approx 2.78$ K is the rotational constant of a CO molecule.

However, in the presence of lasing, the distribution of f_v differs from (4) [13] and is determined from the condition of equality between gain (5) and the loss factor in the resonator (per CO molecule) $\Delta_0 = \frac{\ln(1/R)}{2L_a N_c}$, where $R = R_1 R_2$ is the reflection coefficient of the mirrors and L_a is the length of the active medium.

Above the lasing zone (as for the plateau section), factor c in solution (4) must be replaced by smaller factor [13] $k = \frac{\Delta_0}{\gamma_m \sigma_0}$, which is determined by threshold Δ_0 and has two same meaning. As a result, the flux of quanta F_k outgoing upward into the zone of VT relaxation is smaller than the incoming flux F_0 by the factor $\frac{k^2}{c^2}$ and their difference $1 - \frac{k^2}{c^2}$ gives the part of this flux that is spent for lasing.

The flux F_0 is related to the pumping power density of the lower levels w_p and to the electric power in the discharge w_{el} as $w_p \approx h\nu_1 F_0 N_c = \eta_p w_{el}$, where $\nu_1 = \frac{E_1}{h}$ is the frequency corresponding to the 1–0 transition in a CO molecule. Hence, the power density of lasing per unit volume of the active medium has the form

$$w_g = h\bar{\nu}_g (F_0 - F_k) N_c = \eta_p' \left(1 - \frac{k^2}{c^2}\right) w_{el}; \quad \eta_p' = \eta_p \eta_v, \quad (6)$$

where η_p' is the pure pumping efficiency (with allowance for Stokes losses), $\bar{\nu}_g$ is the mean frequency in the lasing spectrum, and $\eta_v = \frac{\bar{\nu}_g}{\nu_1}$ is the quantum efficiency due to a decrease in the value of a quantum in the lasing zone $\left(\frac{2\Delta E}{E_1} \approx 1.24\%$ per transition$\right)$.

As a whole, these relationships complete the model of the active medium of CO lasers for the quasistationary lasing mode [13, 14]. However, this analysis was not properly developed for the resonator. For example, the fundamentally important factor $\left(1 - \frac{k^2}{c^2}\right)$ is treated there as the total efficiency of the resonator η_R. However, this is not entirely the case. In order to provide a better insight into this problem and to obtain the closed model of CO lasers, we first consider how this problem is solved for simpler media.

2. FOUNDATIONS OF THE THEORY OF THE OPTIMUM RESONATOR FOR FOUR-LEVEL MEDIA

In the stationary regime, the main rate equation has the form

$$\frac{w'_p}{h\nu_g} = \frac{kI}{h\nu_g} + \frac{n_3}{\tau_*}. \tag{7}$$

Here, the left-hand side is the pumping rate determined by the pure pumping power (with allowance for Stokes losses) $w'_p = \eta'_p w_{e1}$, and the right-hand side is the depopulation rate of the upper laser level with population n_3 under the action of radiation with intensity I and the relaxation of this level with lifetime τ_*. Hence, taking into account the evident relation $k = n_3 \sigma_g$, we find the following fundamental saturation formula for the gain [10, 11]:

$$k(I) = k_0\left(1 + \frac{I}{I_0}\right)^{-1}; \quad k_0 = \frac{\sigma_g \tau_*}{h\nu_g} w'_p;$$

$$I_0 = \frac{h\nu_g}{\sigma_g \tau_*} \tag{8}$$

or, on the contrary,

$$\frac{I}{I_0} = \frac{k_0}{k} - 1.$$

Here, I is the total intensity of two counterpropagating waves in the resonator.

By definition of k_0 and I_0, it follows that k_0 for these media rises strictly linearly with w'_p, whereas I_0 is independent of w'_p. In addition, we arrive at the important relation $w'_p \equiv k_0 I_0$, which will be used below in the model of CO lasers.

Finally, for the power density of lasing in the active medium, it follows from (7) and (8) that

$$w_g = kI = k_0 I_0\left(1 - \frac{k}{k_0}\right). \tag{9}$$

As follows from the derivation of Eq. (9), the multiplier in the parentheses is the efficiency of producing the laser power in the resonator η'_R, which is determined here only by relaxation losses in the active medium. To obtain the total efficiency η_R, it should be multiplied by the output efficiency from the resonator η''_R, which presents all other losses. When the losses in the mirrors are neglected, the output efficiency can be written as $\eta''_R = \frac{k_R}{k_{th}}$, where $k_R = -\frac{\ln(1 - T_2)}{2L_a}$ is the coefficient of useful losses and $k_{th} = k_R + \alpha_i$ is the total (threshold) gain.

The above discussion indicates that the total efficiency of the resonator is written as

$$\eta_R = \eta'_R \eta''_R = \left(1 - \frac{k_{th}}{k_0}\right)\left(1 - \frac{\alpha_i}{k_{th}}\right). \tag{10}$$

Hence, for the maximum efficiency, we find the important relations

$$k^m_{th} = \sqrt{\alpha_i k_0}, \quad \eta^m_R = \left(1 - \sqrt{\frac{\alpha_i}{k_0}}\right)^2, \tag{11}$$

which play the central role in the theory of the optimum resonator for four-level media.

It is easy to see that the both factors entering into Eq. (10) make the same contribution to the decrease in the efficiency at the maximum point. Therefore, the second factor in Eq. (10) cannot be neglected.

3. GENERALIZED THEORY OF THE OPTIMUM RESONATOR OF A CO LASER

Comparing the results and conclusions of Sections 1 and 2, we conclude that the expression in the parentheses in Eq. (6) is the production efficiency of the laser power η'_R in the active medium of a CO laser. In the detailed form, this expression can be written as

$$w_g = \Delta'_0 N_c \int I_v dv \equiv k_{th} I = w'_p\left(1 - \frac{k^2}{c^2}\right), \tag{12}$$

where $\Delta'_0 = \frac{k_{th}}{N_c}$ is the revised (with allowance for α_i) threshold per CO molecule and I is the integrated intensity (in v) of radiation in the resonator.

As is seen, this expression is quite similar to analogous expression (9) for four-level media. It only remains to transform the component with $\frac{k^2}{c^2}$ in Eq. (12) to the customary (laser) form

$$\frac{k}{c} = \frac{\Delta'_0 N_c / \gamma_m \sigma_0}{c N_c} \equiv \frac{k_{th}}{k_0}, \quad k_0 = \gamma_m \sigma_0 N_c c. \tag{13}$$

The new parameter k_0 introduced here is the generalized unsaturated gain of the active medium in CO lasers.

To demonstrate this fact, we take into account that, under the typical conditions for $T = 100$ K, $j_m \approx 6$ and $\gamma_m \approx 1/3$ for CO lasers. Therefore, the contribution of the term with the derivative in Eq. (5) is small in the plateau region. As a result, we have

$$k_v \approx \gamma_m \sigma_v f_v = \gamma_m \sigma_0 c \equiv \frac{k_0}{N_c}. \tag{14}$$

Thus, because of the inverse dependence of σ_v and f_v on $v + 1$, k_v is almost constant within the lasing zone. This behavior determines the importance of the parameter k_0 for these media.

Consequently, the expression in the parentheses in Eq. (12) is actually the efficiency η'_R of laser-power production in the active medium of CO lasers. The quadratic dependence $\dfrac{k^2}{c^2}$ in Eq. (12) [instead of the linear dependence in Eq. (9)] is the direct consequence of the main mechanism of the pair VV exchange in the kinetics of CO lasers.

As a result, in contrast to solid-state lasers, the power of CO lasers is proportional to the square of the population of laser levels ($w'_p \sim c^2$), whereas the gain, to the population ($k_0 \sim c$). This is the main difference of the nonlinear active medium of CO lasers from conventional linear media.

Hence, the gain of CO lasers has a specific (nonlinear) dependence $k_0 \sim \sqrt{w'_p}$. This simple dependence is clearly pronounced in many experiments and detailed numerical simulations of CO lasers. In our case, it is an obvious consequence of the main VV-exchange mechanism.

Developing the analogy further and rewriting Eq. (12) in the form

$$w_g = k_{th} I = k_0 I_0 \left(1 - \frac{k_{th}^2}{k_0^2} \right), \qquad (15)$$

we find the new (energy-balance) definition for the intensity I_0 in CO lasers:

$$I_0 \equiv \frac{w'_p}{k_0} \sim c \sim \sqrt{w'_p}. \qquad (16)$$

Thus, the quantity I_0 introduced here is proportional to $\sqrt{w'_p}$, whereas, for the four-level media, it is independent of w'_p.

Intensity I_0, as well as k_0, can be written in terms of the pumping power w_{el}, flux F_0, and other parameters of a CO molecule.

In turn, Eq. (15) provides the direct relation:

$$\frac{I}{I_0} = \frac{k_0}{k_{th}} \left(1 - \frac{k_{th}^2}{k_0^2} \right) = \frac{k_0}{k_{th}} - \frac{k_{th}}{k_0}, \qquad (17)$$

which differs significantly from analogous dependence (8) for solid-state lasers. Considering this relation as an implicit (quadratic) equation for the inverse

dependence $k_{th}(I)$ and normalizing k_{th} to k_0 and I to I_0, we obtain

$$\bar{k}_{th}(\bar{I}) = \sqrt{1 + \left(\frac{\bar{I}}{2} \right)^2} - \frac{\bar{I}}{2}. \qquad (18)$$

This formula for the CO lasers is of the same fundamental importance as the analogous dependence $\bar{k}_{th}(\bar{I}) = (1 + \bar{I})^{-1}$ for four-level media.

Despite of different forms, the both dependences have the similar shape of monotonically falling curves with the same asymptotics $\bar{k}_{th} \sim 1/\bar{I}$. At the same time, curve (18) passes higher than curve (8) and its slope at small $\bar{I}$ is equal to half the slope of curve (8).

Returning to the optimum resonator of CO lasers, we write, by analogy with Eq. (10), the total resonator efficiency in the form

$$\eta_R = \eta'_R \eta''_R = \left(1 - \frac{k_{th}^2}{k_0^2} \right) \left(1 - \frac{\alpha_i}{k_{th}} \right). \qquad (19)$$

The optimum value of $\bar{k}_{th}^m$ is now determined by solving the cubic equation. For small relative losses $\bar{\alpha} = \dfrac{\alpha_i}{k_0}$, it is equal to

$$\bar{k}_{th}^m \cong \left(\frac{\bar{\alpha}}{2} \right)^{1/3} \left(1 + \frac{1}{3} \left(\frac{\bar{\alpha}}{2} \right)^{2/3} \right). \qquad (20)$$

Since $\bar{\alpha}$ is small, the first term is usually sufficient. In this case, the maximum efficiency of the resonator of a CO laser equals

$$\eta_R^m = \left(1 - \left(\frac{\bar{\alpha}}{2} \right)^{2/3} \right) \left(1 - 2 \left(\frac{\bar{\alpha}}{2} \right)^{2/3} \right). \qquad (21)$$

For comparison, the same quantities for four-level media in the same notation are $\bar{k}_{th}^m = \sqrt{\bar{\alpha}}$ and $\eta_R^m = (1 - \sqrt{\bar{\alpha}})^2$.

Thus, losses in the power output in CO lasers are twice as large as losses in the energy extraction. Therefore, the contribution of the last component in Eq. (19) and (21) cannot be ignored.

Figure 1 shows two components (η'_R and η''_R) and the total resonator efficiency η_R for (solid lines) the active medium of CO lasers and (dashed lines) four-level media at the same losses $\bar{\alpha} = 0.1$.

It is natural that the components η''_R coincide for the both media, whereas η'_R significantly differ. For four-level media, η'_R decreases linearly, whereas for the

active medium of CO lasers, it decreases parabolically and, therefore, passes higher than the former curve.

Therefore, the total efficiency of the resonator for CO lasers, which is equal to the product of the functions η_R' and η_R'', also passes higher than the value for four-level media. In addition, its maximum value η_R^m indicated by asterisk, as is seen in Fig. 1, is always higher than the value for four-level media and is achieved at higher $\bar{k}_{th}$.

For the same losses $\bar{\alpha} = 0.1$ for the four-level media and the active medium of CO lasers, we have

$$\bar{k}_{th}^m = 0.316 \text{ and } 0.385, \text{ and } \eta_R^m = 0.467 \text{ and } 0.630, \quad (22)$$

respectively. As is seen, the optimum values of $\bar{k}_{th}^m$ in a CO laser are significantly higher (in the given case, by 21.5%) and, despite the higher threshold, the maximum efficiency η_R^m is also larger (by ~35%).

Figure 2 shows the optimum thresholds $\bar{k}_{th}^m$ and the maximum efficiencies η_R^m in these two models. The notation of the curves is the same as in Fig. 1. However, for CO lasers, solid curves are the exact calculations by Eq. (19), whereas dash–dotted and short dashed curves are the calculations by Eqs. (20) and (21) without and with the second term in Eq. (20), respectively. Thus, in the majority of cases (up to $\bar{\alpha} \sim 0.2$), Eqs. (20) and (21) including the most simple one [without the second term in Eq. (20)] are enough.

4. EXPERIMENTAL EVIDENCE OF THE EFFECTIVENESS OF THE MODEL OF CO LASERS

Since the new model of CO lasers is the complete analog of the classical model for four-level media, it can be successively applied in all cases where the classical model is used for solid-state lasers, in particular, for the recalculation of the three basic parameters of the active medium (k_0, I_0, and α_i) using the experimental information on the output laser power (for three values of transmission T_2), the correction of the constants of the VV exchange, and determination and elimination of the causes responsible for decreasing the efficiency of CO lasers.

Such a treatment was actually performed for a high-power subsonic CO laser [4]. The table presents the two triple of the laser parameters for one of the regimes with the specific energy contribution $w_{el} = 25$ W/cm³ and the main characteristics of the CO laser resonator, which were recalculated on their basis.

The new triple of the parameters seemingly does not differ from the initial one. Moreover, the direct use of each of the two triples provides the same result for the
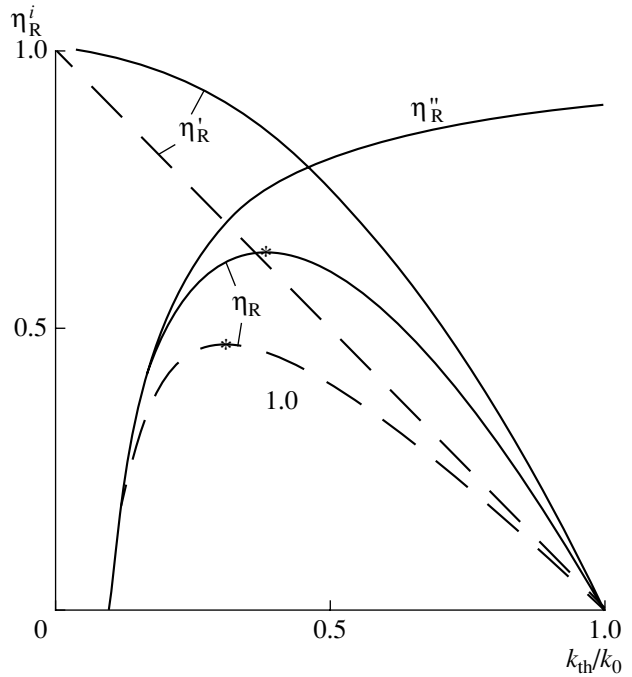

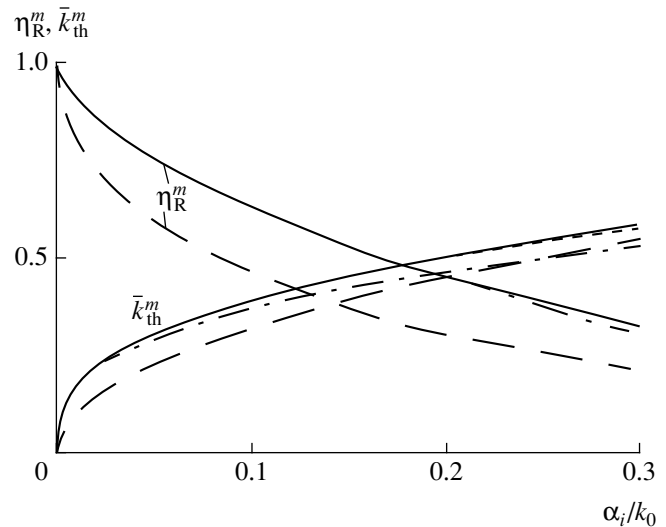**Fig. 1.** Components of the resonator efficiency vs. the relative threshold.

Fig. 2. Optimum parameters of the resonator vs. the relative losses.

output power. On the other hand, the decrease in all three parameters in the model of CO lasers and the corresponding increase in η_R^m must lead to a change in the other (input) characteristics of CO lasers. Thereby, degeneracy between these two models is removed. Let us compare the calculated and measured values of w_{el}.

According to Sections 2 and 3, the pure pumping power density is determined as $w_p' = k_0 I_0 = \eta_p' w_{el}$. The values of the internal efficiencies η_p and η_v can easily

Table

Model	k_0, m^{-1}	I_0, kW/cm^2	α_i, m^{-1}	$\bar{k}_{th}^m$	η_R^m	η_R'	η_R''
Four-level	1.40	2.90	0.290	0.455	0.297	0.545	0.545
CO laser	1.17	1.52	0.095	0.3575	0.674	0.872	0.773

be found. For the $N_2 + CO$ medium, we have $\eta_p \approx 0.85$ [7, 15], and the quantum efficiency η_v of the process consisting of three stages: carrying excitation in N_2 up to sixth–seventh level, its resonant transfer to the lower level in CO, and then its carrying upwards to the CO lasing zone with $\bar{v}_g \sim 8$ [7, 13] is also equal to ≈ 0.85.

As a result, the total pumping efficiency is $\eta_p' \approx 0.70$.

Dividing the table values of w_p' by η_p', we find the desired energy-contribution power $w_{el} = 58.0$ and 25.4 W/cm^3 in the models of four-level media and CO lasers, respectively. Since the latter value almost coincides with the experimental value, whereas the former value is far from it, the new model of CO lasers is undoubtedly adequate.

Considerable induced losses α_i in the active medium of CO lasers can be one of the main causes responsible for underestimating the efficiency. For example, their suppression ($\eta_R'' \longrightarrow 1$) increases the total efficiency of CO lasers by a factor of ~ 1.3 that approaches it to the values given in [1].

In conclusion, we emphasize that the above relationships were found for the quasistationary operation mode of CO lasers when the pulse duration (or the flight time through an active medium) significantly exceeds the time of VV exchange. Otherwise, as for solid-state lasers, it is necessary to take into account the energy consumption on increasing inversion to the threshold with allowance for the specific character of this new active medium.

REFERENCES

1. M. M. Mann, AIAA J. **14** (5), 549 (1976).
2. N. G. Basov, V. A. Danilychev, A. A. Ionin, and I. B. Kovsh, Tr. Fiz. Inst. im. Lebedeva Akad. Nauk SSSR **116**, 54 (1980).
3. A. A. Ionin, Kvantovaya Élektron. (Moscow) **20**, 113 (1993).
4. A. S. Golovin, V. A. Gurashvili, I. V. Kochetov, *et al.*, Kvantovaya Élektron. **23**, 405 (1996).
5. R. E. Center and G. E. Caledonia, J. Appl. Phys. **46**, 2215 (1975).
6. Yu. B. Konev, I. V. Kochetov, and V. G. Pevgov, Zh. Tekh. Fiz. **48** (5), 977 (1978) [Sov. Phys. Tech. Phys. **23**, 571 (1978)]; Zh. Tekh. Fiz. **49** (6), 1266 (1979) [Sov. Phys. Tech. Phys. **24**, 701 (1979)].
7. A. A. Ionin, V. S. Kazakevich, I. V. Kovsh, *et al.*, Preprint No. 232, FIAN (Fiz. Inst. im. Lebedeva Akad. Nauk SSSR, Moscow, 1982).
8. A. A. Mak, L. N. Soms, V. A. Fromzel', and V. E. Yashin, *Lasers on Neodymium Glass* (Nauka, Moscow, 1990).
9. I. I. Litvinov, E. D. Lyumkis, and S. S. Filippov, Preprint No. 135, IPM AN SSSR (Inst. Prikl. Mat. Akad. Nauk SSSR, Moscow, 1976); Preprint No. 4, IPM AN SSSR (Inst. Prikl. Mat. Akad. Nauk SSSR, Moscow, 1977).
10. W. W. Rigrod, J. Appl. Phys. **34**, 2602 (1963).
11. *Methods of Calculations of Optical Quantum Generators*, Ed. by B. I. Stepanov (Nauka i Tekhnika, Minsk, 1966), Vol. 1.
12. B. F. Gordiets, A. I. Osipov, and L. A. Shelepin, *Kinetic Processes in Gases and Molecular Lasers* (Nauka, Moscow, 1980; Gordon and Breach, New York, 1988).
13. A. P. Napartovich, I. V. Novobrantsev, and A. N. Starostin, Kvantovaya Élektron. **4**, 2125 (1977).
14. S. A. Zhdanok, I. V. Kochetov, A. P. Napartovich, *et al.*, Dokl. Akad. Nauk SSSR **241** (1), 76 (1978) [Sov. Phys. Dokl. **23**, 485 (1978)].
15. N. G. Basov and I. B. Kovsh, Izv. Akad. Nauk SSSR, Ser. Fiz. **48**, 2290 (1984).

Translated by Yu. Vishnyakov

=== **PHYSICS** ===

Homogeneous Nucleation in a Superheated Crystal. Molecular-Dynamic Simulation

G. É. Norman and V. V. Stegaĭlov

Presented by Academician V.P. Skripov April 14, 2002

Received May 6, 2002

By the method of molecular dynamics, various equilibrium characteristics of many-particle systems are determined: equation of state, radial distribution function, heat capacity, elastic moduli, diffusion coefficient, etc. The value of a quantity being calculated is obtained by averaging its instantaneous value over a sampling of statistically independent points on a certain equilibrium molecular-dynamic (MD) trajectory along which the thermodynamic parameters of the system are invariable. In particular, by this method, the equation of state for superheated crystals and characteristics of their melting were calculated in [1–6].

When investigating nonequilibrium phenomena, we cannot use a set of points in a single MD trajectory for averaging a desired quantity. In this case, it is necessary to consider an ensemble in a certain sense of independent trajectories. Formation of such an ensemble represents a nontrivial problem whose solution depends on specific features of the nonequilibrium process.

In this paper, the method of molecular dynamics is applied for simulating a homogeneous-nucleation process (formation of nuclei) in a superheated crystal. Specific features of the simulation are considered, which are associated with a finite calculation accuracy and instabilities of trajectories inherent in many-particle dynamical systems. An approach is proposed for averaging the calculated data, which allows us to obtain the estimates of such physical parameters as the rate and the activation energy of homogeneous nucleation.

THE MODEL AND CALCULATION METHOD

The system under study represents a face-centered crystal of particles whose interaction energy is determined by a soft-repulsion potential $U = \varepsilon \left(\dfrac{\sigma}{r} \right)^n$. The uniformity of the potential makes it possible to describe

the thermodynamic state of the system by a single normalized parameter

$$X = 2^{-1/2} \rho m^{-1} \sigma^3 \left(\frac{\varepsilon}{k_{\mathrm{B}} T} \right)^{3/n} \sim \rho T^{-3/n},$$

where ρ is the density, m is the atomic mass, k_{B} is the Boltzmann constant, and T is temperature [7, 8]. In this case, the virial theorem is valid, according to which $(n + 2)K = nE + 3PV$, where $K = \dfrac{3 k_{\mathrm{B}} T N}{2}$ and E are the average kinetic and total energies of the system, P is pressure, V is the volume of the system, and N is the number of particles in it.

The model system contained N particles in a basic cubic cell of the volume. The calculations were carried out for $N = 108, 256, 500$, and 864 with periodic boundary conditions. For the numerical integration of classical equations of motion, the Euler–Störmer calculation scheme of the second order of accuracy was applied [9]. The integration step h varied within the range 0.001–0.01 $\Big($ here and below, normalized units are employed, in which $\varepsilon = \sigma = m = 1$ and time is expressed in units of $\left(\dfrac{m \sigma^2}{\varepsilon} \right)^{1/2} \Big)$. The energy E in the process of calculations is, on the average, constant.

The initial configuration of the system was an ideal face-centered lattice in which particles possessed arbitrary velocities. Then, the system dynamics were calculated for a number of steps until the particle-velocity distribution became Maxwellian. Starting parameters were adjusted in such a manner that in the thermodynamic-equilibrium state, the density and temperature of the system corresponded to a stable solid crystal. Afterwards, gradual heating was carried out, namely, the particle velocities were simultaneously scaled: $\mathbf{v} \longrightarrow (1 + \delta)\mathbf{v}$, where $0 < \delta \ll 1$. Then, 10^4 steps were calculated, each of them being $h = 0.001$. The procedure was then repeated. As a result, the temperature of the system became higher than the melting temperature of a solid

Institute of Thermal Physics of Extremal States,
Associated Institute for High Temperatures,
Russian Academy of Sciences,
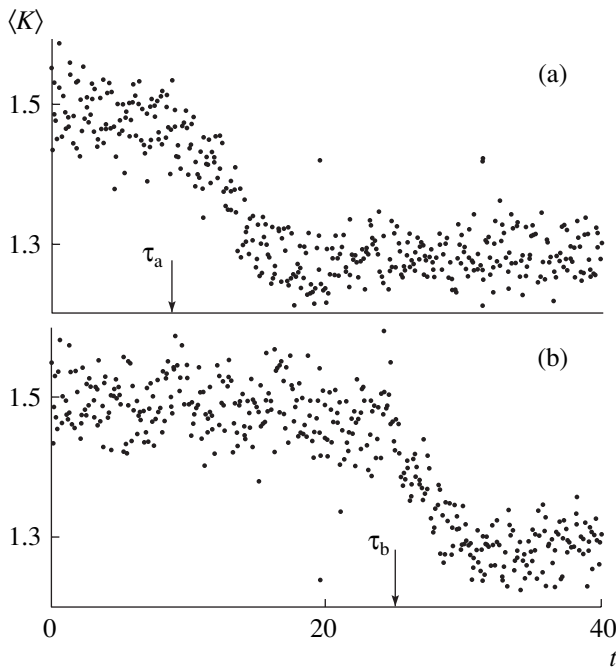*Izhorskaya ul. 13/19, Moscow, 127412 Russia*

Fig. 1. Fluctuations of the mean kinetic energy K of particles as a function of time t for two MD trajectories calculated at the same initial conditions with different integration steps h for $N = 500$ particles in a cell: (a) $h = 0.0021$; (b) 0.002. The onset and the end of the transition region correspond to the appearance of a critical nucleus and to the complete disordering (melting) of the MD system. Arrows indicate the values of lifetimes τ of the ordered metastable configuration. $n = 12$ and $X^{-1} = 1.308 \pm 0.003$.
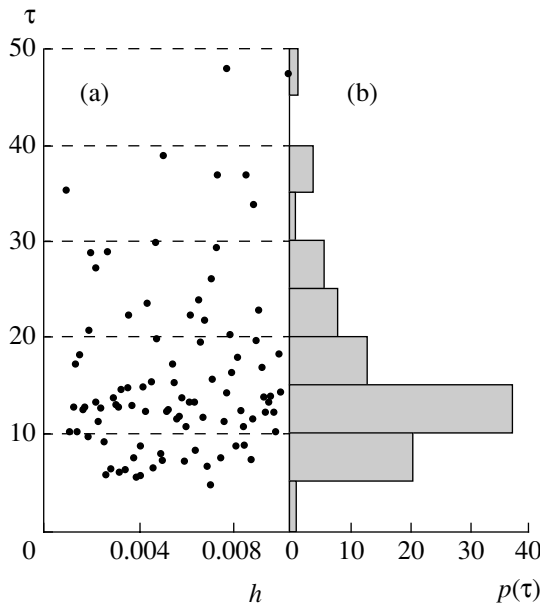

Fig. 2. (a) Lifetimes τ of a superheated metastable ordered structure for $M = 100$ various MD trajectories calculated for the same initial configuration with a different step h of numerical integration; (b) is the number of MD trajectories $p(\tau)$, for which the melting occurred within the time interval from τ to $\tau + \Delta\tau$ ($\Delta\tau = 5$); $n = 12$, $X^{-1} = 1.308 \pm 0.003$.

crystal with a given density. By this method, the system was transformed into a metastable state. The pressure P in the system was determined according to the values of E and T.

The lifetime of an ordered phase in a metastable state is finite as far as the system becomes unstable with respect to the formation of nuclei of a new disordered (liquid) phase. The probability of the formation of a critical nucleus in the system is higher the larger the degree of superheating. On the basis of the results of [6], superheating degrees were chosen for which the decomposition of the ordered crystalline structure (melting) proceeded for the times of the MD simulation (10^3–10^6 steps).

RESULTS AND THEIR ANALYSIS

The melting process was analyzed from the standpoint of both the position of particles in a cell and the dependence of the mean kinetic energy of particles (temperature) on time. For isochoric melting, the temperature of the system decreases when forming and growing a critical nucleus (Fig. 1). The onset and the end of the transition region correspond to the appearance of a critical nucleus and the moment of complete disordering of the system of particles. The calculation of the dynamics of the MD system beginning from a certain initial configuration allows us to determine the lifetime τ of the ordered metastable state.

The value of τ must be dependent only on the initial configuration of a system, since, in the case of certain initial conditions, the single solution of the Cauchy problem exists for a system of classical differential equations of motion determining the evolution of the MD model under consideration. However, while performing numerical MD calculations, it turned out that the calculations with various steps of numerical integration for the same initial configuration of the system yielded completely different values of τ. The values of τ obtained as a result of the calculations even with very close values of h can differ by several times (Fig. 1).

At the same time, the analysis of values of τ for an ensemble consisting of M trajectories of the system, which had been calculated for equal initial conditions with different h, has shown that the distribution $p(\tau)$ is independent of the interval of values of the numerical integration step h for which the trajectories were calculated (Fig. 2a). An example of the distribution $p(\tau)$ is shown in Fig. 2b. The shape of the distribution virtually does not vary for $M \geq 40$. The existence of similar distributions is evidence that even for quite definite initial conditions, the calculation can yield only probabilistic characteristics of the nonequilibrium process under consideration. The maximum of the distribution $p(\tau)$ corresponds to the most probable value of the lifetime τ^* of the ordered metastable state.

Such an independence of the result for $p(\tau)$ on the integration step with the values of τ dispersed by more than an order of magnitude for various h is associated, first of all, with the strong instability of phase trajectories. This is intrinsic to many-particle systems in which any arbitrarily small perturbation exponentially increases with time.

In connection with this, the concept of the dynamic-memory time is introduced. It can be interpreted as a time interval for which an MD trajectory calculated with the step h loses the correlation with a hypothetical exact dynamic trajectory of a system for the same initial conditions. It was shown in [10] that for a broad class of many-particle dynamical systems, the time of the dynamic memory only logarithmically increases with the accuracy of numerical integration and can be increased only twice with the employment of refined high-order numerical schemes. Therefore, the improvement of the accuracy of numerical integration does not affect the results obtained.

For the system under consideration, the time of dynamic memory is on the order of 5. The trajectories calculated with different integration steps completely lose the correlation for a time period of the same order. In the calculations performed, the nucleation processes at melting started, in the overwhelming majority of cases, at larger and larger times. Therefore, the MD trajectories calculated for the same initial conditions with a different integration step are independent, and distributions $p(\tau)$ are equivalent to those over the ensemble of initial microstates corresponding to the same degree of superheating (i.e., having the same values of the density and temperature). Along with the distribution $p(\tau)$, we can construct distributions of the number of trajectories $m(\tau)$ in which none of the critical nuclei have been formed by the time τ (Fig. 3). The distributions $p(\tau)$ and $m(\tau)$ can be obtained one from the other.

The decomposition of metastable configurations occurs as a result of the formation of nuclei. If we assume that the probability λ of the formation of a nucleus in the system is independent of time, then the nucleation can be described within the framework of the Poisson random process [2]. In this case, the probability P_0 that there are no critical nuclei in the system by the time τ exponentially decreases with time: $P_0(\tau) = \exp(-\lambda\tau)$. The obtained distributions $m(\tau)$ are well described by this formula: $\dfrac{m(\tau)}{M} \approx P_0(\tau)$ (Fig. 3). This testifies to the fact that the model of the Poisson random process is adequate to the MD system under consideration. A similar situation is characteristic of the process of homogeneous nucleation for various phase transitions. This situation was observed experimentally, e.g., the histogram presented in [2] (similar to that in Fig. 3) was obtained in the experiments on crystallization of supercooled tin drops. The shape of the histogram also
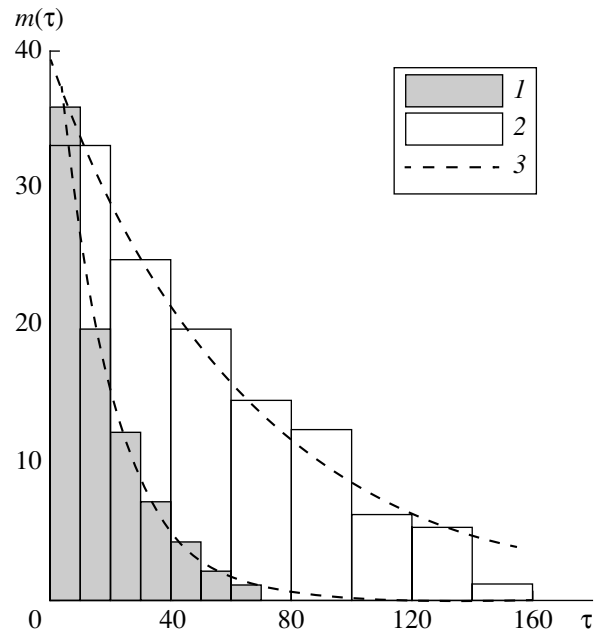
Fig. 3. Distributions $m(\tau)$ for the number of metastable ordered configurations not decomposed to the time moment τ. The configurations belong to the ensemble of M trajectories calculated with a different step of numerical integration in the case of two superheatings: (*1*) $X^{-1} = 1.3013$ ($M = 50$, $N = 500$); (*2*) $X^{-1} = 1.2993$ ($M = 40$, $N = 256$); (*3*) approximation $m(\tau) = M\exp\left(-\dfrac{\tau}{\tau^*}\right)$, according to which $\tau^* = 16.4 \pm 0.5$ for (*1*) and $\tau^* = 62 \pm 3$ for (*2*); $n = 12$.

confirms the validity of the model of the Poisson random process.

The most probable lifetime of the ordered metastable structure is $\tau^* = \lambda^{-1}$. Note that the values of λ and, consequently, also those of τ^* are determined from the distribution $m(\tau)$ (Fig. 3) more exactly than from the distribution $p(\tau)$ (Fig. 2). The distributions $m(\tau)$, which were used for the determination of the values of τ^*, had been calculated for certain values X^{-1} of superheating. However, τ^* is inversely proportional to the size of the model system: the greater the number of particles N, the larger is the number of independent centers of possible nucleation, and, consequently, the smaller τ^*. The nucleation rate $J = (\tau^* V)^{-1}$, which has the sense of the mean number of nuclei formed per unit time per unit volume, is the quantity independent of the system size. The nucleation rate is a physical parameter that characterizes the melting of a superheated crystal; this parameter can be determined from both the MD calculations and experiments. In the general case, $J = J(P, V, T)$. In the case of a system of particles whose interaction obeys a homogeneous potential, we can show that the combination $\dfrac{J}{\rho^{(8+n)/6}}$ depends only on X^{-1}; i.e., $J/\rho^{(8+n)/6} = f(X^{-1})$.
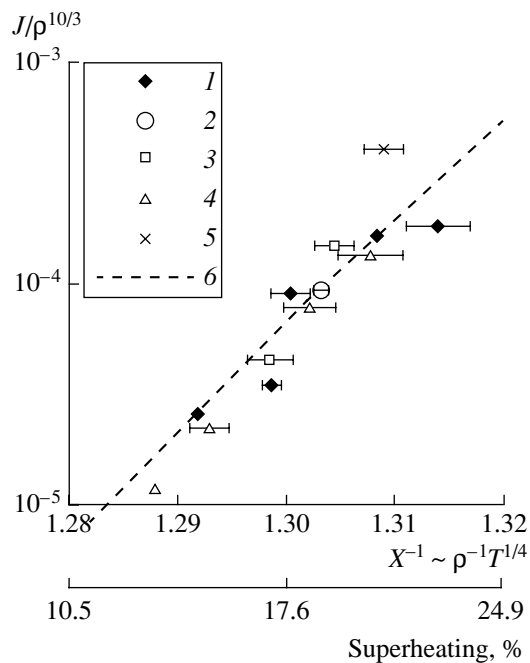
Fig. 4. Values of the combination $\dfrac{J}{\rho^{(8+n)/6}}$ calculated for

the case of an interparticle potential with $n = 12$ as a function of the parameter X^{-1} for a different number of particles in a calculation cell: (*1*) $N = 108$ ($\rho = 1.08145$); (*2*) $N = 108$ ($\rho = 1.03030$); (*3*) $N = 256$ ($\rho = 1.08145$); (*4*) $N = 500$ ($\rho = 1.08145$); and (*6*) approximation $J = J_0 \exp\left(-\dfrac{W}{k_B T}\right)$.

Such a dependence was constructed within the range of values $1.28 < X^{-1} < 1.31$ for a potential with $n = 12$ (Fig. 4). The value $X^{-1} = 1.23$ corresponds to the melting point. The temperature T (average kinetic energy) of the system prior to the melting onset was determined by averaging over MD trajectories until the moment τ. Furthermore, the temperature was averaged over various trajectories with different integration steps h. This allowed us to plot the calculation errors in Fig. 4.

The exponential increase in the observed nucleation rate with the superheating can be described by the theory of a steady-state homogeneous nucleation. According to this theory, $J = J_0 \exp\left(-\dfrac{W}{k_B T}\right)$, where W is the work spent for the formation of a critical nucleus. The approximation of the calculated points by the above dependence yields an estimate of the quantity W within the superheating range under discussion: $W = (24.5 \pm 3.3)\rho^4$. In this case, the value of J_0 is determined with a significantly higher error: $J_0 = [(5.7 \pm 2.6) \times 10^{10}]\rho^{10/3}$.

A separate issue relates to the critical nucleus size. According to visual estimates, within the superheating

range under consideration, the number of particles is on the order of 100–200, which agrees with the results of [5]. For $N = 108$, the question on the appearance of such a nucleus is meaningless. In this case, the melting mechanism likely corresponds to the cooperative decomposition process. Despite this fact, the calculation results for the nucleation rate J in the case of 108 particles well agree with those obtained in calculations with a larger number of particles.

The dashed line in Fig. 4 can be continued to the right up to a certain limiting value J_{max}. An estimate of the maximum nucleation rate J_{max} can be obtained from the following considerations: the minimum characteristic time in a system corresponds to the mean vibration period t_{min} for lattice nodes (on the order of unity, whereas the values of τ^* obtained in the calculations are equal to 10–100). The minimum characteristic volume is $v_{min} = \rho^{-1}$, thus, $J_{max} = (t_{min} v_{min})^{-1}$. The corresponding value $(X^{-1})_{max} \approx 1.37 \pm 0.02$ (superheating of 50%) determines a kinetic limit of the solid-phase stability. The error is estimated by the accuracy of the extrapolation over X^{-1} for a chosen value of J_{max}.

In the literature [11–14], the consistency of various stability criteria is now being discussed. The preliminary results of [15] show that, in our case, the thermodynamic, mechanical, and kinetic stability limits yield close values of $(X^{-1})_{max}$.

REFERENCES

1. V. G. Baĭdakov, A. E. Galashev, and V. P. Skripov, Fiz. Tverd. Tela **22**, 2681 (1980) [Sov. Phys. Solid State **22**, 1565 (1980)].

2. V. P. Skripov and V. P. Koverda, *Spontaneous Crystallization of Supercooled Liquids* (Nauka, Moscow, 1984).

3. J. Wang, J. Li, S. Yip, *et al.*, Physica A (Amsterdam) **240**, 396 (1997).

4. J. Solca, A. J. Dyson, G. Steinebrunner, *et al.*, J. Chem. Phys. **108**, 4107 (1998).

5. Z. H. Jin, P. Gumbsch, K. Lu, and E. Ma, Phys. Rev. Lett. **87**, 055703 (2001).

6. M. N. Krivoguz and G. É. Norman, Dokl. Akad. Nauk **379**, 177 (2001) [Dokl. Phys. **46**, 463 (2001)].

7. W. G. Hoover, G. Stell, E. Goldmark, and G. D. Degani, J. Chem. Phys. **63**, 5434 (1975).

8. L. D. Landau and E. M. Lifshitz, *Statistical Physics* (Nauka, Moscow, 1976, 1995; Pergamon Press, Oxford, 1980), Part 1.

9. A. A. Valuev, G. É. Norman, and V. Yu. Podlipchuk, in *Mathematical Simulation. Physicochemical Properties of Substances*, Ed. by A. A. Samarskiĭ and N. N. Kalitkin (Nauka, Moscow, 1989), pp. 5–40.

10. G. É. Norman and V. V. Stegaĭlov, Zh. Éksp. Teor. Fiz. **119**, 1011 (2001) [JETP **92**, 879 (2001)].

11. K. Lu and Y. Li, Phys. Rev. Lett. **80**, 4474 (1998).

12. V. P. Skripov and M. Z. Faĭzullin, Teplofiz. Vys. Temp. **37**, 814 (1999).

13. V. I. Zubov, N. P. Tretiakov, and J. N. Teixeira Rabelo, Mol. Mater. **13**, 349 (2000).

14. B. Rethfeld, K. Sokolowski-Tinten, D. von der Linde, and S. I. Anisimov, Phys. Rev. B **65**, 092103 (2002).

15. M. N. Krivoguz, G. É. Norman, and V. V. Stegaĭlov, Tr. Inst. Teplofiz. Ékstrem. Sostoyaniĭ, No. 4-2001 (OIVT RAN, Moscow, 2001), pp. 145–150.

Translated by T. Galkina

<hr>

TECHNICAL
PHYSICS

<hr>

A New Class of Weight Functions and Their Spectral Properties

V. F. Kravchenko* and Corresponding Member of the RAS V. I. Pustovoĭt**

Digital processing that uses weight functions (windows) is employed in practice for controlling physical effects that arise in the case of the existence of side lobes while estimating signal spectra. In this paper, starting from the concepts and results previously published in [1–4], we develop and substantiate a new method of constructing synthesized weight functions (windows). This method is based on the combination (direct product) of so-called atomic functions (AF) $\text{fup}_n(x)$ with classical Gauss functions, Bernstein–Rogozinskiĭ functions, and Dolf–Chebyshev functions. The results obtained in the course of numerical experiments prove the efficiency and reliability of the method proposed in solving problems of signal spectral analysis compared to the method of classical windows.

ATOMIC FUNCTIONS $\text{fup}_N(x)$

The finite function $\text{fup}_N(x)$ is the fractional component of the function $\text{up}(x)$ [1–4] and is determined as

$$\text{fup}_N(x) = \frac{1}{2\pi}\int_{-\infty}^{\infty} e^{jux}\left(\frac{\sin\left(\dfrac{u}{2}\right)}{\dfrac{u}{2}}\right)^N \prod_{k=1}^{\infty}\frac{\sin(u\cdot 2^{-k})}{u\cdot 2^{-k}}du. \quad (1)$$

For calculating its value, it is convenient to take a finite number of terms of an infinite product and use an expansion into a Fourier series

$$\text{fup}_{N-1}(x) = N^{-1}\left\{1 + 2\sum_{k=1}^{M}\left(\frac{\sin\left(\pi\dfrac{k}{N}\right)}{\pi\dfrac{k}{N}}\right)^N\right.$$

$$\left.\times\prod_{i=1}^{\infty}\frac{\sin\pi\dfrac{k}{2^i N}}{\pi\dfrac{k}{2^i N}}\cos\frac{2\pi kx}{N}\right\}. \quad (2)$$

* *Institute of Radio Electronics,*
  Russian Academy of Sciences,
  Mokhovaya ul. 18, Moscow, 103907 Russia
** *Research and Technology Center of Unique*
  Instrumentation, Russian Academy of Sciences,
  ul. Butlerova 15, Moscow, 117342 Russia

In this case, we have no need of calculating improper integral (1).

OPERATIONS OF THE DISCRETE FOURIER TRANSFORMATIONS AND OF THE CONVOLUTION

The Fourier transformation of a continuous signal $f(t)$ is written out as

$$F(\omega) = \int_{-\infty}^{\infty} f(t)\exp(-j\omega t)dt,$$

and its approximation within a finite interval [discrete Fourier transformation (DFT)] has the form

$$F[\omega_k] = \sum_{n=0}^{N-1} f(nT)\exp(-j\omega_k nT),$$

$$\omega_k = \frac{2\pi}{NT}k, \quad k = 0, 1, \ldots, N-1. \quad (3)$$

The product of two functions within a time region is equivalent to the convolution of their Fourier transforms written out in the frequency form

$$F[y[t_k]\cdot g[t_k]] = Y[\omega_n] * G[\omega_n]$$

or in the discrete form

$$Y[\omega_n] * G[\omega_n] = \sum_{k=0}^{N-1} Y[\omega_k]\cdot G[\omega_{n-k}].$$

This property is useful in the determination of spectra for windows being synthesized according to known Fourier transforms of initial weight functions.

NEW SYNTHESIZED WINDOWS

As is well known, in signal analysis, two problems are solved: namely, problems of detection and of estimation. The detection implies a search for an answer to the question of whether a given signal with known parameters at a given time is observed. The estimation implies the determination of parameters of a certain signal. At the same time, the spectrum of an initial signal is rarely composed of only frequency components that we are interested in and often contains overlapping

noise. To simplify solving the above problems, signals usually are decomposed into their basis components. To this aim, the expansion in terms of basis functions, i.e., simple periodic functions $\sin x$ and $\cos x$, which corresponds to the classical Fourier transformation, is used. In practice, when employing modern computers, we usually present signals as sequences of equidistant readings taken in a finite time interval. The choice of a finite interval and an orthogonal trigonometric basis results in a parasitic effect of the infiltration of spectral components (see [5, 6]). This implies that from the entire frequency continuum, only frequencies coinciding with that of the basis vector are exactly projected onto only one vector, whereas all other frequencies are projected onto all basis vectors. When using the Fourier transformation, we assume that the function under consideration is periodic and has a period equal to the observation period. At the same time, if the signal period is not multiple to the observation interval, the signal will have discontinuities at the interval ends. In order to avoid this obstacle, weight functions (windows) are applied. They make it possible to decrease the spreading of spectral components, which is caused by the finiteness of the observation interval. The basic effect of the windows manifests itself in the fact that they allow the values of a function and of its derivatives at the interval ends to be adjusted. For estimation of the weight functions (windows), the following physical characteristics are applied [6].

1. The equivalent noise band

$$k_1 = N \frac{\sum_{n=0}^{N-1} w^2(nT)}{\left[\sum_{i=0}^{N-1} w(nT)\right]^2};$$

2. The correlation of overlapping segments

$$k_2 = \frac{\sum_{n=0}^{N-1} w(nT)w\left(\left[n+\frac{N}{2}\right]T\right)}{\sum_{n=0}^{N-1} w^2(nT)} 100\%;$$

3. The parasitic amplitude modulation (AM)

$$k_3 = \frac{\left|\sum_n w(nT) \cdot \exp\left\{-i\frac{\pi}{N}n\right\}\right|}{\sum_n w(nT)};$$

4. The maximum transformation loss

$$k_4 = 10\log(k_1) + k_3;$$

5. The maximum level of side lobes

$$k_5 = 10\log\left(\max_k \left|\frac{W(\theta_k)}{W(0)}\right|^2\right),$$

where $\{\theta_k\}$ are points of local maxima (except of θ_0);

6. The bandwidth for the 6-dB level

$$k_6 = 2\theta,$$

where θ is the maximum frequency such that $10\log\left|\frac{W(0)}{W(0)}\right|^2 = 6$;

7. The coherent amplification

$$k_7 = \frac{1}{N}\sum_{n=0}^{N-1} w(nT);$$

8. The quality functional of the new weight functions for the determination of the optimal weight functions (windows) is

$$J(w) = \|w - w_{et}\|_{L^2[-1;\,1]} = \min.$$

The procedure of constructing the quality functional involves several stages. At the first stage, we determine necessary physical parameters for windows according to the above relationships *1–7*. At the second stage, we determine the value of $J(w)$ for particular weight functions. Then, the quality functional takes the following form:

$$J(w) = J(k_4(w), k_5(w), k_7(w)) = \left(\frac{k_4(w_i) - k_4(w_e)}{k_4(w_e)}\right)^2$$

$$+ \left(\frac{k_5(w_i) - k_5(w_e)}{k_5(w_e)}\right)^2 + \left(\frac{k_7(w_i) - k_7(w_e)}{k_7(w_e)}\right)^2, \quad (4)$$

where w_e is the reference window with the parameters required: $k_4 = 3$ dB, $k_5 = -100$ dB, and $k_7 = 0.5$.

Analytical expressions for the determination of the discrete-temporal Kravchenko windows are presented in Table 1. Their physical parameters are given in Table 2. The figure shows logarithmic amplitude–frequency characteristics for certain synthesized weight functions. Time and amplitude (at the left) and the frequency (radians) and amplitude logarithm (at the right) are plotted along the x and y axes, respectively. The windows given in Tables 1 and 2 are normalized to the value $w(0)$ so that their maximum value is unity. The definition region is $n \in \left[-\frac{N}{2}; \frac{N}{2}\right]$. In Table 2, characteristics of a number of known classical windows are presented:

1. Gaussian window $G_\alpha(t) = \exp\left(-\frac{(\alpha t)^2}{2}\right)$.
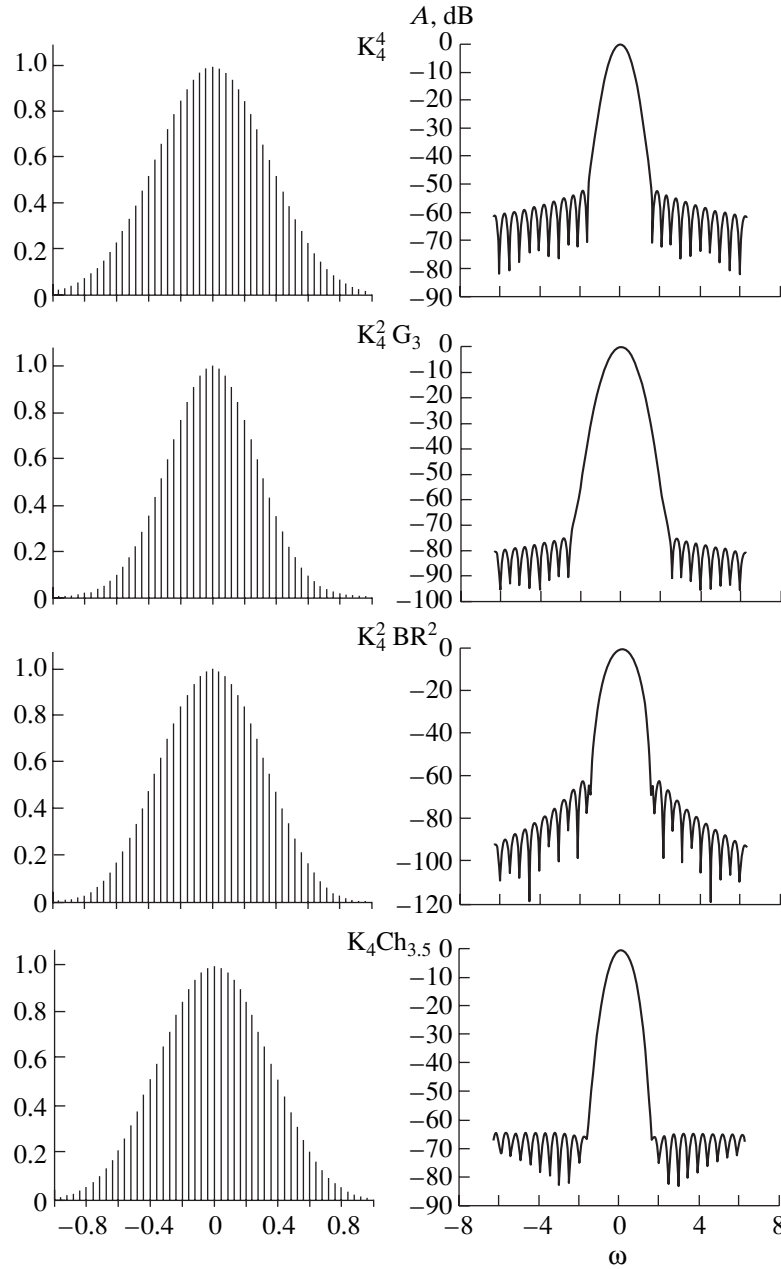
2. Bernstein–Rogozinskiĭ window $B(t) = \cos\frac{\pi t}{2}$.

Table 1. New synthesized Kravchenko windows

Window	Discrete temporal function
Kravchenko (K_2^4)	$w(n) = \mathrm{fup}_2^4\,(2n/N)$
Kravchenko–Gauss (K_2G_3)	$w(n) = \mathrm{fup}_2(2n/N) \cdot G_3(2n/N)$
Kravchenko–Bernstein–Rogozinskiĭ ($K_2^2\,BR$)	$w(n) = \mathrm{fup}_2^2\,(2n/N) \cdot B(2n/N)$
Kravchenko (K_4^4)	$w(n) = \mathrm{fup}_4^4\,(2n/N)$
Kravchenko–Gauss ($K_4^2\,G_3$)	$w(n) = \mathrm{fup}_4^2\,(2n/N) \cdot G_3(2n/N)$
Kravchenko–Bernstein–Rogozinskiĭ ($K_4^2\,BR^2$)	$w(n) = \mathrm{fup}_4^2\,(2n/N) \cdot B^2(2n/N)$
Kravchenko–Dolf–Chebyshev ($K_4Ch_{3.5}$)	$w(n) = \mathrm{fup}_4(2n/N) \cdot D_{3.5}(2n/N)$
Kravchenko–Gauss ($K_6^2\,G_3$)	$w(n) = \mathrm{fup}_6^2\,(2n/N) \cdot G_3(2n/N)$
Kravchenko–Bernstein–Rogozinskiĭ ($K_6^2\,BR^2$)	$w(n) = \mathrm{fup}_6^2\,(2n/N) \cdot B^2(2n/N)$

Table 2. Parameters of new synthesized Kravchenko windows and of classical windows

Window	Equivalent noise band, bin	Correlation of overlapped segments (50%-overlap), %	Parasitic AM, dB	Maximum transformation loss, dB	Maximum level of side lobes, dB	6.0-dB level bandwidth, bin	Coherent amplification	Quality functional
Kravchenko (K_2^4)	1.9861	4.2498	0.8518	3.8318	–51.6112	2.6276	0.3610	0.3883
Kravchenko–Gauss (K_2G_3)	1.9643	4.7297	0.8781	3.8101	–68.8390	2.6276	0.3614	0.2469
Kravchenko–Bernstein–Rogozinskiĭ ($K_2^2\,BR$)	1.7411	8.6540	1.0856	3.4939	–55.1020	2.2234	0.4166	0.2565
Kravchenko (K_4^4)	1.6295	12.2556	1.2596	3.3801	–52.1313	2.2234	0.4371	0.2610
Kravchenko–Gauss ($K_4^2\,G_3$)	2.0415	3.7429	0.8156	3.9152	–74.8054	2.6276	0.3467	0.2505
Kravchenko–Bernstein–Rogozinskiĭ ($K_4^2\,BR^2$)	1.8126	6.8755	0.9986	3.5816	–62.1117	2.4255	0.3998	0.2213
Kravchenko–Dolf–Chebyshev ($K_4Ch_{3.5}$)	1.8007	7.3910	1.0249	3.5793	–74.9523	2.4255	0.3988	0.1410
Kravchenko–Gauss ($K_6^2\,G_3$)	1.9598	4.8492	0.8844	3.8066	–70.2968	2.6276	0.3611	0.2377
Kravchenko–Bernstein–Rogozinskiĭ ($K_6^2\,BR_2$)	1.7336	8.6977	1.0859	3.4753	–51.1199	2.2234	0.4201	0.2896
Gauss, $\alpha = 3$	1.7017	10.1829	1.1632	3.4721	–56.0922	2.2234	0.4166	0.2454
Gauss, $\alpha = 3.5$	1.9765	4.6147	0.8702	3.8292	–71.0006	2.6276	0.3579	0.2413
Hamming	1.3638	23.3241	1.7492	3.0967	–45.9347	1.8191	0.5395	0.2996
Blackman–Harris (4-term)	2.0044	3.7602	0.8256	3.8453	–92.0271	2.6276	0.3587	0.1656
Nuttall (4-term)	1.9761	4.1760	0.8506	3.8087	–97.8587	2.6276	0.3636	0.1475
Dolf–Chebyshev, $\alpha = 3.5$	1.6328	11.8490	1.2344	3.3636	–70.0161	2.2234	0.4434	0.1174
Bernstein–Rogozinskiĭ	1.2337	31.8309	2.0982	3.0103	–23.0101	1.6170	0.6366	0.6674
Kaiser–Bessel, $\alpha = 3$	1.7952	7.3534	1.0226	3.5639	–69.6568	2.4255	0.4025	0.1654

Discrete windows (on the left): (K_4^4) Kravchenko; ($K_2 G_3$) Kravchenko–Gauss; ($K_4^2 BR^2$) Kravchenko–Bernstein–Rogozinskiĭ; ($K_4 Ch_3$) Kravchenko-Dolf–Chebyshev; and (on the right): corresponding logarithmic amplitude–frequency characteristics.

3. Dolf–Chebyshev window $D_\alpha(n) = F^{-1}[W_\alpha(n)]$,

$$W_\alpha(n) = (-1)^n \frac{\cos\left[N \arccos\left(\beta_\alpha \cos\left[\pi\left(\frac{n}{N} - \frac{1}{2}\right)\right]\right)\right]}{\cosh[N \cosh^{-1}(\beta_\alpha)]},$$

$$\beta_\alpha = \cosh\left[\frac{1}{N} \cosh^{-1}(10^\alpha)\right].$$

The passage from the continuous to the discrete time was performed in the following way. First, the initial window $w(x)$ was subjected to discretization over time

$w[nT] = w(t)|_{t = nT}$. Since the quantity T (discretization period) is constant, we denote the discrete window as $w[n]$. Furthermore, we applied to the obtained discrete window $w[n]$ the discrete Fourier transformation (DFT). In the case when the number of discretization points is multiple to 2^k, we used the fast Fourier transformation (FFT)

$$W(\omega) = F[w[nT]] = \sum_{n=0}^{N-1} w[n] \cdot \exp(-j\omega nT),$$

where $\omega_k = \frac{2\pi}{N}$ is the discrete frequency.

A NUMERICAL EXPERIMENT

We now analyze the most typical physical characteristics of the proposed and substantiated weight functions. As follows from Table 2, new synthesized Kravchenko windows constructed on the basis of atomic functions $\text{fup}_N(x)$ have a reasonably low level of side lobes at the acceptable width of the main lobe according to the 6-dB level. Values of the maximum transformation loss vary from 3.38 to 3.92 dB, which is a significant milestone in the analysis of signals of different physical nature. The $K_4^2 G_3$ Kravchenko–Gauss window (comparable in this case with the 4-term Blackman–Harris window) has the maximum equivalent noise band. The minimum value of the equivalent noise band is attained for the K_4^4 Kravchenko weight function, which is close to the Dolf–Chebyshev window ($\alpha = 3.5$). The quality functional $J(w)$ allows for an effect of the three most important parameters: maximum transformation loss, maximum level of side lobes, and coherent amplification. Kravchenko–Dolf–Chebyshev windows ($K_4 Ch_{3.5}$, $K_4 Ch_3$) and Kravchenko–Bernstein–Rogozinskiĭ windows ($K_4^2 BR^2$) correspond to the minimum values of $J(w)$ and therefore have a low level of side lobes, small transformation loss, and good coherent amplification.

The numerical experiment and physical analysis of its results has demonstrated that the new synthesized windows, i.e., Kravchenko, Kravchenko–Gauss, Kravchenko–Bernstein–Rogozinskiĭ, and Kravchenko–Dolf–Chebyshev windows are highly competitive by their physical parameters with classical windows and even exceed them by certain parameters. These results may be considered as basis ones while performing spectral digital processing of multidimensional signals with Doppler radars, as well as in radar stations with synthesized-aperture antenna.

REFERENCES

1. V. F. Kravchenko, Dokl. Akad. Nauk **382**, 190 (2002) [Dokl. Phys. **47**, 51 (2002)].
2. E. G. Zelkin and V. F. Kravchenko, Radiotekh. Électron. **46**, 903 (2001).
3. V. F. Kravchenko, M. A. Basarab, V. I. Pustovoĭt, and H. Peres-Meana, Dokl. Akad. Nauk **377**, 183 (2001) [Dokl. Phys. **46**, 166 (2001)].
4. V. F. Kravchenko and M. A. Basarab, Dokl. Akad. Nauk **383**, 40 (2002) [Dokl. Phys. **47**, 195 (2002)].
5. S. L. Marple, Jr., *Digital Spectral Analyses with Application* (Prentice-Hall, Eglewood Cliffts, N. J., 1987; Mir, Moscow, 1990).
6. F. J. Harris, Proc. IEEE **66** (1), 60 (1978).

Translated by G. Merzon

======= **MECHANICS** =======

Problems on the Vibration of an Elastic Half-Space Containing a System of Interior Cavities

Academician V. A. Babeshko*, A. V. Pavlova*, S. V. Ratner*, and R. T. Williams**

An elastic half-space containing a set of N flat horizontal cracks and executing steady vibrations is considered. Similar problems are of interest for engineering geology, geophysics, seismology, etc.

In this paper, the effect of certain factors such as spacings between neighboring cracks and crack-system occurrence depth on the wave-process localization is revealed.

1. We suppose that in a rectangular coordinate system (x_1, x_2, x_3), where the plane $x_1 o x_2$ is parallel to the half-space surface and the axis $o x_3$ is directed upwards, cracks are situated in planes parallel to $x_1 o x_2$ at the heights $h_1, h_2, \ldots, h_N$ $(h_1 < h_2 < \ldots < h_N)$ and occupy simply connected regions Ω_l, $l = 1, 2, \ldots, N$. These simplest irregularities among those localizing a wave process in the half-space are defined, in terms of [1–3], as an $(N + 1)$-level vibration-strength virus of class 2 and of the type S, which is denoted by $V(2/h_1; S_1/\ldots/h_N; S_N/h_{N+1}; \infty/)$. The elastic medium is characterized by the Lamé constants λ, μ and by the density ρ.

We denote the displacement amplitudes in the cross sections $x_3 \longrightarrow \pm h_l$ for a given frequency ω and the amplitudes of stresses acting on the boundaries $x_3 = h_l$ of cavities by $\mathbf{u}_l^\pm = (u_{l1}^\pm, u_{l2}^\pm, u_{l3}^\pm)$ and $\boldsymbol{\tau}_l = (\tau_{l1}, \tau_{l2}, \tau_{l3})$, respectively.

The relationship between displacements and stresses in the crack planes for an elastic layer with plane-parallel boundaries ($x_3 = h_0$ and $x_3 = h_{N+1}$) is expressed in the matrix form [3] as

$$\mathbf{L}_l^\pm \mathbf{U}_l^\pm - \mathbf{L}_{l+1}^\pm \mathbf{U}_{l+1}^\pm = \mathbf{D}_l^\pm \mathbf{T}_l - \mathbf{D}_{l+1}^\pm \mathbf{T}_{l+1}. \qquad (1)$$

Here, the following notation is introduced: $\mathbf{U}_l^\pm = \{U_{l,m}^\pm\}$, $\mathbf{T}_l = \{T_{l,m}\}$, $m = 1, 2, 3$, $l = 0, 1, \ldots, N$. Taking

---

* *Kuban State University,*
ul. Karla Libknekhta 9, Krasnodar, 350640 Russia
** *Tennessee University, USA*

into account the character of the irregularities under consideration, we assume hereinafter that $\mathbf{T}_l = \mathbf{T}_l^+ = \mathbf{T}_l^-$,

$$U_{l,m}^\pm(\alpha_1, \alpha_2) = V u_m^\pm(x_1, x_2, h_l),$$
$$T_{l,m}(\alpha_1, \alpha_2) = V \tau_m(x_1, x_2, h_l),$$

where V is the two-dimensional Fourier transform operator;

$$\mathbf{L}_l^\pm$$

$$= \begin{pmatrix} \pm \alpha_1 \alpha_{31} e^{\pm i\alpha_{31}h_l} & \pm \alpha_2 \alpha_{31} e^{\pm i\alpha_{31}h_l} & s e^{\pm i\alpha_{31}h_l} \\ \pm \alpha_2 \alpha_{32} e^{\pm i\alpha_{32}h_l} & \mp \alpha_1 \alpha_{32} e^{\pm i\alpha_{32}h_l} & 0 \\ (2s + \alpha_2^2) e^{\pm i\alpha_{32}h_l} & -\alpha_1 \alpha_2 e^{\pm i\alpha_{32}h_l} & \mp 2\alpha_1 \alpha_{32} e^{\pm i\alpha_{32}h_l} \end{pmatrix},$$

$$\mathbf{D}_l^\pm = \frac{i}{\mu} \begin{pmatrix} \dfrac{\alpha_1}{2} e^{\pm i\alpha_{31}h_l} & \dfrac{\alpha_2}{2} e^{\pm i\alpha_{31}h_l} & \dfrac{\pm \alpha_{31}}{2} e^{\pm i\alpha_{31}h_l} \\ \alpha_2 e^{\pm i\alpha_{32}h_l} & -\alpha_1 e^{\pm i\alpha_{32}h_l} & 0 \\ \pm \alpha_{32} e^{\pm i\alpha_{32}h_l} & 0 & -\alpha_1 e^{\pm i\alpha_{32}h_l} \end{pmatrix}.$$

Here, the following denotations are used:

$$\alpha^2 = \alpha_1^2 + \alpha_2^2, \quad s = 0.5\gamma_2^2 - \alpha^2,$$

$$\alpha_{31} = \pm\sqrt{\gamma_1^2 - \alpha^2}, \quad \alpha_{32} = \pm\sqrt{\gamma_2^2 - \alpha^2},$$

$$\gamma_1 = \frac{\omega}{v_1}, \quad \gamma_2 = \frac{\omega}{v_2}, \quad v_1 = \sqrt{\frac{\lambda + 2\mu}{\rho}}, \quad v_2 = \sqrt{\frac{\mu}{\rho}}.$$

The system of operator equations (1) is equivalent to a system of integral equations of the first kind.

Within the framework of the developed approach, it is easy to turn to the consideration of an elastic half-space with an array of cracks. For constructing a matrix representation of the system of integral equations in the case of half-space $x_3 \le h_{N+1}$, it is sufficient to formally
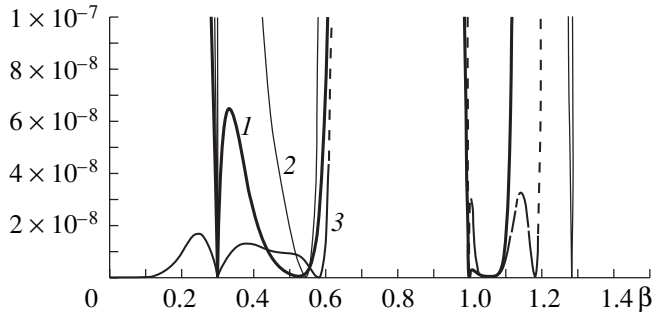
Fig. 1. Function of the determinant modulus for $\mathbf{A}_N$ at $N = 2$, $\varepsilon = 0.3$: (*1*) $\gamma_2 h_{12} = \gamma_2 h_{23} = \frac{\pi}{3}$, (*2*) $\frac{2\pi}{3}$; (*3*) π. $\beta \in [0; 1.5]$.
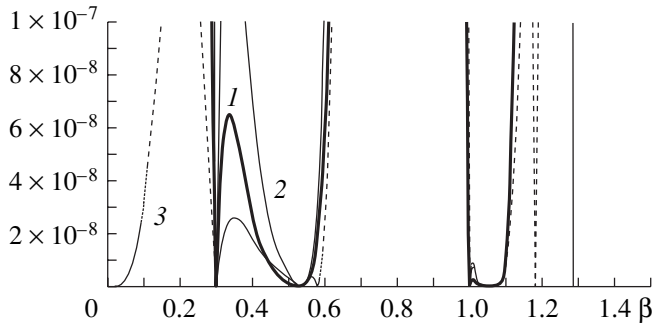

Fig. 2. Function of the determinant modulus for $\mathbf{A}_N$ at $N = 2$, $\varepsilon = 0.3$, $\gamma_2 h_{12} = \frac{\pi}{3}$, $\gamma_2 h_{23} = $ (*1*) $\frac{\pi}{3}$; (*2*) $\frac{2\pi}{3}$; (*3*) π. $\beta \in [0; 1.5]$.

exclude the terms with $e^{\pm i\alpha_{3k}h_0}$, $k = 1, 2$ and $e^{i\alpha_{3k}h_1}$ in relationships (1) for $l = 0$:

$$\mathbf{L}_1^- \mathbf{U}_1^- = \mathbf{D}_1^- \mathbf{T}_1,$$

$$\mathbf{L}_1^- \mathbf{U}_1^+ - \mathbf{L}_2^- \mathbf{U}_2^- = \mathbf{D}_1^- \mathbf{T}_1 - \mathbf{D}_2^- \mathbf{T}_2,$$

$$\mathbf{L}_1^+ \mathbf{U}_1^+ - \mathbf{L}_2^+ \mathbf{U}_2^- = \mathbf{D}_1^+ \mathbf{T}_1 - \mathbf{D}_2^+ \mathbf{T}_2,$$

$$\dots \tag{2}$$

$$\mathbf{L}_N^- \mathbf{U}_N^+ - \mathbf{L}_{N+1}^- \mathbf{U}_{N+1}^- = \mathbf{D}_N^- \mathbf{T}_N - \mathbf{D}_{N+1}^- \mathbf{T}_{N+1},$$

$$\mathbf{L}_N^+ \mathbf{U}_N^+ - \mathbf{L}_{N+1}^+ \mathbf{U}_{N+1}^- = \mathbf{D}_N^+ \mathbf{T}_N - \mathbf{D}_{N+1}^+ \mathbf{T}_{N+1}.$$

The system obtained can be rewritten in the form resolved in terms of $\mathbf{T}_l$, $l = 1, 2, \dots, N + 1$. Using the denotation $\mathbf{U}_l = \mathbf{U}_l^+ - \mathbf{U}_l^-$, we obtain the matrix form of the system

$$\mathbf{S}_N \mathbf{U} = \mathbf{T}, \tag{3}$$

where

$$\mathbf{T} = \{\mathbf{T}_1, \mathbf{T}_2, \dots, \mathbf{T}_N, \mathbf{T}_{N+1}\},$$

$$\mathbf{U} = \{\mathbf{U}_1, \mathbf{U}_2, \dots, \mathbf{U}_N, \mathbf{U}_{N+1}^-\};$$

$$\mathbf{S}_N = \mathbf{G}_N^{-1} \mathbf{A}_N,$$

$$\mathbf{G}_N = \begin{pmatrix} \mathbf{M} & 0 & \dots & 0 & -(\mathbf{L}_1^+)^{-1}\mathbf{D}_{N+1}^+ \\ 0 & \mathbf{M} & \dots & 0 & -(\mathbf{L}_2^+)^{-1}\mathbf{D}_{N+1}^+ \\ \dots & \dots & \dots & \dots & \dots \\ 0 & 0 & \dots & \mathbf{M} & -(\mathbf{L}_N^+)^{-1}\mathbf{D}_{N+1}^+ \\ 0 & 0 & \dots & 0 & -(\mathbf{L}_{N+1}^-)^{-1}\mathbf{D}_{N+1}^- \end{pmatrix},$$

$$\mathbf{A}_N = \begin{pmatrix} \mathbf{I} & \mathbf{A}_{12}^+ & \dots & \mathbf{A}_{1N}^+ & -\mathbf{A}_{1N+1}^+ \\ \mathbf{A}_{12}^- & \mathbf{I} & \dots & \mathbf{A}_{2N}^+ & -\mathbf{A}_{2N+1}^+ \\ \dots & \dots & \dots & \dots & \dots \\ \mathbf{A}_{1N}^- & \mathbf{A}_{2N}^- & \dots & \mathbf{I} & -\mathbf{A}_{NN+1}^+ \\ \mathbf{A}_{1N+1}^- & \mathbf{A}_{2N+1}^- & \dots & \mathbf{A}_{NN+1}^- & -\mathbf{I} \end{pmatrix}.$$

Here, $\mathbf{A}_{mk}^+ = (\mathbf{L}_m^+)^{-1}\mathbf{L}_k^+$, $\mathbf{A}_{mk}^- = (\mathbf{L}_k^-)^{-1}\mathbf{L}_m^-$, $m < k$, $\mathbf{M} = (\mathbf{L}_l^+)^{-1}\mathbf{D}_l^+ - (\mathbf{L}_l^-)^{-1}\mathbf{D}_l^-$, $k, l, m = 1, 2, \dots, N$.

It is evident that $|\mathbf{S}_N| = |\mathbf{L}_{N+1}^-| |\mathbf{D}_{N+1}^-|^{-1} |\mathbf{M}|^{-N} |\mathbf{A}_N|$. Then, we can write out

$$|\mathbf{S}_N| = \frac{2i\mu^3 \alpha_{32}(\alpha^2 \alpha_{31}\alpha_{32} + s^2)}{(\alpha^2 + \alpha_{31}\alpha_{32})} |\mathbf{M}|^{-N} |\mathbf{A}_N|. \tag{4}$$

2. Methods for calculating the determinant of the matrix $\mathbf{A}_N$ are analyzed in [4]. Thus, the study of the properties of the matrix determinant of system (3) for the half-space with a set of N flat horizontal cracks is formally reduced to the previously considered case for an elastic half-space with $N + 1$ cracks. Extra factor (4) contains the known Rayleigh function and has the real-valued zero ξ_R. By virtue of the complexity of function (4), analytically investigating the distribution of its zeros seems to be impossible.

The results of the numerical investigation of the matrix determinant $\mathbf{A}_N$ are shown in the graphic representation in Figs. 1 and 2. From the analysis of these results, the following conclusions can be drawn: The number of real zeros increases with vertical distance between neighboring cracks. The change in the distance between cracks, which is a multiple of the half-length of the transverse wave in the medium, gives rise to an additional real-valued zero. The crack-system deepening affects the number of real-valued zeros of the determinant in a similar manner. In addition, the determinant of the system matrix $\mathbf{S}_N$ has the zero ξ_R and two branch points as real-valued singularities. Upon passing to dimensionless coordinates, the branch points will be $\beta = \varepsilon, 1$, where $\beta = \frac{\alpha}{\gamma_2}$, $\varepsilon = \frac{\gamma_1}{\gamma_2}$.

Figure 1 shows the modulus of the determinant $\mathbf{A}_N$ for $N = 2$, $\varepsilon = 0.3$ in the cases of $\gamma_2 h_{12} = \gamma_2 h_{23} = \dfrac{\pi}{3}$ (curve *1*), $\gamma_2 h_{12} = \gamma_2 h_{23} = \dfrac{2\pi}{3}$ (curve *2*), and $\gamma_2 h_{12} = \gamma_2 h_{23} = \pi$ (curve *3*). Figure 2 corresponds to $N = 2$, $\varepsilon = 0.3$, $\gamma_2 h_{12} = \dfrac{\pi}{3}$ in the cases of $\gamma_2 h_{23} = \dfrac{\pi}{3}$ (curve *1*), $\gamma_2 h_{23} = \dfrac{2\pi}{3}$ (curve *2*), and $\gamma_2 h_{23} = \pi$ (curve *3*).

ACKNOWLEDGMENTS

REFERENCES

1. V. A. Babeshko, Izv. Vyssh. Uchebn. Zaved., Sev.-Kavk. Reg., Estestv. Nauki, No. 3, 5 (2000).

2. V. A. Babeshko, Dokl. Akad. Nauk **373**, 191 (2000) [Dokl. Phys. **45**, 342 (2000)].

3. V. A. Babeshko, Izv. Akad. Nauk, Mekh. Tverd. Tela, No. 3, 5 (2000).

4. V. A. Babeshko, A. V. Pavlova, and S. V. Ratner, Izv. Vyssh. Uchebn. Zaved., Sev.-Kavk. Reg., Estestv. Nauki, Spetsvypusk: Matematicheskoe modelirovanie, 26 (2001).

Translated by V. Tsarev

Nonlocal Fracture Criterion: Finite Strains

V. A. Levin* and E. M. Morozov**

Theory of multiple overlap of severe strains [1] allows us to analyze crack growth for finite strains of a body made of viscous elastic material on the basis of subsequently merging micropores and secondary cracks with the main crack. To do this, a criterion for the breakage of a wall between the main crack and a secondary crack or a micropore merging with the main crack is necessary, as well as a criterion for the formation (opening) of micropores in the course of the deformation process. We should note that for finite strains, the models of the viscous growth of cracks in bodies made of a viscous elastic material have not been considered previously.

One of the versions of such criteria, namely, "averaging" criteria is proposed in this paper. Generally speaking, fracture criteria in the form of averaging the criterion quantity both over space and over time (but not for finite strains and for bodies made of a viscous elastic material) are well known [2–4]. However, the versions proposed here do not coincide with them.

In our opinion, in viscous elastic bodies (especially for finite strains), we should take into account the history of the body deformation preceding the moment of the intercrack-wall breakage or the micropore opening within the time interval $0 \leq t \leq T$. We propose the following criterion

$$\int_0^T K d\tau \leq K_{01} T. \qquad (1)$$

Here, $K = K(\sigma_i)$ is the given function of σ_i if the force criterion is employed (the use of the deformation criterion also is possible); $\sigma_i(x_j, t)$, $i = 1, 2, 3, j = 1, 2, 3$, are the principal values of the true-stress tensor (Cauchy tensor); x_j are the spatial coordinates; t is time; K_{01} is an experimentally chosen (determined) material parameter; and T is the time at which the strength analysis is performed.

Criterion (1) can be used either for the determination of the moment T, at which, according to this criterion, the onset of the intercrack-wall breakage (or the micropore opening) occurs, or simply in the form of a separate criterion of the intercrack-wall breakage (or micropore opening).

We here repeat that, according to criterion (1), the intercrack-wall breakage occurs while attaining a limiting value of an averaged criterion quantity for a certain finite time interval T, which we are interested in and which is assigned by us (and involves the entire history of loading). Among all the time moments $t \leq T$ being analyzed, the equality in condition (1) is valid only at the moment of the intercrack-wall breakage or opening (formation) of a micropore at $t = T$.

Assuming $K(\sigma_i) = \sigma_1$, we write out criterion (1) in the form

$$\int_0^T \sigma_1 d\tau < \sigma_{01} T, \qquad (2)$$

where σ_{01} is an experimentally chosen (determined) material parameter.

In addition, in our opinion, in viscous elastic bodies (especially for finite deformations), the micropore opening (formation) occurs not when the ultimate strength is exceeded at a certain point but when the total (integrated) level of the ultimate strength is exceeded over the entire length (diameter) of a micropore. It occurs when in the center of this (future) micropore, the ultimate strength reaches its maximum, which determines the position of this center. Therefore, criterion (2), as the criterion of the micropore opening in the loaded body (for the plane problem), is supposed to be generalized and used in the following form:

$$\int_{-1/2b}^{1/2b} dx \int_0^T \sigma_1 d\tau < \sigma_{02} T D. \qquad (3)$$

Here, D is the micropore length and σ_{02} is an experimentally chosen (determined) material parameter.

While solving concrete problems of such a type, we should probably choose the center of a future micropore at the point corresponding to the distance of

* *Moscow State University,*
 Leninskie Gory, Moscow, 119899 Russia
** *Moscow Engineering Physics Institute,*
 Kashirskoe sh. 31, Moscow, 115409 Russia

more than $0.5D$ from the tip of the main crack, where σ_1 reaches its largest value.

Employment of criterion (2) as a criterion of the breakage of a wall between the main crack and the secondary crack or the micropore (the plane geometry) allows us to write out this criterion in the following form:

$$\int_A^B dx \int_0^T \sigma_1 d\tau \le \sigma_{03} Tb. \qquad (4)$$

Here, $AB = b$ is a distance between the main crack and a secondary crack or micropore; x is the axis perpendicular to the first principal direction of the true-stress tensor (in the deformation plane); and σ_{03} is an experimentally chosen (determined) material parameter.

Note that criteria (3) and (4) have different scale levels so that usually $b \gg D$.

Criteria (3) and (4) with account of criterion (1) have the following form:

$$\int_{-1/2b}^{1/2b} dx \int_0^T K d\tau \le K_{02} TD, \qquad (5)$$

$$\int_A^B dx \int_0^T K d\tau \le K_{03} Tb. \qquad (6)$$

Finally, we note that in the general case, criterion (5), which is the criterion of the micropore opening, can be written as

$$\int_0^{V_c} dV \int_0^T K d\tau \le K_{02} TV_c, \qquad (7)$$

where, as before, $K = K(\sigma_i)$, K_{02} is an experimentally chosen (determined) parameter, and V_c is the mean micropore volume.

Thus, the opening (formation) of a micropore occurs when the "total" (integrated) level of the ultimate strength is exceeded over the entire volume V_c of a micropore and, in the center of this (future) micropore, the ultimate strength reaches its maximum (which determines the choice of the position of this center in particular calculations).

The physical meaning of the averaging criteria proposed by us can be speculatively substantiated by the fact that a body cannot be fractured by a mechanical field (external action) at a single point, since the neighboring points inevitably should be involved in the fracture process. This involvement is extended in both time and space by virtue of the nonuniformity of action of the mechanical field (also owing to the viscous elastic processes among those occurring in the body's material).

It is worth noting that the averaging over the space was realized in the fracture mechanics by introducing an averaged coefficient of the stress intensity at a certain segment along the crack front [5]. As was indicated in [5], an attempt to average the stress-intensity coefficient even along the entire length of the contour of the surface semi-elliptical crack in a mechanical part being calculated satisfactorily agrees with experimental data.

REFERENCES

1. V. A. Levin, *Multiple Overlap of Severe Deformations in Elastic and Viscoelastic Bodies* (Fizmatlit, Moscow, 1999).

2. G. Neĭber, *Concentration of Stresses* (Gostekhizdat, Moscow, 1947).

3. V. V. Novozhilov, Prikl. Mat. Mekh. **33**, 212 (1969).

4. N. F. Morozov and Yu. V. Petrov, Dokl. Akad. Nauk SSSR **324**, 964 (1992) [Sov. Phys. Dokl. **37**, 285 (1992)].

5. E. M. Morozov and P. V. Kostenko, Zavod. Lab., No. 7, 31 (1999).

Translated by T. Galkina

===== **MECHANICS** =====

Pressure Waves in a Stratified Medium Involving a Liquid and a Liquid with Gas Bubbles

Academician V. E. Nakoryakov and V. E. Dontsov

Received May 13, 2002

The propagation of pressure waves in a liquid with gas bubbles has been adequately investigated over the last 30 years both theoretically and experimentally [1–5]. In particular, a nonlinear finite-duration perturbation in a liquid with gas bubbles was shown to decompose into solitary waves (solitons), whose evolution and structure were studied in detail. The heat exchange between a gas in bubbles and an ambient liquid was shown to be the basic mechanism of wave dissipation in bubble media over a wide range of their parameters. In [6, 7], the structure and attenuation of solitary pressure waves with moderate amplitude were investigated experimentally in a liquid with gas bubbles uniform in size. Allowance for the polydispersity of a gas–liquid medium leads to additional attenuation of pressure waves [8, 9]. New types of wave structures, multisolitons in a liquid with gas bubbles of two different sizes, were discovered in [10] for various ratios between the bubble radii. The effect of the inhomogeneity of a gas–liquid mixture and the compressibility of a liquid on the structure of a pressure wave was investigated in [11, 12]. The structure of upward and downward bubble flows was studied in [13, 14]. The gas phase is substantially redistributed over the pipe cross section even for low volume gas contents. Bubbles are almost entirely concentrated either in the central region of the pipe (downward flow) or in the near-wall region (upward flow).

In this study, we experimentally investigated the evolution and attenuation of moderate-amplitude pressure waves in a liquid containing gas bubbles inhomogeneously (stepwise) distributed over a section transverse to the wave-propagation direction.

The experiments were carried out in a shock tube. Its active region is a 1.5-m-long vertical thick-walled steel pipe with an inner diameter of 53 mm. A thin-walled (30-μm-thick) Dacron pipe 37.5 mm in diameter was arranged inside the active region. The Dacron pipe was rigidly mounted by thin partitions to the active region. This region was filled with a liquid and saturated with gas bubbles by a generator arranged in the

Institute of Thermophysics, Siberian Division,
Russian Academy of Sciences,
pr. Akademika Lavrent'eva 1, Novosibirsk, 630090 Russia

lower part of the pipe. The experiments were carried out for three structures of the bubble medium. Bubbles were supplied uniformly either over the cross section of the entire active region, over the ring between the Dacron pipe and the active-region wall (gas–liquid ring), or inside the Dacron pipe (gas–liquid column). The spread of gas-bubble sizes was equal to ±5%. The mean bubble radius was equal to 0.53 mm. As a working liquid, we used the 50% (in mass) solution of glycerin in distilled water. Freon 12 and nitrogen having different thermal diffusivities were used as a gas phase. A volume gas–bubble fraction average over both cross section and active-region length was determined from the liquid-level increase in the active region upon introducing gas bubbles and was equal to 0.5% for all of the experiments. The experiments were carried out at room temperature and atmosphere static pressure P_0 over the level of the gas–liquid medium.

Bell-shaped pressure waves were generated by an electromagnetic radiator arranged at the active-region bottom. A signal is formed when a thin copper plate is repulsed from the coil through which a current pulse flows. The pressure-wave profiles were detected by six piezoelectric pressure sensors arranged along the active region. The sensor signals were applied to an analog-to-digital converter and processed by a computer.

The experimental results showed that the inhomogeneous distribution of the gas phase over the pipe cross section substantially affects the evolution and attenuation of waves in bubble media. Figure 1 shows the time dependence of pressure-wave profiles at various distances X from the entrance of the wave into a liquid with bubbles of a gas (Freon) with low heat conductivity for various structures of the medium and almost identical amplitudes ΔP_0 of the initial signal (ΔP is the wave amplitude or the first-oscillation amplitude for a group of solitary waves and oscillating shock waves). Comparison between the evolutions of waves in Figs. 1a and 1b demonstrates that the displacement of gas bubbles from the central part of the pipe to the near-wall region with conservation of the volume gas-content average over the cross section considerably increases the attenuation rate and qualitatively changes the wave structure. Whereas solitary waves (solitons) were isolated from the initial signal even at distance
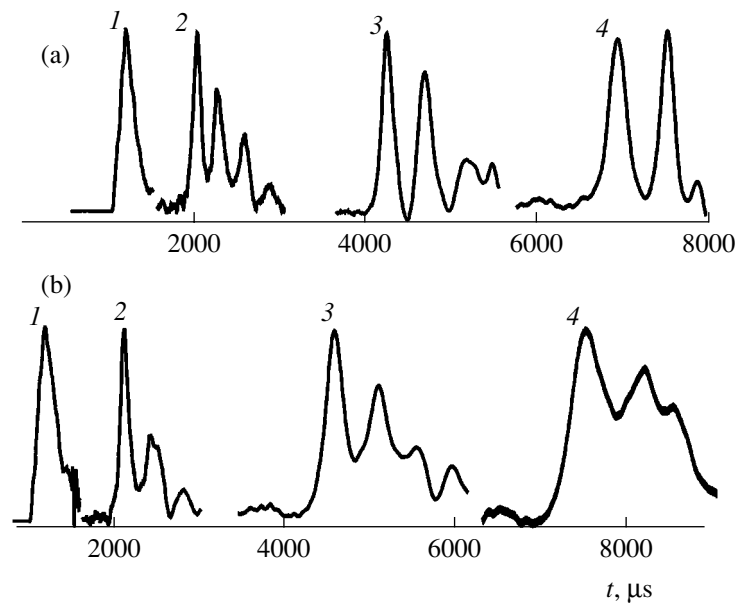
Fig. 1. Profiles of the pressure wave in a liquid with Freon bubbles for X = (*1*) 0, (*2*) 0.25, (*3*) 0.76, and (*4*) 1.25 m and for (a) homogeneous medium where ΔP_0 = (*1*) 0.272 MPa, ΔP = (*2*) 0.172, (*3*) 0.117, and (*4*) 0.068 MPa and (b) gas–liquid ring near the wall, where ΔP_0 = (*1*) 0.219 MPa, ΔP = (*2*) 0.195, (*3*) 0.072, (*4*) 0.031 MPa.

$X = 0.76$ m (Fig. 1a, curve *3*) for the homogeneous distribution of bubbles over the pipe cross section, an oscillating shock wave was formed near the pipe wall in the gas–liquid ring (Fig. 1b, curve *3*). The oscillating shock wave is formed due to increasing dissipative losses in the medium. It should be noted that the gas-phase redistribution over the pipe cross section does not change the frequency of oscillations in the wave. The duration of the first oscillation corresponds to the resonance oscillations of gas bubbles in the wave as for the medium with homogeneously distributed bubbles.

When, instead of low heat-conducting Freon bubbles, homogeneously distributed nitrogen bubbles that have higher heat conductivity and the same size and volume gas content are used, waves with close initial amplitudes are attenuated faster. This increase takes place because the basic mechanism of wave dissipation in a homogeneous bubble medium is thermal dissipation [3, 6].

When the wave amplitude increases, its attenuation rate also increases. Due to this fact, oscillating shock waves are formed from the initial signal for every structure of the gas–liquid medium.

We obtained experimental data on the velocity of low-amplitude pressure waves in the medium with various distributions of gas bubbles. The speed of sound in the gas–liquid medium was shown to be independent of the degree of homogeneity of the gas-bubble distribution over the pipe cross section and to be determined by the volume gas content average over the cross section.

The experiments showed that a solitary wave is formed from the initial signal due to dispersion and nonlinear effects in the gas–liquid ring near the wall or

in the gas–liquid column in the pipe center faster than in the case of the homogeneous distribution of bubbles in the liquid.

Figure 2 shows the attenuation rate of a pressure wave (first oscillation) in a liquid with gas bubbles as a
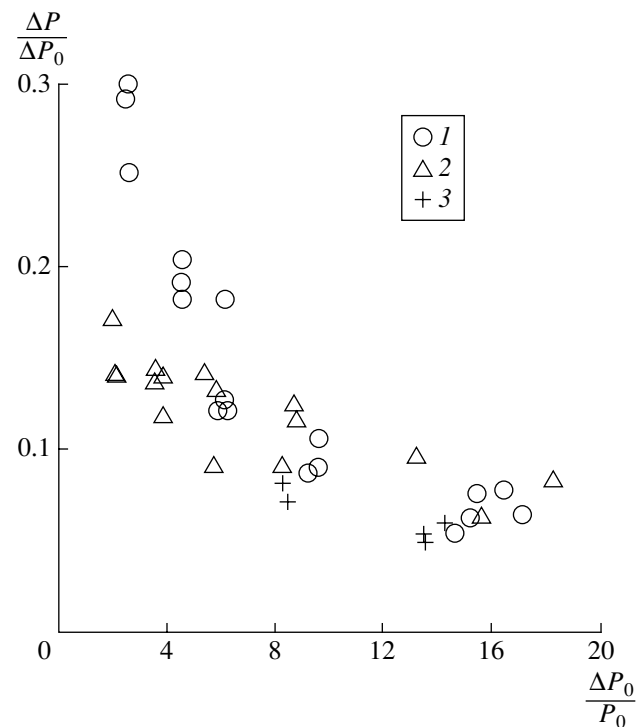

Fig. 2. Attenuation rate of the pressure wave in a liquid with Freon bubbles as a function of its amplitude: (*1*) homogeneous medium, (*2*) gas–liquid ring near the wall, and (*3*) gas–liquid column at the pipe center.

function of wave amplitude at distance $X = 1.25$ m from the entrance of the wave into the medium. It is seen that the attenuation rate is independent of the bubble distribution over the pipe cross section for high wave amplitudes. As the wave amplitude decreases, points *1* and *2* in Fig. 2 are separated from each other. Therefore, the inhomogeneity of the gas-phase distribution for Freon bubbles in the liquid leads to additional attenuation comparable with thermal dissipation. For the liquid with nitrogen bubbles, attenuation rates for various structures of the medium differ from each other much weaker because thermal dissipation prevails for nitrogen bubbles. Additional dissipation due to the inhomogeneity of the bubble medium over the section perpendicular to the wave-propagation direction can be caused by the relative motion of gas bubbles in the liquid. The effect of the relative motion of bubbles in a liquid for homogeneous bubble media was first considered in [15]. However, as was shown later in [3, 4], thermal dissipation in homogeneous bubble media usually dominates over viscous dissipation due to the relative motion of bubbles. For bubble media substantially inhomogeneous over the cross section, the relative motion of bubbles in a wave occurs not only along the wave propagation, but also in the transverse direction towards a higher compressibility of the medium. This motion increases the magnitude and changes the direction of the relative velocity of bubbles as compared to a homogeneous medium and, correspondingly, increases the attenuation rate. In addition, vortex structures can be formed when the liquid moves in the pressure wave due to the transverse component of the velocity of the liquid and to the solid wall of the active region. The presence of vortex structures also gives rise to additional attenuation of the pressure wave.

Thus, we showed that the distribution of gas bubbles over the section transverse to the direction of wave propagation can increase its attenuation. An attenuation mechanism associated with the relative motion of gas bubbles in a liquid and with the formation of vortex structures in the wave was proposed.

REFERENCES

1. G. K. Batchelor, Mechanik **109**, 67 (1968).
2. L. Van Wijngaarden, J. Fluid Mech. **33**, 465 (1968).
3. V. E. Nakoryakov, B. G. Pokusaev, and I. R. Schreĭber, *Wave Dynamics of Gas– and Vapor–Liquid Media* (Énergoatomizdat, Moscow, 1990; Begell House, New York, 1992).
4. R. I. Nigmatulin, *Dynamics of Multiphase Media* (Nauka, Moscow, 1987), Vols. 1, 2.
5. M. Watanabe and A. Prosperetti, J. Fluid Mech. **274**, 349 (1994).
6. V. E. Dontsov, V. E. Kuznetsov, P. G. Markov, and V. E. Nakoryakov, Akust. Zh. **33**, 1041 (1987) [Acoust. Phys. **33**, 605 (1987)].
7. V. E. Nakoryakov, V. E. Kuznetsov, V. E. Dontsov, and P. G. Markov, Int. J. Multiphase Flow **16**, 741 (1990).
8. V. K. Kedrinskiĭ, PMTF, Zh. Prikl. Mekh. Tekh. Fiz., No. 4, 29 (1968).
9. V. Sh. Shagapov, Izv. Akad. Nauk SSSR, Mekh. Zhidk. Gaza, No. 6, 145 (1976).
10. V. E. Nakoryakov and V. E. Dontsov, Dokl. Akad. Nauk **378**, 483 (2001) [Dokl. Phys. **46**, 422 (2001)].
11. A. E. Beylich and A. Gulhan, Phys. Fluids A **2**, 1412 (1990).
12. M. Kameda, N. Shimaura, F. Higashino, and Y. Matsumoto, Phys. Fluids **10**, 2661 (1998).
13. O. N. Kashinsky and V. V. Randin, Int. J. Multiphase Flow **25**, 109 (1999).
14. O. N. Kashinsky and L. S. Timkin, Exp. Fluids **26** (2), 305 (1999).
15. L. Noordzij and L. Van Wijngaarden, J. Fluid Mech. **66**, 115 (1974).

Translated by V. Bukhanov

===== **MECHANICS** =====

Generalization of the Leveque Problem for Mass Transfer in Swirling Flows in the Entrance Region of a Cylindrical Section

V. L. Okulov[1,*], S. Martemianov[2], and T. O. Murakhtina[1]
Presented by Academician A.K. Rebrov December 20, 2001

The swirl of a flow has long been used to increase mass transfer. Numerous experimental data obtained in this field are still processed and compared with each other only by using empirical formulas [1–4]. In particular, the Sherwood number Sh is conventionally represented in terms of the rate-averaged Reynolds number Re as [2]

$$\text{Sh} = c\text{Re}^n\text{Sc}^{1/3}, \quad \text{Re} = \frac{Ud}{\nu}. \qquad (1)$$

Here, Sc is the Schmidt number; ν is the kinematic viscosity of a fluid; d is the hydraulic diameter; $U = \dfrac{Q}{\Sigma}$ is the rate-averaged velocity of a flow, where Q is the volume rate and Σ is the cross-section area $\left(\Sigma = \pi R^2 \text{ for a tube of radius } R = \dfrac{d}{2}\right)$; and c and n are the empirical parameters. However, in contrast to axial non-swirling flows, the comparison [4] of experimental data [1–4] for various set-ups and flow regimes did not reveal the generalized character of Eq. (1) for swirling flows.

To verify the applicability of Eq. (1) to mass transfer in swirling flows, we consider the problem of mass transfer from a swirling flow to a microelectrode flash mounted with the wall of a cylindrical tube of radius R (corresponding measurements were reported, e.g., in [4]). In order to simplify the mathematical formulation of the problem, we examine only axisymmetrically developed flow regimes (turbulent pulsations and three-dimensional effects are ignored). Let the distance z_0 from the entrance of the cylindrical section to the microelectrode be so small that the boundary layer developed in this length is thin (its thickness $\delta \ll R$) and

only slightly affects the inviscid flow in the stream core. We assume that mass transfer does not affect the hydrodynamics of the stream (the Schmidt number is assumed to be constant and we do not discuss the dependence of processes on it; let it be sufficiently large and the diffusion layer be deep inside the boundary layer). To describe the swirl motion of an electrolyte in the tube, we consider the flow induced by the axisymmetric vortex structure determining the inviscid stream core. Let the vortex axis coincide with the cylinder axis and the vortex core be of radius $\varepsilon < R$ and consist of vortex helixes, which have constant pitch $2\pi l$ and constant axial vorticity component corresponding to the simple velocity field [5]

$$w_\varphi = \frac{\Gamma}{r}\begin{cases} \dfrac{r^2}{\varepsilon^2}, & r < \varepsilon \\ 1, & r \geq \varepsilon, \end{cases}$$

$$w_z = w_0 - \frac{\Gamma}{l}\begin{cases} \dfrac{r^2}{\varepsilon^2}, & r < \varepsilon \\ 1, & r \geq \varepsilon, \end{cases} \qquad (2)$$

where Γ is the vortex circulation, w_0 is the velocity in the stream axis, and w_z and w_φ are, respectively, the axial and tangential components of the velocity of the inviscid flow. This solution (2) to the Euler equations well describes experimental velocity profiles [6, 7] in various swirling flows (see Fig. 1). Since Eq. (2) involves the second velocity component associated with flow swirl, it is necessary to consider the following equations of the three-dimensional boundary layer [8]:

$$u_y\frac{\partial u_x}{\partial y} + u_z\frac{\partial u_x}{\partial z} = \nu\frac{\partial^2 u_x}{\partial y^2},$$

$$u_y\frac{\partial u_z}{\partial y} + u_z\frac{\partial u_z}{\partial z} = \nu\frac{\partial^2 u_z}{\partial y^2} - \frac{1}{\rho}\frac{\partial p}{\partial z}, \qquad (3)$$

$$\frac{\partial u_y}{\partial y} + \frac{\partial u_z}{\partial z} = 0,$$

[1] *Institute of Thermophysics, Siberian Division,*
   Russian Academy of Sciences,
   pr. Akademika Lavrent'eva 1, Novosibirsk, 630090 Russia
[2] *Laboratoire d'Etudes Thermiques UMR CNRS n 6608,*
   ESIP, avenue du Recteur Pineau 68022 Poitiers Cedex,
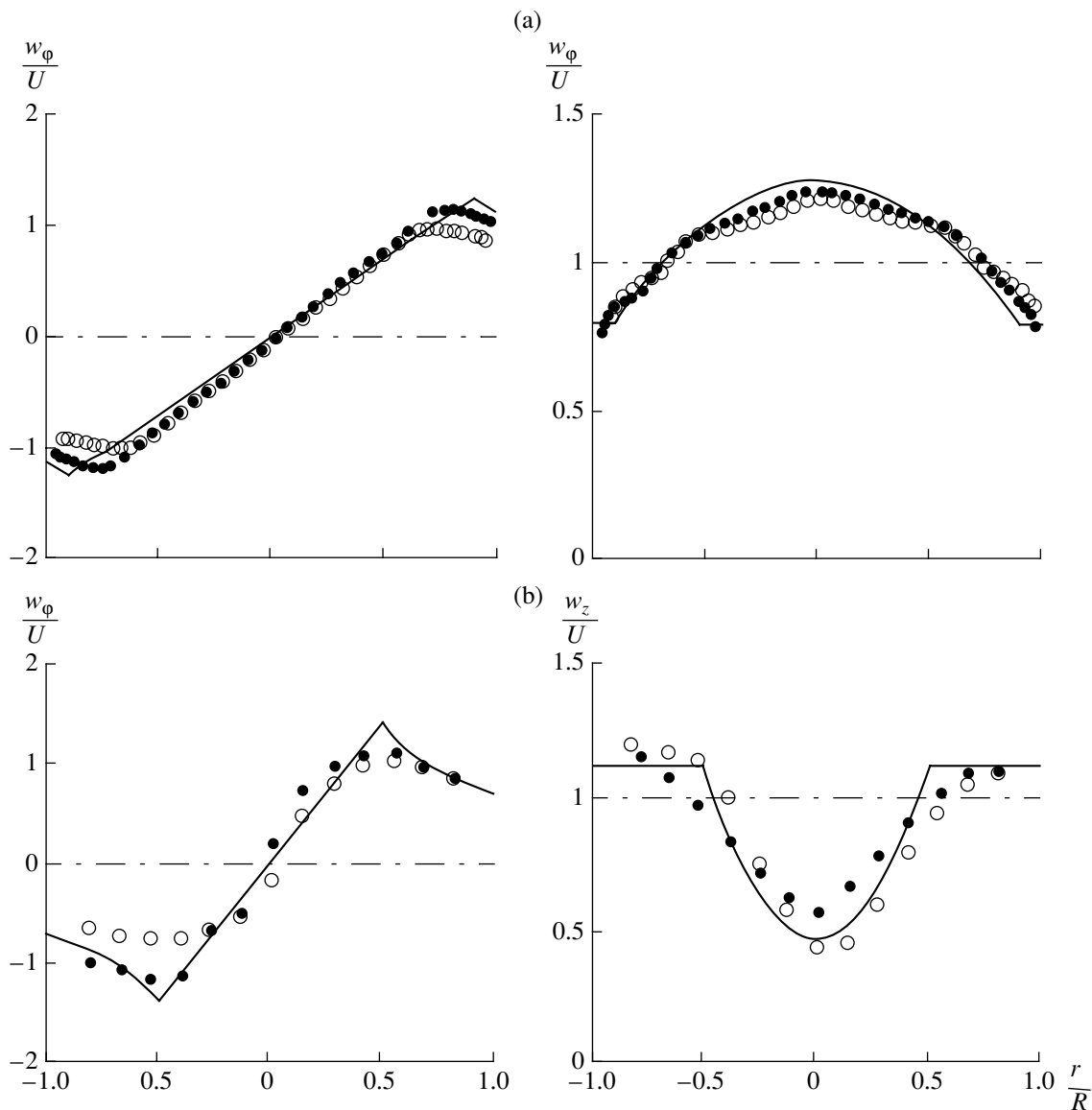   *France*
* *E-mail: okulov@itp.nsc.ru*

Fig. 1. Profiles of the (left panel) tangential and (right panel) axial velocity components for swirling flows with (a) jetlike [6] and (b) tracelike profiles of the axial velocity component: LDA measurements for distances (closed circles) 3–4 and (open circles) 8–9 tube diameters from the swirler and (lines) approximation by Eq. (1).

with the boundary conditions

$$y = 0: u_x = u_y = u_z = 0;$$

$$y = \infty: u_x = w_\varphi(R) \equiv V;$$

$$u_z = w_z(R) \equiv W.$$

Equations (3) were obtained by changing to the reference frame connected with the tube wall: the z axis is oriented along the tube; the x axis coincides with the tangential direction; $y = R - r$ is the distance from the tube wall in the radial direction; $u_x = u_\varphi$, $u_y = -u_r$, and u_z are the velocity components in the boundary layer; and $w_\varphi(R) \equiv V$ and $w_z(R) \equiv W$ are, respectively, the tangential and axial velocity components of inviscid flow (2)

on the tube wall. In addition, the curvature of the tube wall (i.e., radial pressure gradient) was ignored, and we took into account that all the characteristics of the flow do not vary along the x axis, because the flow is axisymmetric.

In view of the assumption that the inviscid flow does not change up to the microelectrode, i.e, that V and W are constant, we have $\dfrac{\partial p}{\partial z} = 0$ and, therefore, arrive at the familiar problem for the boundary layer on a thin plate with the grazing angle. The solution to this problem is expressed in terms of the solution to the Blasius equation ϕ [8] as

$$u_\varphi = u_x = V\phi',$$

$$-u_r = u_y = \frac{1}{2}\sqrt{\frac{\nu W}{z}}(\xi\phi' - \phi), \qquad (4)$$

$$u_z = W\phi'.$$

Therefore, the friction stresses on the tube wall have the form

$$\tau_z = \mu\frac{\partial u_z}{\partial y}\bigg|_{y=0} = 0.332\sqrt{\frac{\mu\rho W}{z}}W,$$

$$\tau_\varphi = \mu\frac{\partial u_x}{\partial y}\bigg|_{y=0} = 0.332\sqrt{\frac{\mu\rho W}{z}}V, \qquad (5)$$

where μ is the dynamic viscosity and ρ is the fluid density.

Turning to the mass transfer processes within the boundary layer with velocity field (4), we write the equation of stationary diffusion in cylindrical coordinates as

$$u_r\frac{\partial c}{\partial r} + u_\varphi\frac{\partial c}{r\partial\varphi} + u_z\frac{\partial c}{\partial z}$$

$$= D\left(\frac{\partial}{r\partial r}\left(r\frac{\partial c}{\partial r}\right) + \frac{\partial^2 c}{r^2\partial\varphi^2} + \frac{\partial^2 c}{\partial z^2}\right), \qquad (6)$$

where the velocity components u_r, u_φ, and u_z within the thin diffusion layer ($R - r \ll \delta$) can be expressed in terms of the friction components given on the wall by Eqs. (5):

$$u_r = -\frac{1}{2}(r-R)^2\left(\frac{1}{R}\frac{\partial}{\partial\varphi}\frac{\partial u_\varphi}{\partial r} + \frac{\partial}{\partial z}\frac{\partial u_z}{\partial r}\right)\bigg|_{r=R},$$

$$u_z = (r-R)\frac{\partial u_z}{\partial r}\bigg|_{r=R}, \quad u_\varphi = (r-R)\frac{\partial u_\varphi}{\partial r}\bigg|_{r=R}. \qquad (7)$$

Here, the equation for the radial velocity component u_r follows from the continuity equation.

Since the curvature of the diffusion layer is ignored, it is possible to go over from the radial coordinate r to the distance from the wall $y = R - r$, and the cylindrical problem reduces in fact to the plane one. The further simplification of Eq. (6) follows from the approximation of the diffusion boundary layer (longitudinal and transverse molecular diffusions are ignored). As a result and in view of Eqs. (7), Eq. (6) takes the form

$$\frac{\tau_z}{\mu}y\frac{\partial c}{\partial z} - \frac{1}{2\mu}\frac{\partial\tau_z}{\partial z}y^2\frac{\partial c}{\partial y} + \frac{\tau_\varphi}{\mu}y\frac{\partial c}{\partial x} = D\frac{\partial^2 c}{\partial y^2}. \qquad (8)$$

Let us consider mass transfer on the surface of a ring microelectrode flash mounted with the wall at the distance d_0 from the entrance section. The second term in the left-hand side of Eq. (8) can be neglected if the ratio $\dfrac{d_0}{z_0}$ is small, i.e., if the characteristic length of the vari-

ance of the concentration c along the microelectrode surface is small compared to the characteristic length of varying the friction stress on the tube wall. Turning the reference frame along the y-axis so that the z-axis coincides with the local direction of the flow near the microelectrode, we represent Eq. (8) in the following form of the familiar Leveque equation [9]:

$$\frac{\sqrt{\tau_\varphi^2 + \tau_z^2}}{\mu}y\frac{\partial c}{\partial z} = D\frac{\partial^2 c}{\partial y^2}.$$

By the change of variables $\eta = y\left(\dfrac{\sqrt{\tau_\varphi^2 + \tau_z^2}}{\mu D z}\right)^{1/3}$, this equation is modified to the ordinary differential equation

$$\frac{\partial^2 c}{\partial\eta^2} - \frac{1}{3}\eta\frac{\partial c}{\partial\eta} = 0.$$

As a result, the surface-average Sherwood number is expressed as

$$\overline{\mathrm{Sh}} = 0.866\left(\frac{\sqrt{\tau_z^2 + \tau_\varphi^2}\big|_{z=z_0}d_0^2}{\mu D}\right)^{1/3}. \qquad (9)$$

The substitution of the friction components given by Eqs. (5) into Eq. (9) provides

$$\overline{\mathrm{Sh}} = 0.6\mathrm{Sc}^{1/3}\left(\frac{d_0}{z_0}\right)^{1/6}\left(\frac{d_0\sqrt[3]{W(V^2 + W^2)}}{\nu}\right)^{1/2}$$

$$= 0.6\mathrm{Sc}^{1/3}\left(\frac{d_0}{z_0}\right)^{1/6}(\mathrm{Re}_{(V,W)})^{1/2}, \qquad (10)$$

where the parameter

$$\mathrm{Re}_{(V,W)} = \frac{d_0\sqrt[3]{W(V^2 + W^2)}}{\nu} \qquad (11)$$

can be treated as an analog of the Reynolds number, which is expressed in terms of the axial and tangential velocity components of the main stream near the cylinder wall.

On the basis of the simplest generalization (10) of the solution to the Leveque problem [9] for describing local mass transfer in swirling flows, we can make the following important remarks.

1. In spite of the simplicity of the model proposed above, solution (10) quite correctly describes the variation of local mass transfer along the entrance region of the mass transfer section. Figure 2 shows mass transfer coefficients $k = \dfrac{\nu\mathrm{Sh}}{d\mathrm{Sc}}$ both measured in [4] and calculated by Eq. (10) for fixed $\mathrm{Re}_{(V,W)}$ (Fig. 3, solid line) characterizing the flow for distances up to 5–6 tube
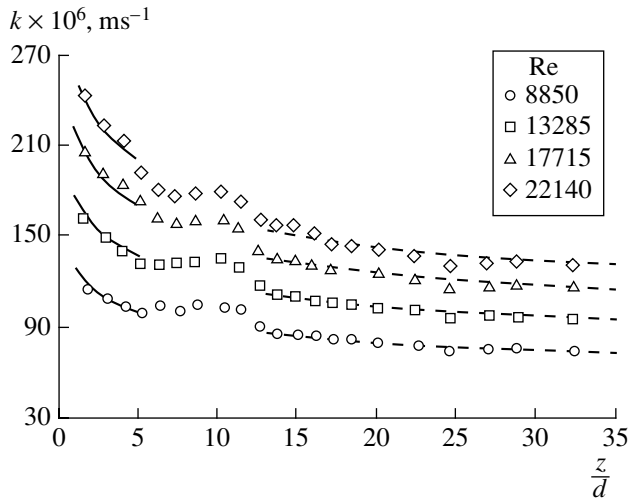
Fig. 2. Mass-transfer coefficients k both measured in [4] and calculated by Eq. (10).
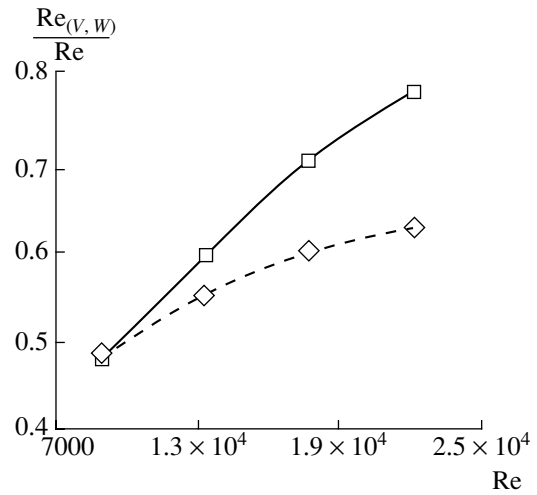

Fig. 3. Relative $\mathrm{Re}_{(V, W)}$ values (solid line) in the entrance region of the mass transfer section and (dashed line) for the developed flow regime.

diameters from a swirler, where the above assumptions of the model are applicable.

2. Function (10) can be successfully applied to describe the variation of local mass transfer not only in the entrance region (where the model assumptions are applicable) but also in the region with the developed flow regime (dashed lines in Fig. 2 in the region from 10 to 30 tube diameters). In this case, $\mathrm{Re}_{(V, W)}$ values are different (dashed line in Fig. 3). This fact is also known for non-swirling flows ($V = 0$). Although Eq. (1) determines the form of the exact solution (10) only in the entrance tube region ($W = U$), Isaev *et al.* [10] emphasized that functions similar to Eq. (1) can be successfully applied to generalize experimental data on mass transfer in developed, laminar, and turbulent flows. In non-swirling flows, this is the fact because the rate-average Reynolds number is a universal similarity parameter even though the laws of varying friction on the wall are different for different flow regimes. For this reason, mass transfer in these flows is well described by

Parameter $\mathrm{Re}_{(V, W)}$ for the fixed rate-average Reynolds number $\mathrm{Re} = 2.8 \times 10^5$

Vortex type	S	$\dfrac{W}{U}$	$\dfrac{V}{U}$	$\dfrac{\mathrm{Re}_{(V, W)}}{\mathrm{Re}}$
Set-up with rotating honeycomb section as a swirler [6]				
Right-handed	0.5	0.85	0.58	0.966
Right-handed	1.0	0.79	1.13	1.145
Set-up with axial-tangential input [7]				
Right-handed	0.1	0.91	0.19	0.923
Right-handed	0.35	0.97	0.41	1.025
Left-handed	0.7	1.12	0.70	1.25

Eq. (1) with different values of empirical parameters c and n.

3. Comparison [1–4] of mass transfer processes in swirling flows in terms of Sherwood number (1) represented as a function of the rate-averaged Reynolds number is incorrect. This conclusion is clear from the table, where the relative values of the parameter $\mathrm{Re}_{(V, W)}$ characterizing local mass transfer for various swirlers and flow swirl numbers S were calculated for the same rate-averaged Reynolds number [6, 7]. Moreover, at least two fundamentally different flow regimes exist in swirling flows. These are flows that involve right- and left-handed helical vortices [5] and have jetlike (convex as in axial flows) and tracelike (concave) profiles of the axial velocity. As a result, the axial velocities near the wall are different for these two regimes even for the same rate-averaged Reynolds number and flow swirl number. In addition, both regimes can be realized in the same flow. This fact was shown for flows with vortex breakdown for the broad Re range from 1500 to 300 000 [11–13]. Due to this uncertainty, it is impossible to characterize local mass transfer in swirling flows by Eq. (1) even when Eq. (1) is refined by introducing a factor characterizing the swirl number [4].

4. We emphasize that the notions of "continuous" and "decaying" swirling flows, which were used in experimental studies [1–4], must be defined more exactly. Indeed, Eq. (10) was obtained in the model of the inviscid flow which is still independent of the developed boundary layer. This means that an experimentalist carrying out LDA measurements in an inviscid core considers that the flow is continuous (open and closed circles in Fig. 1). At the same time, the local friction stress and local mass transfer coefficient (10) decrease along the tube (Fig. 2) such as in a plane plate [8]. This means that an experimentalist conducting electrochem-

ical measurements between electrodes mounted in series regards that the flow is decaying.

ACKNOWLEDGMENTS

REFERENCES

1. P. Legentilhomme, A. Aouabed, and J. Legrand, Chem. Eng. J. **52**, 137 (1993).

2. S. Yapici, M. A. Patrick, and A. A. Wragg, J. Appl. Electrochem. **24**, 685 (1994).

3. S. Yapici, M. A. Patrick, and A. A. Wragg, J. Appl. Electrochem. **25**, 15 (1995).

4. S. Yapici, G. Yazici, C. Ozmetin, *et al.*, Int. J. Heat Mass Transfer **40**, 2775 (1997).

5. S. V. Alekseenko, P. A. Kuibin, V. L. Okulov, and S. I. Shtork, J. Fluid Mech. **382**, 195 (1999).

6. M. Schmidts and V. Vasanta Ram, in *Proceedings of the VIII European Turbulence Conference* (STU, Barcelona, 2000), pp. 121–124.

7. O. G. Dahlhaug, Thesis of Doctor Engineer Degree (NTNU, Trondheim, 1997).

8. H. Shlichting, *Boundary Layer Theory* (McGraw-Hill, New York, 1968; Nauka, Moscow, 1974).

9. J. Leveque, Ann. Mines **13**, 201 (1928).

10. S. I. Isaev, I. A. Kozhinov, V. I. Kofanov, *et al.*, *The Theory of Thermo-Mass Exchange* (Mosk. Gos. Tekh. Univ., Moscow, 1997).

11. S. Leibovich, Annu. Rev. Fluid Mech. **10**, 221 (1978).

12. M. Escudier, Prog. Aerosp. Sci. **25**, 189 (1988).

13. T. Sarpkaya and F. Novak, in *Proceedings of the XXXVII AIAA Aerospace Meeting and Exhibit*; AIAA Pap. **99-0135**, 1 (1999).

Translated by R. Tyapaev

===== **MECHANICS** =====

On the Regularity of Stresses for a Bounded Domain in the Linear Theory of Elasticity[1]

A. I. Koshelev

Presented by Academician N.F. Morozov on March 28, 2002

Received April 5, 2002

The problem of regularity of stresses plays an important role in modern elasticity theory. This problem is closely related to the fracture of materials, appearance of cracks, and certain other extreme situations. It is desirable to obtain explicit estimates for the upper bounds of stress moduli in a closed bounded domain in which the boundary value problem of the elasticity theory is solved.

We consider in a bounded domain $\Omega \subset R^m$, $m \geq 2$, with the boundary $\partial \Omega \in C^{1,\kappa}$, $\kappa > 0$ the equilibrium equations of the elasticity theory

$$L^{(k)}(u) = D_i a_i^{(k)}(x, \varepsilon_{jl}[u]) = -f^{(k)}(x)$$
$$(i, j, k, l = 1, 2, \ldots, m),$$
(1)

where D_i is the operator of differentiation with respect to x_i ($x \in \Omega$) and $f^{(k)}(x)$ is the projection of the mass force $f(x) = \{f^{(1)}(x), f^{(2)}(x), \ldots, f^{(m)}(x)\}$ on the k-axis. The strains $\varepsilon_{jl}[u]$ in the linear theory are given by the formula

$$\varepsilon_{jl}[u] = \frac{1}{2}(D_j u^{(l)} + D_l u^{(j)}),$$
(2)

where $u(x) = \{u^{(1)}(x), u^{(2)}(x), \ldots, u^{(m)}(x)\}$ denotes the vector function of displacements.

The coefficients $a_i(x, \varepsilon_{jl}) = \{a_i^{(1)}(x, \varepsilon_{jl}), a_i^{(2)}(x, \varepsilon_{jl}), \ldots, a_i^{(m)}(x, \varepsilon_{jl})\}$ in Eqs. (1) are determined by the physical dependences

$$\sigma_{ik} = a_i^{(k)}(x, \varepsilon_{jl}[u]).$$
(3)

From (2) and (3), it follows that pointwise estimates for stresses can be obtained from the same estimates for the first derivatives of the solutions to Eqs. (1). In the case of a linear homogeneous isotropic medium, these can

be estimates written in the form

$$\sigma_{ik} = \lambda \operatorname{div} u \delta_{ik} + 2\mu \varepsilon_{ik}[u],$$
(4)

where $\lambda, \mu = \operatorname{const} > 0$ are the Lamé constants.

We now consider the matrix

$$A = \left\{ \frac{\partial a_i^{(k)}}{\partial p_j^{(l)}} \right\} \quad (i, j, k, l = 1, 2, \ldots, m).$$
(5)

It is known that in the general case of system (1), this matrix is positive but not positive definite.

If the operator $L(u)$ is defined on the twice differentiable functions then the system of equations (1) can be written in the form

$$L(u) \equiv \mu \Delta u + (\lambda + \mu)\nabla(u) = -f(x).$$
(6)

This system is strongly elliptic.

The present paper is devoted to the pointwise explicit estimation of the first derivatives of the solutions to Eq. (6), which satisfy the boundary condition

$$u|_{\partial\Omega} = 0.$$
(7)

The estimates are obtained in a certain strong norm. If the norm of f in $\mathscr{L}_2$ is sufficiently small with respect to its strong norm, then the inequalities acquire an explicit form.

We write system (6) in the following form:

$$L^{(k)}(u) \equiv D_i a_i^{(k)}(x, D_j u^{(l)}) = -f^{(k)}(x),$$
$$k = 1, 2, \ldots, m,$$
(8)

where

$$a_i^{(k)}(x, p_j^{(l)}) = (\lambda + \mu)p_h^{(h)}\delta_{ik} + \mu p_i^{(k)}$$
$$(i, h = 1, 2, \ldots, m)$$

and the summation over h occurs from 1 to m.

Therefore, the ellipticity matrix A (5) has the following elements:

$$\frac{\partial a_i^{(k)}}{\partial p_j^{(l)}} = (\lambda + \mu)\delta_{ik}\delta_{jl} + \mu\delta_{ij}\delta_{kl}.$$

---

[1] This article was submitted by the author in English.

St. Petersburg State University,
Universitetskiǐ pr. 28, Staryǐ Peterhof,
St. Petersburg, 198504 Russia

It is clearly seen that the eigenvalues $\lambda_i(x, p)$ of A are equal only to either μ or $m\lambda + (m + 1)\mu$.

Therefore,

$$\lambda = \inf_{i, x, p} \lambda_i = \mu \quad \text{and} \quad \Lambda = \sup_{i, x, p} \lambda_i = m\lambda + (m + 1)\mu. \quad (9)$$

Thus, the dispersion $K = (\Lambda + \bar{\lambda})^{-1}(\Lambda - \bar{\lambda})$ of the spectrum is

$$K \equiv \frac{m(\lambda + \mu)}{m\lambda + (m + 2)\mu} < 1. \quad (10)$$

In [1], the exact results related to the existence of generalized solutions to Eqs. (1), which belong to $W_2^{(1)}(\Omega)$ for basic problems of the elasticity theory in the case of hardening, were obtained. Some results concerning the existence of regular (continuous, continuously differentiable, satisfying the Hölder condition) solutions to the system of equations (1) and (8) were obtained in [2–5]. Some of these results contain sharp conditions imposed on the spread of K. When these conditions are valid, the generalized solution to problem (7), (8) is of the Hölder type (see, e.g., [2, Chapter 5; 4, Chapters 3 and 4]).

We will consider the functional spaces $W_{2,\alpha}^{(k)}(\Omega; x_0)$ that contain functions having all k generalized derivatives with the finite norm

$$\|u\|^2_{W_{2,\alpha}^{(k)}(\Omega; x_0)} = \sum_{|\beta| = k} \int_\Omega |D^\beta u|^2 r^\alpha dx + \int_\Omega |u|^2 dx. \quad (11)$$

Here β ($\beta_1, \ldots, \beta_m$) is the length multiindex $|\beta| = \beta_1 + \beta_2 + \ldots + \beta_m$, $D^\beta = D_1^{\beta_1} D_2^{\beta_2} \ldots D_m^{\beta_m}$, $r = |x - x_0|$, $x_0 \in \Omega$, and $\alpha = 2 - m - \gamma$ ($0 < \gamma < 1$). For $k = 0$, the space $W_{2,\alpha}^{(0)}(\Omega; x_0)$ coincides with the space $\mathcal{L}_{2,\alpha}(\Omega; x_0)$.

We now consider the space $H_{2,\alpha}^{(k)}(\Omega) \subset W_{2,\alpha}^{(k)}(\Omega; x_0)$. In this space, the norm is defined by the formula

$$\|u\|_{\alpha, k} = \sup_{x_0 \in \Omega} \|u\|_{W_{2,\alpha}^{(k)}(\Omega; x_0)}. \quad (12)$$

We also consider the space $H_{2,\alpha}^{(k)}$ in which the norm can be introduced in a different manner. Let $B_\delta(x_0) = \{x: |x - x_0| < \delta\}$, and $\Omega_\delta(x_0) = B_\delta(x_0) \cap \Omega$. Then, we take a fixed sufficiently small $\delta_0 > 0$. The norm

$$\|u\|_{\alpha, k} = \sup_{x_0 \in \Omega, \delta \leq \delta_0} \|u\|_{W_{2,\alpha}^{(k)}(\Omega; x_0)} \quad (13)$$

is equivalent to norm (12). These spaces were first introduced in a similar way by Morrey [6] and applied by Nirenberg [7] is studies of the regularity problem for the second-order quasilinear elliptic equations with two variables.

Note that for $\alpha = 2 - m - 2\gamma$ $(0 < \gamma < 1)$, we have the embedding

$$H_{2,\alpha}^{(k)}(\Omega) \subset C^{k-1, \gamma}(\Omega). \quad (14)$$

It is known that for arbitrary $\eta > 0$, the inequality

$$|u(x_0)|^2 \leq \eta \int_{B_1(x_0)} |Du|^2 |x - x_0|^\alpha dx + C_0(\eta) \int_{B_1(x_0)} |u|^2 dx$$

holds. Here, $\alpha = 2 - m - \gamma$ $(0 < \gamma < 1)$, $|S|$ is the surface of the unit sphere in R^m and

$$C_0(\eta) = 2m|S|^{-(m/2\gamma + 1)} \gamma^{-m/2\gamma} \eta^{-m/2\gamma}.$$

(See [6, formula (2.1.21)]). From here, we arrive at the inequality

$$|u(x_0)|^2 \leq m^{\frac{4\gamma}{m + 2\gamma}} (|S|\gamma)^{-1} \left(1 + \frac{2\gamma}{m}\right)$$

$$\times \left(\int_{B_\delta(x_0)} |Du|^2 r^\alpha dx\right)^{\frac{m}{m + 2\gamma}} \left(\int_{B_\delta(x_0)} |u|^2 dx\right)^{\frac{2\gamma}{m + 2\gamma}}. \quad (15)$$

In [2–5], we have assumed that the coefficients $a_i(x, p)$ in Eqs. (1) satisfy the following conditions:

(1) they are continuously differentiable with respect to p for an arbitrary bounded set $\{p\}$ and measurable for almost all $x \in \Omega$;

(2) the matrix A is symmetric and its eigenvalues $\{\lambda_i(x, p)\}$ satisfy the conditions

$$\inf_{i, x, p} \lambda_i(x, p) = \lambda_{\inf} > 0 \quad \text{and} \quad \sup_{i, x, p} \lambda_i(x, p) = \Lambda_{\sup} < \infty;$$

(3) for $\forall q \in (1, q_0]$, where q_0 is a sufficiently large number and $\forall u \in W_q^{(1)}(\Omega)$, $a_i(x, Du) \in \mathcal{L}_q(\Omega)$;

(4) for $\forall u \in W_{2,\alpha}^{(1)}(\Omega)$, $a_i(x, Du) \in \mathcal{L}_{2,\alpha}(\Omega; x_0)$ $\frac{\partial a_i}{\partial x_i} \in \mathcal{L}_{2,\alpha}(\Omega; x_0)$, and $f \in \mathcal{L}_{2,\alpha}(\Omega; x_0)$ for arbitrary $x_0 \in \overline{\Omega}$.

It is evident that all these conditions hold for system (6).

In [3, Theorem 5.5.1; 8], Chelkak proved that if the basic conditions are satisfied and the inequality

$$K\left\{1 + \frac{(m - 2)^2}{m - 1}\right.$$

$$\times \left[1 + \max\left\{0, \frac{2m(m - 2)(m - 4)}{9(m^2 - 1)}\right\}\right]\right\}^{1/2} < 1 \quad (16)$$

holds, then the solution to problem (8) with boundary condition (7) belongs to $C^{1, \gamma}(\overline{\Omega})$. For $m = 2$, inequal-

ity (16) is satisfied, since $K < 1$. For $m = 3$, the condition (16) leads to the inequality

$$\frac{3}{2}K < 1, \tag{17}$$

which yields the condition of smallness for the dispersion of the spectrum of the quadratic form A.

On the basis of inequality (16), the following theorems can be proved.

Theorem 1. *Let* $\alpha = 2 - m - 2\gamma$ *with* $m = 2$ *or* $m = 3$, $f \in \mathscr{L}_{2,\alpha}(\Omega; x_0)$, $x_0 \in \overline{\Omega}$, *and* $\delta_0 > 0$ *be a fixed constant, whose smallness is determined by local properties of the boundary* $\partial\Omega$.

If the inequality

$$K\sqrt{1 + \frac{(m-2)^2}{m-1}} < 1 \tag{18}$$

holds, then for the solution of problem (6), (7), *which is extended in the odd manner together with f locally through* $\partial\Omega$, *an estimate*

$$\sup_{x_0 \in \Omega, \delta < \delta_0} \int_{B_\delta(x_0)} |D^2u|^2|x - x_0|^\alpha dx$$

$$\leq \left[\frac{4}{(\Lambda + \bar{\lambda})^2}\frac{1}{\left(1 - K\sqrt{1 + \frac{(m-2)^2}{m-1}}\right)^2} + O(\gamma) + \eta\right]$$

$$\times \sup_{x_0 \in \Omega, \delta < \delta_0} \int_{B_\delta(x_0)} \left(\frac{2|f|}{\Lambda + \bar{\lambda}}\right)^2 |x - x_0|^\alpha dx$$

$$+ C \sup_{x_0 \in \Omega, \delta < \delta_0} \left(\int_{B_\delta(x_0)} |f|^2 dx + \int_{B_\delta(x_0)} |Du|^2 dx\right) \tag{19}$$

is valid with the positive constant C depending only on δ_0, α *and an arbitrary small* $\eta > 0$.

Theorem 2. *Under conditions of the previous theorem for* $m = 2$, *the exact inequality*

$$\sup_{x_0 \in \Omega, \delta < \delta_0} \int_{B_\delta(x_0)} |D^2u|^2|x - x_0|^\alpha dx$$

$$\leq \left[\frac{1}{\mu^2} + O(\gamma) + \eta\right]\sup_{x_0 \in \Omega, \delta < \delta_0} \int_{B_\delta(x_0)} |f|^2|x - x_0|^\alpha dx$$

$$+ C\sup_{x_0 \in \Omega, \delta < \delta_0} \left(\int_{B_\delta(x_0)} |f|^2 dx + \int_{B_\delta(x_0)} |Du|^2 dx\right) \tag{20}$$

holds.

Indeed, the constant ahead of the first integral in inequality (20) can be obtained from estimate (19) if we substitute there the values of $\bar{\lambda}$, Λ, K from formulas (9) and (10) for $m = 2$. The accuracy of the estimate can be proved by the following example. Let $\Omega = B_1(0)$, $u^{(1)} =$

$(r^{1+\varepsilon} - 1)q(\varphi)$ and $u^{(2)} = 0$, where (r, φ) be the polar coordinates. Here $\varepsilon > 0$ is sufficiently small and $q(\varphi)$ is the solution to the problem $q'' + q = p_n(\varphi)$, $q(-\pi) = q(\pi) = 0$, with $p_n(\varphi) = 0$ for $\varphi \in [-\pi, -(2n)^{-1}] \cup [(2n)^{-1}, \pi]$, $p_n(\varphi) = \sqrt{n}$ for $\varphi \in (-(2n)^{-1}, (2n)^{-1})$ $(n = 1, 2, \ldots)$. It is clear that $u = (u^{(1)}, u^{(2)})$ is the solution to problem (6), (7), where $f^{(1)} = -r^{\varepsilon - 1}(q'' + q)(\mu + (\lambda + \mu)\sin^2\varphi) + O(\varepsilon)$ and $f^{(2)} = r^{\varepsilon - 1}(q'' + q)(\lambda + \mu)\sin\varphi\cos\varphi + O(\varepsilon)$.

By simple considerations, it can be proved that with an accuracy of $O(n^{-1})$, the supremum of the integrals is attained for $x_0 = 0$. It can be shown by elementary calculations that the constant ahead of the first integral at the right-hand side in (19) is equal to $\mu^{-2} + O(\gamma) + \eta + O(n^{-1})$.

It is worth noting that the application of estimate (15) for the derivatives of the solution to problem (6), (7) with the help of (20) leads to the explicit pointwise estimates for these derivatives.

In fact, if the norm of f in $\mathscr{L}_2(\Omega)$ is sufficiently small compared to the norm of f in $\mathscr{L}_{2,\alpha}(\Omega)$ for $\alpha = 2 - m - 2\gamma$ $(0 < \gamma < 1)$, then for $m = 2$, inequality (15) for the derivatives can be written in the explicit form

$$|Du|^2\big|_{x = x_0} \leq \left[\frac{1}{2\pi\gamma\mu^2} + O(\gamma)\right]$$

$$\times \sup_{\delta < \delta_0, x_0 \in \overline{\Omega}} \left(\int_{B_\delta(x_0)} |f|^2|x - x_0|^\alpha dx\right)^{\frac{1}{1+\gamma}}\left(\int_{B_\delta(x_0)} |Du|^2 dx\right)^{\frac{\gamma}{1+\gamma}}.$$

In this case, the corresponding estimates for the stresses follow from formulas (4).

When $m = 3$, condition (17) is also exact, since there exists an example of system (1) (see [6]) when the generalized solution can loose its regular properties provided that condition (17) is not true.

REFERENCES

1. I. I. Vorovich and Yu. P. Krasovskiĭ, Dokl. Akad. Nauk **126**, 740 (1959) [Sov. Phys. Dokl. **4**, 701 (1959)].

2. A. I. Koshelev, *Regularity of Solutions to Elliptic Equations and Systems* (Nauka, Moscow, 1986).

3. A. Koshelev and S. Chelkak (Teubners Phys. Techn. Samml. 1985), vol. 77.

4. A. Koshelev, *Regularity Problem for Quasilinear Elliptic and Parabolic Systems*, Springer Lect. Notes Math. (Springer, Berlin, 1995), vol. 1614.

5. A. I. Koshelev and S. I. Chelkak, *Regularity of Solutions to Certain Boundary Value Problems for Quasilinear Elliptic and Parabolic Systems* (St.-Peterburg. Univ., St. Petersburg, 2000).

6. Ch. Morrey, Trans. Am. Math. Soc. **43**, 126 (1938).

7. L. Nirenberg, Commun. Pure Appl. Math. **6**, 103 (1953).

8. S. I. Chelkak, Izv. Vyssh. Uchebn. Zaved., Mat. **1** (260), 33 (1984).

======= **MECHANICS** =======

Classification of Trajectories of the Plane-Parallel Motion of an Axisymmetric Body in a Strong Medium with Flow Separation

I. V. Simonov

Presented by Academician A.Yu. Ishlinskiǐ April 1, 2002

Received April 12, 2002

   Various scenarios for the motion of a thin pointed body in an elastoplastic medium for an asymmetric separation are presented for various values of initial perturbations, body shape, and separation angle, which is the parameter appearing in the separation criterion. The physical model [1] in which a relation between kinematic and force factors on the contact area is postulated on the basis of exact solutions [2, 3] and experiment [4] reduces to the Cauchy problem for a set of integrodifferential equations of motion of a body, which is solved numerically with a high accuracy. First, the practical stability of linear motion with constant axial velocity is studied. Comparison with local stability criteria [1] is given. In the instability region, a soft relaxation regime whose limiting cycle is the circular motion is found. A classification of trajectories with allowance for drag is proposed. It is shown that a trajectory can, in principle, pass close to a given one, in particular, to that with back ejection from the day surface when a striker enters a half-space (the effect previously found experimentally by Yu.K. Bivin). Since there is no reliable verification of the separation criterion taken from engineering practice, it is important that the characteristic features of trajectories depend only slightly on separation angle. This study is promising for designing penetrators, i.e., stations for investigating inner layers of extraterrestrial objects [5] and for other purposes [6].

   1. A rigid axisymmetric body moves with a high velocity in an unbounded isotropic and homogeneous elastoplastic medium. The length of the body L and its largest radius r_{m} are used as the longitudinal and transverse length scales, respectively. Let $R = R(l) = \dfrac{r}{r_{\mathrm{m}}}$ be the dimensionless meridian equation in the cylindric coordinates R, ϕ, and l rigidly bound to the body and to the local Cartesian coordinate system: $x = l_{\mathrm{c}} - l$, $y =$

_____

Institute for Problems in Mechanics,
Russian Academy of Sciences,
pr. Vernadskogo 101, Moscow, 117526 Russia

$R\cos\phi$, and $z = R\sin\phi$, where l is the distance from the body nose; $l = l_{\mathrm{c}}$ and $R = 0$ are the coordinates of the center of mass. We suppose that the body is thin:

$$\varepsilon = \frac{r_{\mathrm{m}}}{L} \ll 1, \quad \varepsilon\beta \ll 1, \quad \beta = \frac{dR}{dl}, \quad 0 < l < 1. \quad (1)$$

At the initial time $t = 0$, the velocity $\mathbf{v}_0$ of the body's center of mass and the rotation angular velocity $\mathbf{\Omega}_0$ relative to this center in the plane formed by the vector $\mathbf{v}_0$ and the body axis are given, and there are no yaw or other rotations. We denote the vectors of current transport, angular, total, and normal (to the surface) velocities as

$$\mathbf{v} = (v_x, v_y, 0), \quad \mathbf{\Omega} = (0, 0, \Omega),$$

$$\mathbf{V} = \mathbf{v} + \mathbf{\Omega} \times (x, y, z), \quad V_n = \mathbf{n}\mathbf{V} = \varepsilon\delta v_x,$$

$$\delta = \beta - a\cos\phi, \quad a = -\omega x - \eta,$$

$$\omega = \frac{\Omega L}{\varepsilon v_x}, \quad \eta = \frac{v_y}{\varepsilon v_x}.$$

The dimensionless functions ω and η can take values $O(1)$. The mass of the body is expressed in terms of its average density ρ_1 and the length l_{e} of a cylinder equivalent in mass and midsection: $m = \pi r_{\mathrm{m}}^2 L l_{\mathrm{e}} \rho_1$. The incompressible medium is characterized by the density ρ_0, shear modulus μ, and von Mises yield stress τ_{d}. A plastically compressible (porous) medium can be considered as being packed far from the body, and ρ_0 is its density in the packed state.

   The separation criterion taken from engineering applications is that the inclination angle of an elementary area of the body surface to the flow velocity takes the critical value β_* at infinity:

$$\delta^* \equiv \delta - \beta_*(\sigma_{ij}^0, V) = 0. \quad (2)$$

For low velocities, $\beta_* = 0$, which means perfect separation from midsection edges, and this angle increases

with velocity and decreases with an increase in initial compressing stresses σ_{ij}^0 in the medium. In [7], an experimental procedure for determining β_* was proposed. We denote the wetting area as S_+ (under condition that $\delta^* > 0$) and the separation area as S_- ($\delta^* < 0$); $S = S_+ + S_-$ is the total surface of the body. We consider only regimes without the flow attachment on the body surface. According to the local-interaction method [2], which was justified theoretically [3] and experimentally [4], the vector of contact stresses $\boldsymbol{\Sigma}$ on each element of the surface S_+ is the sum of the hydrodynamic and strength terms and thus is directly related to the kinematic characteristics of the body motion:

$$\boldsymbol{\Sigma} = \tau_S \mathbf{n}_\tau - \sigma_n \mathbf{n}, \quad \sigma_n = \frac{1}{2} C_x \rho_0 V^2 + b_f \tau_d \quad (S_+);$$

$$\boldsymbol{\Sigma} = 0 \quad (S_-), \tag{3}$$

$$C_x = C_f \delta^2 \varepsilon^2, \quad b_f = \ln \frac{4\mu}{\tau_d} - 1, \quad C_f = \ln \frac{\mu}{\tau_d} + 2.55.$$

Here, $\tau_S = \text{const} \le \tau_d$ is the plastic friction (the law corroborated experimentally [4]) and the unit vector $\mathbf{n}_\tau$ in the direction of sliding is equal to $(-1, 0, 0)$ in the approximation under consideration. In this case, we neglect the initial stresses and virtual masses. The square dependence for C_x is valid up to values $C_x < 0.2$. This fact, Eqs. (3), and the definition of quantities δ and ε provide restrictions for the angles β, η, and $l_c\omega$. Generally speaking, coefficients C_f and b_f [4] can be set by different methods based on experiments or solutions to other flow problems [8]. The coefficient b_f for typical values of $\frac{\mu}{\tau_d} = 10^2$–$10^3$ is equal to $b_f = 5$–8. The physical separation condition $\sigma_n = 0$ is violated because the model is approximate: σ_n is treated not as a pointwise value but as a value averaged over the surface element.

2. Equations of motion of a pointed axisymmetric body reduce to an autonomous system of integrodifferential equations for the functions κ, η, and ω, and the Cauchy problem is formulated:

$$\kappa' = 2\kappa\varepsilon^2(f_\kappa - \omega\eta), \quad \eta' = f_\eta - \omega, \quad \omega' = jf_\omega,$$

$$\boldsymbol{\kappa} = (\kappa, \eta, \omega) = \boldsymbol{\kappa}_0, \quad \xi = 0; \quad (') = \frac{d}{d\xi}, \tag{4}$$

$$\mathbf{f} = (f_\kappa, f_\eta, f_\omega)$$

$$= D\iint_{S_+} (\tau\kappa + \beta\sigma, -\sigma\cos\phi, -\sigma x\cos\phi) R \, dl \, d\phi$$

$$= D\int_0^1 (\Theta, \Phi, (l_c - l)\Phi) R(l) \, dl, \tag{5}$$

$$\Theta = \phi_0 \Theta_1 + \Theta_2, \quad \Phi = 2a\beta\phi_0 + \Psi \operatorname{sgn} a, \quad 0 < l < 1,$$

$$\Theta_1 = 2(\kappa\tau + \kappa\beta + \beta^3) + \beta a^2,$$

$$\Theta_2 = \beta|a|(4\beta - \beta^*)\sqrt{1 - q^2} H(1 - q^2),$$

$$\Psi = \left\{ 2\kappa + \beta^2 + \frac{1}{3}a^2(2 + q^2) - \beta\beta^* \right\}$$

$$\times \sqrt{1 - q^2} H(1 - q^2),$$

$$q = \frac{\beta^*}{a} \quad \kappa = \frac{c^2}{v_x^2}, \quad \xi: \ d\xi = \frac{v_x dt}{L}, \quad c^2 = \frac{2b_f \tau_d}{\varepsilon^2 \rho_0 C_f},$$

$$D = \frac{\rho C_f}{2\pi l_e}, \quad \rho = \frac{\rho_0}{\rho_1}, \quad j = \frac{mL^2}{I}, \quad \tau = \frac{\tau_S}{\varepsilon b_f \tau_d}, \tag{6}$$

$$\phi_0 = \begin{cases} \pi, & q\operatorname{sgn} a \ge 1 \\ 0, & q\operatorname{sgn} a \le -1, \end{cases}$$

$$\phi_0 = \begin{cases} \pi - \phi^*, & a > 0, \ |q| < 1 \\ \phi^*, & a < 0, \ |q| < 1, \end{cases}$$

$$\sigma = \kappa + \delta^2, \quad \beta^* = \beta - \beta_*, \quad \phi^* = \arccos q.$$

Here, H is the step function, I is the principal moment of inertia of the transverse rotation, $j \sim 10^1$, criterion (2) is used, and quantities on the order of $O(\varepsilon^2)$ are rejected. The angle values $\phi_0 = \pi$, 0, or $\phi_0 \ne \pi$, 0, determine the character of flow around a parallel: (i) continuous, (ii) complete separation, or (iii) partial separation. Unknown functions depend on the body shape and on eight dimensionless parameters. In the model, only the separation angle β_* remains undetermined; its effect will be studied parametrically. The quantity κ can be characterized as the ratio of the strength resistivity to the velocity head. During the body motion, this ratio varies within the range $\kappa_0 < \kappa < \infty$, and dynamic set (4)–(6) adequately describes almost all stages of decelerated motion of the body.

The asymptotic orders of Eqs. (4) are different: $O(\kappa\varepsilon^2)$ for the first one, and $O(\kappa)$ for the remaining equations because the lateral resistance dominates over the axial resistance for a thin body. This fact makes it possible to investigate the practical stability of the linear motion when the axial velocity is constant.

3. We carried out the series of calculations for $\kappa = \text{const}$ and a parabolic body with allowance for the entrance into the half-space without a splash:

$$R(l) = \beta_0 l - (\beta_0 - 1)l^2,$$

$$\beta(l) = \beta_0 - 2(\beta_0 - 1)l, \quad 0 < l < 1.$$

We fix $\varepsilon = 0.065$, $D = 0.115$, $j = 5.5$, and $\tau = 1$ and vary the parameters κ_0, β_0, β_*, and l_c. First, we consider the case of $\beta_* = \beta(1)$, where the separation areas of meridian length Δ appear near the stern for any perturbations $\gamma = (\eta, \omega)$. The numerical experiment points to the bifurcation of the solution on a certain surface $l_i = l_i(\kappa_0, b_0, \dots)$, $l_a(\kappa, b_0, \dots) \le l_i \le l_s(\kappa, b_0, \dots)$ in the phase space of parameters: disturbances decay for $l_c < l_i$ and grow for $l_c > l_i$ (exponentially for small perturbations). For $l_c < l_a$ or $l_c > l_s$, disturbances decay or grow for arbitrary initial conditions. The numerical value of l_i tends to l_s according to the stability criteria in the Lyapunov sense [1] when disturbances decrease; l_a is the absolute critical value. For example, $l_s = 0.85817$ and $l_a = 0.6391$

for $\beta_0 = \dfrac{3}{2}$, $\beta_* = 0.5$, and $\kappa_0 = 2$.

The bifurcation region can contract to a point ($l_a = l_s$) in other cases, for example, when the separation-area boundary is localized near the center of the body for $\beta_* \approx \beta(0.5)$.

In the instability region $l_c > l_i$, stabilization occurs for a finite time: $\gamma, \Delta \longrightarrow \gamma_*$, and Δ_*. The limiting cycle is the circular motion of radius $R_* = \dfrac{1}{\varepsilon^2 \omega_*}$: the moment of forces vanishes, and the constant resultant force induces centripetal acceleration. With increasing l_c, amplitudes γ_* increase, and finite lengths Δ_* rapidly attain a maximum. The calculations point to global orbital stability.

In the regime of a continuous flow around a lateral surface, we have $\Phi = -2\beta\pi(\omega x + \eta)$, integrals (5) are calculated analytically, and, for $\kappa = \text{const}$, Eqs. (4) reduce to a homogeneous set of linear equations for unknown ω and η with, generally speaking, nonzero determinant: the solutions exponentially increase or decay; i.e., the limiting cycle does not exist. An analysis of small separation areas [1] leads to a similar conclusion, which is corroborated by the calculations: even near the critical number ($l_c \longrightarrow l_s + 0$) and for small initial perturbations, the solution has asymptotic behavior with finite separation areas.

As an example, we consider a cone ($\beta_0 = 1$, $\beta_* = 0$) moving under small perturbations in the regime of continuous flow. Evolution is determined by the critical value $l_g = 0.68674$ [1]. We recall that $l_c = 0.75$ for a continuous homogeneous cone, and its motion is unstable, which was corroborated experimentally. A cone is often used in experiments, in particular, when the penetrations of axisymmetric and three-dimensional configurations are compared. In this case, the stability of its
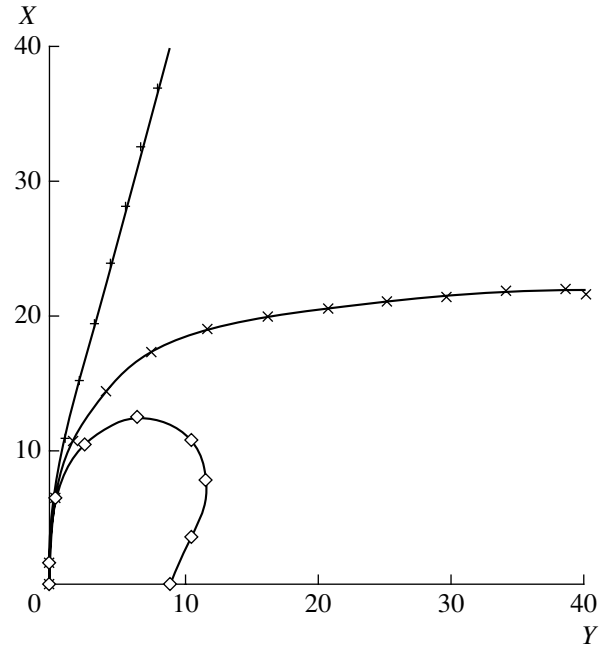

Fig. 1. Trajectories of a parabolic body with the beginning of separation at the stern point for $\kappa_0 = (2, -0.5, 0.5)$.
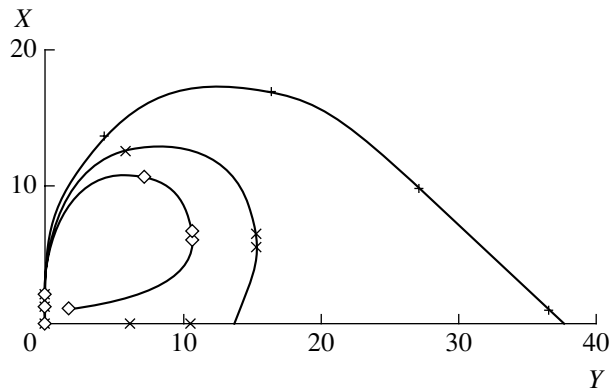

Fig. 2. Trajectories of a parabolic body with the beginning of separation at the stern point for $\kappa_0 = (1, -0.5, 0.5)$.

motion must be provided for the correctness of this comparison.

When $l_c > l_g$ for the cone, the calculations show that perturbations increase; then, an asymmetric separation area is developed and established. Its length Δ_* for values l_c close to the critical value is small; and then, in the narrow interval $0.71 < l_c < 0.7119$, it increases rapidly up to the total length of the body. The limiting cycle is the circumference of radius $6L$ when $\Delta_* = 1$. In the interval $0.72 < l_c < 0.8$, the behavior is the same; however, the separation area is shortened beginning with $l_c = 0.8$ and then is localized near the cone nose.

4. We carried out the calculations taking into account body deceleration ($\kappa \ne \text{const}$). The coordinates
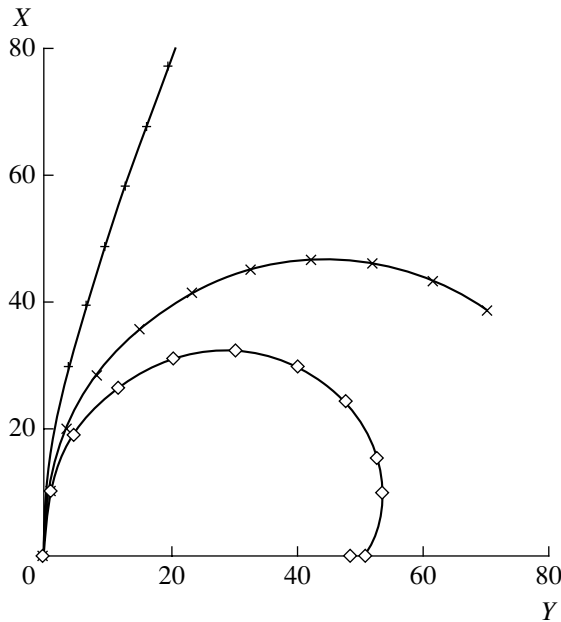
Fig. 3. Trajectories of a parabolic body with the beginning of separation at the point $l = 0.5$ for $\kappa_0 = (2, -0.5, 0.5)$.
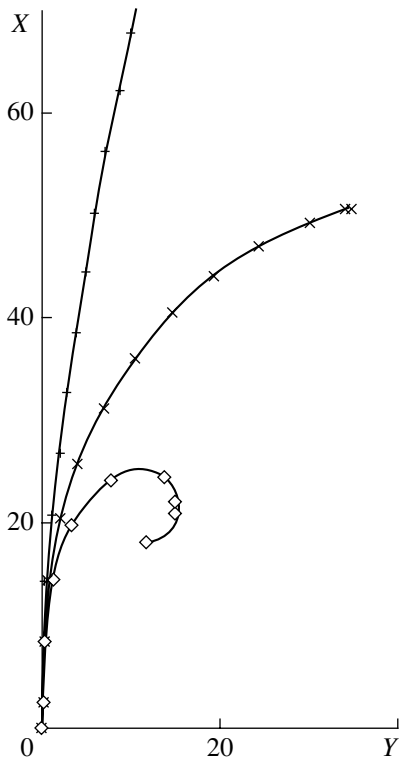

Fig. 4. Trajectories of a cone for $\kappa_0 = (2, -0.5, 0.3)$.

(X, Y) of the body center of mass were calculated with allowance for entry into the day surface $Y = 0$. Figures 1 and 2 show the trajectories for $\kappa_0 = 2, 1$; $\gamma_0 = (-0.5, 0.5)$; $l_c = (+)\ 0.6$, $(\times)\ 0.625$, $(\diamond)\ 0.65$, and the same remaining parameters. For $\kappa_0 = 1$, $l_c = 0.6 > l_i(1)$, and

the kinetic energy is twice as high as the energy for the case $\kappa_0 = 2$, where $l_i(2) > 0.6$ and the trajectory is almost linear for $l_c = 0.6$ in Fig. 1, whereas it is curvilinear in Fig. 2 due to the axial velocity. In both figures, there are trajectories that are curvilinear at the initial section and then become linear because unstable motion becomes stable when the velocity decreases. However, this behavior is observed only when the value l_c is close to the critical value $l_i(\kappa_0)$. Certain curves are classified among inverted trajectories when the stopping point (X_m, Y_m) of the body lies outside the half-space: $X_m \leq 0$. In this case, the striker describes a loop with ejection from the day surface.

Due to deceleration, not all the curvilinear sections are close to the circumference arcs as for $\kappa = \text{const}$, whereas "unstable" trajectories of the same body are close to the arcs (Fig. 3), but for $\beta_* = 1$ (in this case, the separation line is localized near the geometric center of the body) $l_c = (+)\ 0.45$, $(\times)\ 0.49$, and $(\diamond)\ 0.54$; $\kappa_0 = (1, -0.5, 0.5)$.

When the moment of inertia varies by a factor of 3, there are no essential modifications. The trajectories of the cone in Fig. 4 {$l_c = 0.67$, 0.69, and 0.71; $\kappa_0 = (2, -0.5, 0.3)$} are characterized by a sharp transition from weakly curved to strongly curved trajectories.

We propose the following classification of trajectories:

(1) linear trajectories with a weakly curved initial section if the stability criterion $l_c < l_i(\kappa_0)$ is satisfied; in this regime, the body penetrates to the maximum depth;

(ii) trajectories that are curved at the initial section and then linear if $l_c \in \Lambda^+(l_i)$, where Λ^+ is the right-hand neighborhood of the point l_i; in this case, the striker can move away, move parallel, or approach the day surface so that inversion of the trajectory is possible;

(iii) curvilinear trajectories close to a circumference arc if the center of mass l_c lies to the right from the neighborhood $\Lambda^+(l_i)$; the trajectory can end inside a target or be inverted.

5. Thus, the investigation of practical stability showed that large disturbances can considerably reduce the stability inherent in the motion of a body with small perturbations; in certain cases, stability can depend only slightly on the magnitude of perturbations. We established orbital stability; i.e., the limiting cycle is independent of initial perturbations and depends only slightly on the separation angle in the regime of developed separation. It is of methodical importance that a curvilinear trajectory qualitatively close to a given one is possible for essentially different separation parameters. This fact indicates that the basic characteristics of the motion under investigation depend only slightly on the choice of the separation criterion, which, generally speaking, must be checked and improved.

REFERENCES

1. I. V. Simonov, Prikl. Mat. Mekh. **64**, 311 (2000).

2. A. Ya. Sagomonyan, *Penetration* (Mosk. Gos. Univ., Moscow, 1974).

3. L. M. Flitman, Izv. Akad. Nauk SSSR, Mekh. Tverd. Tela, No. 4, 155 (1991).

4. Yu. K. Bivin, V. A. Kolesnikov, and L. M. Flitman, Izv. Akad. Nauk SSSR, Mekh. Tverd. Tela, No. 5, 181 (1982).

5. A. V. Bogdanov, A. V. Nikolaev, G. A. Skuridin, *et al.*, Kosm. Issled. **24** (4), 591 (1988).

6. I. V. Simonov, S. A. Fedotov, and O. B. Khavroshkin, Dokl. Akad. Nauk **347**, 811 (1996).

7. K. Yu. Osipenko and I. V. Simonov, Izv. Akad. Nauk, Mekh. Tverd. Tela, No. 1, 151 (2002).

8. K. Yu. Osipenko and I. V. Simonov, Izv. Akad. Nauk, Mekh. Tverd. Tela, No. 3, 87 (2001).

Translated by V. Bukhanov

===== **MECHANICS** =====

The Flow of a Viscous Fluid inside a Confuser
with Large Opening Angle

L. D. Akulenko*, D. V. Georgievskiĭ**, and S. A. Kumakshev*
Presented by Academician D.M. Klimov May 21, 2002

The formulation of the classical Jeffery–Hamel problem [1–3] on the radial steady flow of a viscous fluid in a plane confuser includes two dimensionless parameters—the opening angle and the Reynolds number. Traditionally, the case of small angles, which is of great importance in technological applications, was investigated by analytical and numerical methods. In the mathematical and natural-scientific aspects, it is interesting to solve the problem for any opening angle in a wide range of the Reynolds number. In this study, we report the new results of numerical-analytical investigation of viscous-fluid for arbitrary possible angles (including the "exotic regions" of a confuser) ranging from a half-space (a plane with an outflow aperture) to a whole space with two extremely close half-planes between which the fluid drains off. A number of the new qualitative features of the velocity and pressure profiles are established and discussed.

1. The investigation of the radial motion of a viscous incompressible fluid in a plane confuser with opening angle 2β ($0 < \beta \le \pi$) under the action of pressure applied at infinity reduces to solving the nonlinear boundary value problem with an additional condition of constant flow rate [4]:

$$y'' + a^2 y - b y^2 = \lambda, \quad 0 < x < 1, \quad y(0) = y(1) = 0;$$
$$\int_0^1 y(x)\,dx = 1, \quad a = 4\beta, \quad b = 2\beta \mathrm{Re}, \quad 0 < \mathrm{Re} < \infty. \tag{1}$$

Here, $y(x)$ is the unknown dimensionless function characterizing the profile of the radial velocity $v_r = -QV(\theta)r^{-1}$ and the transverse velocity $v_\theta \equiv 0$. The unknown function V is related to y by the relationship $y(x) = 2\beta V(\theta)$, where $\theta = \beta(2x - 1)$ is the polar angle lying in the interval $-\beta \le \theta \le \beta$ for $0 \le x \le 1$. The Reynolds number $\mathrm{Re} = \dfrac{Q}{\nu}$, where Q is the intensity of the

* *Institute for Problems in Mechanics,*
  Russian Academy of Sciences,
  pr. Vernadskogo 101-1, Moscow, 119526 Russia
** *Moscow State University,*
  Vorob'evy gory, Moscow, 119899 Russia

outflow at the point $r = 0$ and ν is the kinematic viscosity of the fluid, is given. The constants $\lambda = y''(0) = y''(1)$ and $y'(0) = \gamma$ ($y'(1) = \pm\gamma$) are unknown and should be determined for given (a, b) or (β, Re). The pressure p in the fluid and the velocity profile y are related as

$$p(r, \theta) = 2\rho Q^2 r^{-2} P(x), \quad P(x) \equiv \frac{\lambda - a^2 y(x)}{a^2 b}, \tag{2}$$

where ρ is the density and P is the pressure profile. Relation (2) indicates that the pressure becomes infinite when $\mathrm{Re} \longrightarrow 0$ ($b \longrightarrow 0$); i.e., there is a singularity, although the solution to problem (1) can be regular [4].

The classical results were obtained by analyzing elliptic integrals depending on several parameters, as well as the roots of the system of the two transcendental equations in two unknown parameters (constants of integration) [1–3]. However, these investigations are rather incomplete. It was thought that the diffuser flow ($\mathrm{Re} < 0$) is more complicated and diverse than the confuser flow ($\mathrm{Re} > 0$), because symmetric single- and multimode flow regimes (both symmetric and asymmetric about the point $x = \dfrac{1}{2}$) were known for the former. A multimode regime implies the alternation of intervals (zones) of fluid inflow and outflow for $0 < x < 1$ [1]. For the confuser Jeffery–Hamel flow, such regimes were not explicitly established.

Using a modified numerical-analytical method ensuring fast convergence, we investigated the single-mode [4] and multimode [5] confuser flows for $1° \le \beta \le 89°$ in the wide Re range $\sim 10^2 - 10^4$ ($0 \le b \le 300$) and found that, at $b \gg 1$, there is an asymptotic transition to the model of inviscid fluid, whose velocity profile is described by the Kochin formula [1, 6]

$$y(x) = 1 - \frac{6}{1 + \cosh\left[\mathrm{arccosh}\,5 + \left(\dfrac{b}{2}\right)^{1/2}(1 - |2x - 1|)\right]},$$

$$y(0) = y(1) = 0, \quad y'(0) = -y'(1) = \gamma(b) \approx \left(\frac{4b}{3}\right)^{1/2},$$

$$y''(0) = y''(1) = \lambda(b) \approx -b. \tag{3}$$

Expressions (3) have satisfactory accuracy for $b \sim 10^3$–10^4. The multimode solutions to problem (1) are "close" to Eq. (3) in a certain integral metric [5]. It was also established that the single-mode solutions are regular functions of the parameter b for $b \geq 0$ and can be found by continuing in this parameter [4]. Multimode solutions are singular functions of b in the vicinity of $b = 0$: $\gamma(b) \longrightarrow +\infty$ and $\lambda(b) \longrightarrow -\infty$ for $b \longrightarrow +0$, which results in infinite variations of the functions $y(x)$. These qualitative features take place for any opening angle β in the above range [5].

2. It is of mathematical and natural-scientific interest to solve problem (1) for the entire range of angles $0 < \beta \leq \pi$ including their "exotic" values $\beta = \dfrac{\pi}{2}$ (flow over a half-space with an outflow aperture) and π (flow in the entire space with fixed extremely close half-planes between which the fluid drains off). An increase in the angle 2β between the confuser walls leads to the significant modification of the velocity profile and new qualitative effects.

For the limiting value $b = 0$, boundary value problem (1) is linear, and its asymptotic solution is expressed in terms of a trigonometric function symmetric about the point $x = \dfrac{1}{2}$ [1, 4, 6]:

$$y(x) = 2\beta d^{-1}(\beta)[\cos 2\beta(2x - 1) - \cos 2\beta],$$
$$d(\beta) = \sin 2\beta - 2\beta \cos 2\beta,$$
$$\gamma(\beta) = 8\beta^2 d^{-1}(\beta)\sin 2\beta, \qquad (4)$$
$$\lambda(\beta) = -32\beta^3 d^{-1}(\beta)\cos 2\beta,$$
$$0 < \beta \leq \pi, \quad 0 \leq x \leq 1.$$

For clarity, curves $\gamma(\beta)$ and $\lambda(\beta)$ are shown in Fig. 1. Expressions (4) lose their meaning at $\beta = \beta^* \approx 2.247 \approx 128.7°$ (β^* is the minimum positive root of the equation $d(\beta) = 0$), and the desired solution for $b > 0$ cannot be found by perturbation methods or the continuation procedure in parameter b. The critical value β^* corresponds to a geometrically actual confuser with the opening angle larger than the straight angle $\left(\beta^* > \dfrac{\pi}{2}\right)$.

In addition, the points where these curves change sign divide the entire interval of β into five qualitatively different domains:

$$(1)\; 0 < \beta \leq \frac{\pi}{4}; \quad (2)\; \frac{\pi}{4} < \beta < \frac{\pi}{2}; \quad (3)\; \frac{\pi}{2} \leq \beta < \beta^*;$$
$$(4)\; \beta^* < \beta \leq \frac{3\pi}{4}; \quad (5)\; \frac{3\pi}{4} < \beta \leq \pi, \tag{5}$$

which correspond to different flow regimes for sufficiently small positive b values. Figure 2 shows the velocity profiles $y(x)$ (4) for $b \longrightarrow 0$ and $\beta = \dfrac{\pi}{2}$, $2.2 <$
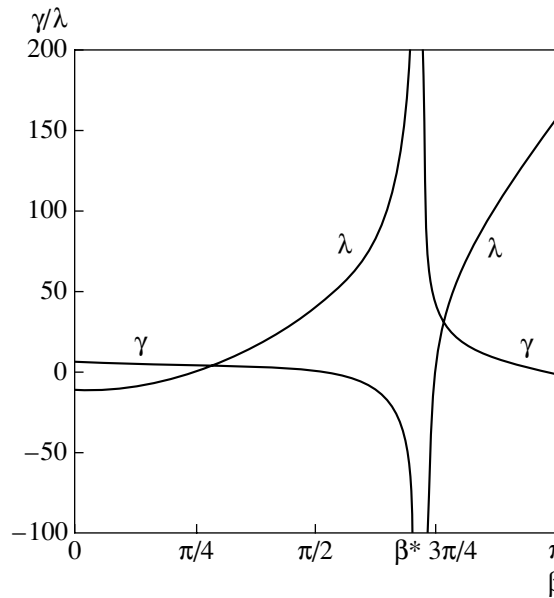

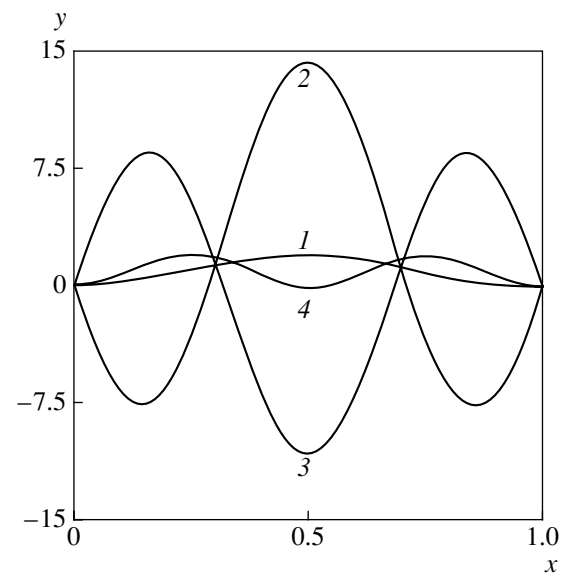**Fig. 1.** Determining parameters γ and λ vs. half-angle β at $b = 0$.

Fig. 2. Family of velocity profiles $y(x)$ for the characteristic values of β as $b \longrightarrow 0$.

β^*, $2.3 > \beta^*$, and π (curves *1–4*, respectively), which belong to domains 3–5 (5).

Single-mode solutions $y(x)$ regularly continuable in $b \geq 0$ (domain 1) are thoroughly studied [4] and have a simple form: they are convex ($\lambda < 0$) for all $b > 0$; at the limiting point, where $\beta = \dfrac{\pi}{4}$ and $b = 0$, $\lambda = 0$, but $\gamma > 0$ and $y''(x) < 0$ for $0 < x < 1$. In domain 2, these solutions are convex in the central part of the interval $0 < x < 1$, whereas they are concave at the edges, $y''(x) > 0$, because $\lambda > 0$. For all $\beta < \dfrac{\pi}{2}$, $\gamma > 0$ and $\gamma = 0$ at the lim-
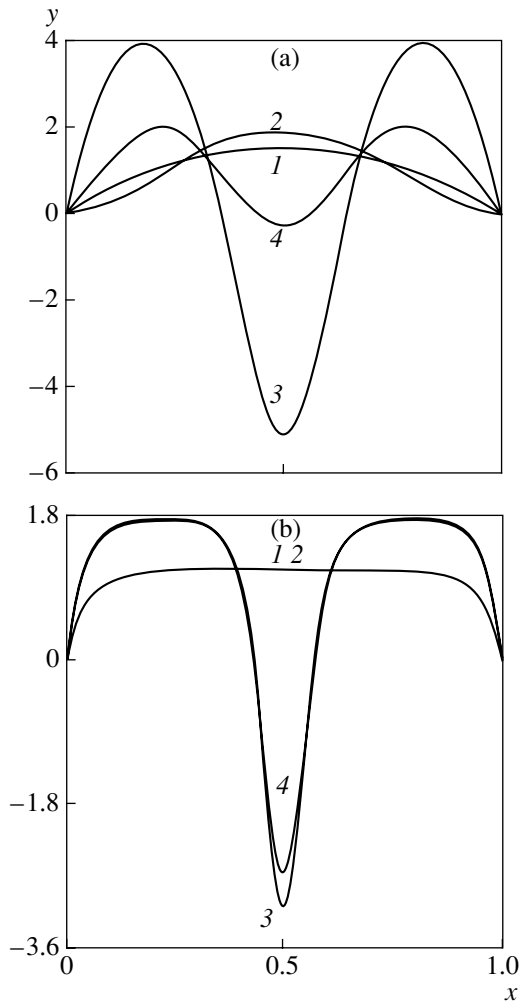

Fig. 3. (a) Evolution of velocity profiles $y(x)$ at $b = 20$ and (b) their ultimate behavior at $b = 300$ for the characteristic values of β.

iting point $\beta = \dfrac{\pi}{2} - 0$ for $b = 0$ (Fig. 2, curve *1*). With increasing parameter b (i.e., Reynolds number Re), γ remains positive and increases, whereas λ decreases and becomes negative at a certain sufficiently large b (Fig. 3, curves *1*) depending on β. Thus, the solution becomes convex. The qualitative behavior of the velocity profile $y(x)$ for the above-indicated large values of b is the same in both domains and tends to the asymptotic limit (3) when $b \longrightarrow \infty$ [4].

In domain 3, where $\beta > \dfrac{\pi}{2}$, $\gamma < 0$ (i.e., $y'(0) < 0$ and $y'(1) > 0$) and the parameter λ is positive (Fig. 2, curve *2*). This means that the intervals (zones) of reverse flows (inflow) [$y(x) < 0$] appear along the confuser walls in certain neighborhoods $x > 0$ and $x < 1$, and the outflow zone is in the central part of the confuser in a certain neighborhood $x = \dfrac{1}{2}$; i.e., the flow has three modes. Two additional symmetric points with zero flow velocity (as

at the points $x = 0$ and 1) appear; the absolute values of y' and y'' at these points are equal to $|\gamma|$ and λ, respectively. As $\beta \longrightarrow \beta^* - 0$, the values of $|\gamma|$ and λ increase indefinitely that results in the indefinite rise in the amplitudes of $y(x)$ for the above-indicated x intervals (i.e., in the outflow and inflow zones) such that the total flow rate is equal to unity according to Eqs. (1). An increase in the parameter b is accompanied by a rise in the first derivative, and, therefore, this regime goes over into the single-mode flow at a certain sufficiently large b (depending on β). In this case, the single-mode velocity profile near the walls is first close the abscissa axis, and then, with further increasing the parameter b, becomes everywhere strictly convex similar to the behavior described in [4] (Fig. 3, curves *2*).

At $b = 0$ and as $\beta \longrightarrow \beta^* - 0$, parameters γ and λ tend to $-\infty$ and $+\infty$, respectively. For $b = 0$ and $\beta = \beta^*$, problem (1) has not solution; for $b > 0$, the problem can be solved and investigated (see below). Thus, on the plane of the parameters (β, Re) or (a, b), the point $(\beta^*, 0)$ or $(4\beta^*, 0)$ is singular in the sense of solving linear boundary value problem (1).

3. The principal modification of the steady flow occurs at $\beta = \beta^*$, i.e., at the boundary between domains 3 and 4 (5). For $b = 0$ and decreasing β values such that $\beta > \beta^*$ and $\beta \longrightarrow \beta^* + 0$ (domain 4), $\gamma \longrightarrow +\infty$ and $\lambda \longrightarrow -\infty$ according to Eqs. (3); i.e., the signs of those parameters are opposite to their signs in the above case $\beta \longrightarrow \beta^* - 0$. When the opening angle of the confuser increases such that it passes through the critical value β^* another type of three-mode flow arises. In this type, in contrast to the above case of flows in domain 3, the outflow of the fluid near the confuser walls occurs symmetrically and the inflow takes place in its central part (Fig. 2, curve *3*). There are also two symmetric points ($x > 0$ and $x < 1$) with zero velocity $y(x)$. With the further rise in the opening angle, γ decreases remaining positive, whereas λ increases and is equal to zero at $\beta = \dfrac{3\pi}{4}$. The smaller the angle β, the larger amplitudes of the profile $y(x)$, which characterize the outflow and inflow zones of the fluid. With increasing parameter b, the flow remains qualitatively the same three-mode flow (Fig. 3, curves *3*) similar to the three-mode flow for small β, for which $\gamma \longrightarrow +\infty$ and $\lambda \longrightarrow -\infty$ when $b \longrightarrow +0$ [5]. In the limit $b \longrightarrow \infty$, the profile $y(x)$ asymptotically, in weak sense, tends to expression (3), which corresponds to an inviscid fluid. Thus, for large angles $\beta > \beta^*$ the three-mode flow rises reasonably in the confuser and retains for all positive b. This new hydrodynamic effect is very interesting.

The further evolution of the three-mode flow occurs in domain 5. At $b = 0$, an increase in the angle $\beta > \dfrac{3\pi}{4}$ leads to the monotonic decrease in parameter γ from $\gamma = \dfrac{9\pi^2}{2}$ at $\beta = \dfrac{3\pi}{4}$ to $\gamma = 0$ at $\beta = \pi$, (Fig. 1). Parameter λ

increases monotonically from $\lambda = 0$ at $\beta = \dfrac{3\pi}{4}$ to $\lambda = 16\pi^2$ at $\beta = \pi$. For $b \ll 1$, the amplitudes of the velocity profile, which correspond to the outflows near the walls and the inflow in the central part, decrease. At $\beta = \pi$, the inflow ceases $\left(y\!\left(\dfrac{1}{2}\right) = 0 \right)$; the velocity profile $y(x)$ attains the maximum value $y = 2$ at the points $x = \dfrac{1}{4}$ and $\dfrac{3}{4}$, i.e., at the right angles to the half-planes forming the outflow aperture (Fig. 2, curve *4*). An increase in parameter $b > 0$ results in the small shift of these outflow maxima to the edges (Fig. 3, curves *4*). For $b \gg 1$ ($b \longrightarrow \infty$), the maxima decrease and the velocity profile $y(x)$ becomes flatter near the points $x = \dfrac{1}{4}$ and $\dfrac{3}{4}$. In this case, there is a fine of a small reverse flow near the midpoint $x = \dfrac{1}{2}$; the velocity profile of this flow becomes sharper, and the minimum $y(\dfrac{1}{2})$ becomes deeper. The zone of the reverse flow contracts indefinitely, and, in the asymptotic limit, the velocity profile $y(x)$ tends to expression (3); curves *3* and *4* approach each other indefinitely. For small positive b, the outflow can somewhat increase throughout domain 5 that requires additional calculations.

The most hydrodynamically surprising and interesting feature is the presence of the critical opening angle of the confuser $2\beta^*$, at which the confuser flow qualitatively changes for $b > 0$. The solution regularly continuable in b (i.e., in Re) is single-mode at $\beta < \beta^*$ and three-mode at $\beta > \beta^*$ for any positive b [5]. For $\beta = \beta^*$ ($\beta^* = 2.246704729$ with ten significant digits), we constructed the two desired solutions at $b > 0$. For $\beta > \beta^*$, the single-mode solution has the property $\gamma \longrightarrow -\infty$ and $\lambda \longrightarrow +\infty$ at $b \longrightarrow 0$; for $\beta < \beta^*$, it goes over into the solution regularly continuable in the parameter $b \geq 0$ (domain 3). For $\beta \leq \beta^*$, the three-mode solution has the property $\gamma \longrightarrow +\infty$ and $\lambda \longrightarrow -\infty$ at $b \longrightarrow 0$; for $\beta > \beta^*$, it is regularly continuable in b, i.e., in Re (domain 4).

The main computational result is the high-accuracy [with a relative error of $O(10^{-9})$] construction of curves γ and λ as functions of parameter b for the β values of interest (Fig. 4). The corresponding profiles of velocity $y(x)$ and pressure $P(x)$ can be found by integrating the Cauchy problem according to Eqs. (1) and (2).

Thus, steady flows of a viscous fluid in a plane confuser with arbitrary opening angle, which are regularly continuable in Re ≥ 0, were quite completely analyzed. For angles $0 < \beta < \pi/2$, multimode solutions with quantities γ and λ infinite at $b \to 0$ were established and constructed earlier [5]. For hydrodynamic applications, the investigation of multimode solutions for confuser opening angle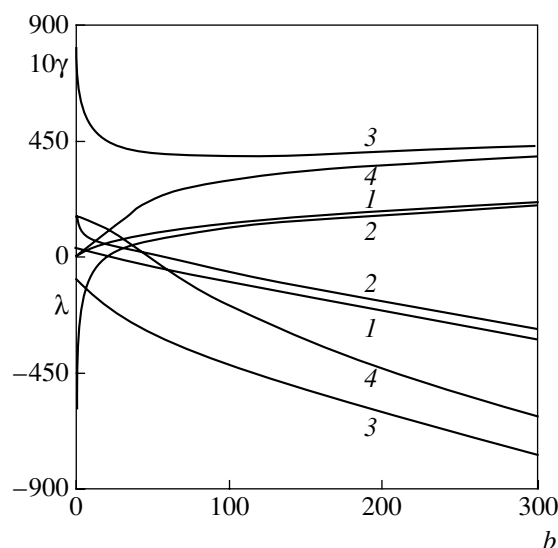s $\pi \leq 2\beta \leq 2\pi$ and moderate Re values ~1–100 can be of certain interest. The effective investigation of the viscous fluid flows is important both itself and for the numerical-analytical solution of more complicated perturbed problems of the deformation of viscoplastic media [6] and the problems of heat and mass transfer, where viscous flows can be considered as unperturbed reference motions.

Fig. 4. Determining parameters γ and λ vs. b for the characteristic values of β.

ACKNOWLEDGMENTS

REFERENCES

1. N. E. Kochin, I. A. Kibel', and N. V. Roze, *Theoretical Hydromechanics* (Fizmatlit, Moscow, 1963; Interscience, New York, 1964), Chap. 2.

2. L. G. Loitsyanskiĭ, *Mechanics of Fluid and Gas* (Nauka, Moscow, 1978).

3. G. K. Batchelor, *An Introduction to Fluid Dynamics* (Cambridge Univ. Press, Cambridge, 1967; Mir, Moscow, 1973).

4. L. D. Akulenko, D. V. Georgievskiĭ, S. A. Kumakshev, and S. V. Nesterov, Dokl. Akad. Nauk **374** (1), 44 (2000) [Dokl. Phys. **45**, 467 (2000)].

5. L. D. Akulenko, D. V. Georgievskii, and S. A. Kumakshev, Dokl. Akad. Nauk **383** (1), 46 (2002) [Dokl. Phys. **47**, 219 (2002)].

6. D. V. Georgievskii, *Stability of Deformation Processes in Viscoplastic Bodies* (URSS, Moscow, 1998).

Translated by Yu. Vishnyakov

================= **MECHANICS** =================

On the Power Law of Catastrophic Floods

V. I. Naĭdenov* and I. A. Kozhevnikova**

A growth in the number of catastrophes is characteristic of modern Russia, especially in recent years [1]. According to the data of the Russian Ministry of Emergency Situations, 2877 emergency events associated with natural dangerous processes were recorded in the last ten years (1990–1999). Among these events, catastrophic phenomena caused by floods amounted to 19% of the total number.

United States statistics of tornado, earthquakes, floods, and hurricanes occurred in the past century show that the data of observations lie in straight lines corresponding, with a reasonably good accuracy, to perfect power-low statistics [2].

From the standpoint of random-process theory, this implies that the probability-density distributions of random quantities characterizing floods (water levels in a river, volumes of high-water outflow, maximum water discharge, etc.) are long-tail distributions. Thus, the probability of catastrophic floods turns out to be much higher than follows from the assumption on the Gaussian distribution law.

Below, we show how long-tail distributions arise in hydrological processes.

ON THE PHYSICAL MECHANISM OF THE POWER LAW

We consider the equation of water balance in a river basin

$$\frac{dW}{dt} = \bar{P} - \bar{E} - Q + \sigma\xi(t), \tag{1}$$

where W and Q are the water content and the river outflow, respectively, $\bar{P}$ and $\bar{E}$ are the many-year averaged values of rainfall and evaporation, $\xi(t)$ is the delta-correlated random process of fluctuations of rainfall and evaporation, and σ is the intensity of this process.

———————————
 * Institute of Water Problems,
   Russian Academy of Sciences, Mytishchi,
   Moscow oblast, Russia
** Moscow State University,
   Vorob'evy gory, Moscow, 119899 Russia

We now assume that the outflow and the water content of the basin are related to each other by a nonlinear (hyperbolic) dependence

$$\frac{Q}{\tilde{P}} = \frac{\bar{\mu}W}{W_* - W}, \quad \tilde{P} = \bar{P} - \bar{E}, \quad 0 \leq W < W_*, \tag{2}$$
$$0 \leq Q < \infty, \quad \bar{\mu} < 0,$$

where $\tilde{P}$ is the effective value of rainfall and W_* is a certain characteristic water content of the basin.

The physical mechanism of an increase in the outflow with a growth of the water contents is the following. First, the larger the volume of surface water, soil water, underground water, and waters of lakes and swamps composing the water content of a basin, the higher is the potential energy of these waters. Second, according to the Newtonian law of a linear relation between the stress tensor and the velocity tensor in a viscous fluid, the energy dissipation in the case of the water motion in a moistened basin is much lower than in a dry basin (this is the reason that ensures an abrupt increase in the filtration coefficient of water with a growth of the soil moisture). Thus, an increase in the potential energy of water and a decrease in the resistance to its motion in the river basin lead to a nonlinear increase in the water discharge.

We introduce the dimensionless quantities

$$X = \frac{Q}{\tilde{P}}, \quad \bar{\sigma} = \frac{\sigma}{\bar{\mu}W_*}, \quad T = \frac{\bar{\mu}W_*}{\tilde{P}},$$
$$\beta = 2\left(1 + \frac{1}{\bar{\sigma}^2 T}\right).$$

Replacing the variables in (1) according to formula (2), we obtain the stochastic differential equation (SDE) with respect to the outflow X_t

$$dX_t = T^{-1}(1 - X_t)(X_t + \bar{\mu})^2 dt + \bar{\sigma}(X_t + \bar{\mu})^2 dW_t, \tag{3}$$

where W_t is the standard Wiener process.

SDE (3) has the following important feature: the action of an external noise depends on a system state. Such a noise is multiplicative and represents the physical cause of a wide class of noise-induced transitions [3].

In the theory of SDE [3], the necessity to interpret Eq. (3) in terms of the Stratanovich theory is proved.

In this case, the Fokker–Planck–Kolmogorov (FPK) equation with respect to the probability density $p(x, t)$ takes the form

$$\frac{\partial p(x, t)}{\partial t} = -\frac{\partial}{\partial x}\left[\frac{(1 - x)(x + \bar{\mu})^2}{T} + \bar{\sigma}^2(x + \mu)^3\right]p(x, t)$$
$$+ \frac{\bar{\sigma}^2}{2}\frac{\partial^2}{\partial y^2}[(x + \bar{\mu})^4 p(x, t)].$$

(4)

It is easy to obtain a time-independent solution to (4) $\left(\frac{\partial p}{\partial t} = 0\right)$ for the one-dimensional probability density

$$p_s(x) = \begin{cases} C(x + \bar{\mu})^{-\beta}\exp\left(-\frac{(\beta - 2)(\bar{\mu} + 1)}{x + \bar{\mu}}\right), & x > 0 \\ 0, & x \leq 0. \end{cases}$$

(5)

The parameter C is determined from the normalization conditions

$$C = [(\beta - 2)(\bar{\mu} + 1)]^{\beta - 1}\left[\int_0^{\frac{(\beta - 2)(\bar{\mu} + 1)}{\bar{\mu}}} u^{\beta - 1}e^{-u}du\right]^{-1}.$$

The most probable mode of the distribution is $x_{\text{mod}} = \frac{\beta - 2 - 2\bar{\mu}}{\beta}$. For $\beta > 2(1 + \bar{\mu})$, the mode exists; for $\beta \leq 2(1 + \bar{\mu})$, it does not. Thus, the behavior of the nonlinear nonequilibrium dynamic set (1)–(3) when the critical level of rainfall noise is exceeded ($\bar{\sigma} = \sqrt{(\bar{\mu}T)^{-1}}$) radically changes. Therefore, the interaction between the nonlinear outflow dynamics and the random nature of the environment (climatic noise) leads, under certain conditions, to an essential reconstruction of the steady outflow regime.

The most important feature of this interaction is the appearance of the Pareto component $(x + \bar{\mu})^{-\beta}$ in the probability-density distribution for a river outflow. For large values of x, the outflow dynamics corresponds to the power law with the exponent β. It is of interest that the exponent σ abruptly decreases with the rainfall-noise intensity β and, for $2 < \beta < 3$, the variance of the random outflow process becomes infinitely large. It

should be noted that distribution (5) has no moments of the [β]th order ([β] is the integer part of β). For example, for $\tilde{P} = 0.4$ m year^{-1}, $W^* = 4$ m, $\sigma = 0.9$ m year$^{-0.5}$, and $\bar{\mu} = 1$, the exponent $\beta = 6$, and the distribution obtained has no moments of the sixth, seventh, and higher orders. Using the theory developed in [3, 4], it is possible to show that the time-independent solution $p(y, t)$ to the FPK equation converges to $p_s(y)$ as $t \longrightarrow \infty$, whence follows the global asymptotic stability of the steady state.

For a random process of the accumulation of the water content W_t, the boundary W_* is natural, and the probability to attain it is zero. For the water outflow, the natural boundary is infinity. Thus, SDE (3) for the outflow is mathematically correct.

Physically, the appearance of the power law is explained by a nonlinear dependence of the outflow on the basin water content. The two most important factors of the outflow, namely, an increase in the water content and a decrease in the resistance to the water motion in the basin, are mutually dependent, and the random process X_t already cannot be Gaussian. Let us assume that abundant rainfall has occurred in the river basin. In this case, the resistance to the water motion decreases so that not only this rainfall will drain down to the river but also the rainfall from previous rains, which earlier failed to do this due to a high frictional resistance. The mathematical formalization of this well-known hydrological phenomenon leads to power laws for floods and high waters. We call attention to the fact that the rainfall follows the Gaussian law, and, therefore, the distribution long tail is formed by the hydrophysical processes when collecting water.

We emphasize once more that the previous rainfall takes part in the formation of the outflow at the present moment of time.

Therefore, the catastrophic floods are a result of the nonlinear interaction between underground water and surface water. The isotopic composition of water coming to the river bed at the moment of a catastrophe must strongly differ from that in an atmospheric rainfall (e.g., the concentration of the heavy hydrogen isotope tritium is quite different).

For example, in the early spring of 1997, northern plains (Midwest, USA) were covered by a destructive flood. Towns situated on the Red River, such as Grand Fork and Northern Dakota, were completely submerged as a result of this flood, which totally paralyzed these towns and left entire regions under water. During showers of 1996, the towns situated on the Red River got a record quantity of rainfall. In winter, the water was frozen before draining down to the ocean. During the long winter, once again, a record amount of snow fell, which began to thaw when a warming began. However, not only the snow fallen in winter began to thaw,

but also the frozen rainwater remaining from the previous rain season. As a result, too much water, which could not be localized in springs and rivers (e.g., in the Red River), has been accumulated, and, as a consequence, vast areas of dry land were flooded.

STATISTIC OF MAXIMUM WATER DISCHARGES AND LEVELS

We have performed statistical analysis of a large number of time series for maximum water levels in rivers, outflow volumes during the high water, and maximum water discharges. We gave special emphasis to the analysis of catastrophic floods in St. Petersburg, because detailed physical models were developed for this phenomenon, and this was a good possibility to compare the probabilistic and hydrodynamic maximum water levels in the Neva River near the Institute of Mining (Fig. 1).

We consider the sampling X_1, X_2, …, X_n from the general set of mutually independent and identically distributed random quantities, which can obey one of two distributions and satisfies the condition that the sampling average is equal to 1. As the distributions we choose:

gamma distribution

$$p_{\Gamma}(x) = \begin{cases} \dfrac{\mu^{\mu} x^{\mu-1} e^{-\mu x}}{\Gamma(\mu)}, & x > 0 \\ 0, & x \le 0; \end{cases} \tag{6}$$

and power distribution
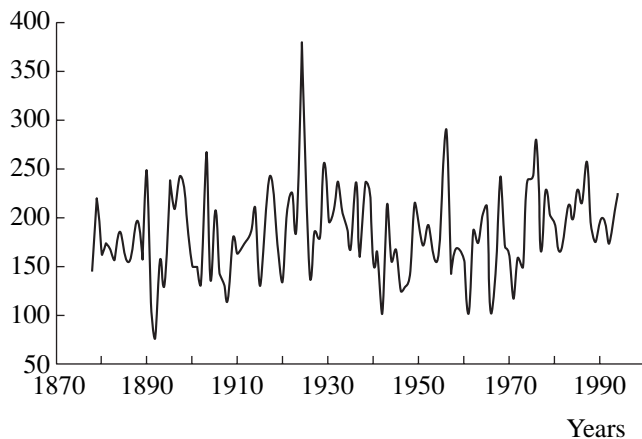
Maximum levels of the Neva River, cm of the BS

Fig. 1. Maximum water level of the Neva River near the Institute of Mining (1878–1994).

$$p_{\text{pow}}(x) = \begin{cases} \dfrac{(\beta-2)^{\beta-1} e^{-\frac{\beta-2}{x}}}{\Gamma(\beta-1) x^{\beta}}, & x > 0 \\ 0, & x \le 0. \end{cases} \tag{7}$$

Here, $\mu > 0$, $\beta > 2$, are the distribution parameters, and $\Gamma(\cdot)$ is the Euler gamma function. The mathematical expectation for both distributions is $EX = \int\limits_0^{\infty} x p(x) dx = 1$; the asymmetry coefficient c_s and the standard derivation σ are linked by the relationships $c_s^{\Gamma} = 2\sigma_{\Gamma}$ for the gamma distribution and $c_s^{\text{pow}} = 2\sigma_{\text{pow}}$ for the power distribution (when the second moment exists).

We estimate the parameters μ and β by the maximum-likelihood method [4]. The logarithmic likelihood functions for distributions (6) and (7) are expressed, respectively, as

$$\ln(p_{\Gamma}(X_1, X_2, …, X_n)) = (\mu-1) \sum_{i=0}^{n} \ln X_i - \mu$$
$$+ n\mu \ln\mu - n \ln\Gamma(\mu),$$

$$\ln(p_{\text{pow}}(X_1, X_2, …, X_n)) = -(\beta-2) \sum_{i=1}^{n} \frac{1}{X_i}$$
$$+ n(\beta-1)\ln(\beta-2) - \beta \sum_{i=1}^{n} \ln X_i - n\ln\Gamma(\beta-1).$$

The maximum-likelihood equations for each distribution have the form

$$\frac{d\ln\Gamma(\mu)}{d\mu} - \ln\mu = \frac{1}{n}\sum_{i=1}^{n} \ln X_i,$$

$$-\frac{d\ln\Gamma(\beta-1)}{d\beta} + \frac{\beta-1}{\beta-2} + \ln(\beta-2) \tag{8}$$

$$= \frac{1}{n}\sum_{i=1}^{n} \frac{1}{X_i} + \frac{1}{n}\sum_{i=1}^{n} \ln X_i.$$

Equations (8) were numerically solved using the Stirling asymptotic formula for the gamma function.

Both models under consideration are regular [4]. In this case, the estimates of the maximum likelihood are unbiased, consistent, and asymptotically normal. Their variance attains the lowest value in the class of unbiased estimates and is expressed in terms of the Fisher information:

$$\sigma_\Gamma^2 = -\frac{1}{n\int\limits_0^\infty \dfrac{d^2\ln p(x,\mu)}{d\mu^2}p(x,\mu)dx}$$

$$= \frac{1}{n\left[\dfrac{d^2\ln\Gamma(\mu)}{d\mu^2} - \dfrac{1}{\mu}\right]},$$

$$\sigma_{\text{pow}}^2 = -\frac{1}{n\int\limits_0^\infty \dfrac{d^2\ln p(x,\beta)}{d\beta^2}p(x,\beta)dx}$$

$$= \frac{1}{n\left[\dfrac{d^2\ln\Gamma(\beta-1)}{d\beta^2} - \dfrac{(\beta-3)}{(\beta-2)^2}\right]}.$$

(9)

We introduce the probability of exceeding the value X_* for the gamma distribution and power distribution, respectively:

$$P_\Gamma(X > X_*) = 1 - \frac{1}{\Gamma(\mu)}\int\limits_0^{\mu X_*} x^{\mu-1}e^{-x}dx,$$

$$P_{\text{pow}}(X > X_*) = \frac{1}{\Gamma(\beta-1)}\int\limits_0^{\frac{\beta-2}{X_*}} x^{(\beta-2)}e^{-x}dx.$$

(10)

For maximum water discharges in rivers (Table 1), we present the estimates of parameters for each distribution, which were obtained by numerically solving Eqs. (8) and their bilateral confidence intervals at the significance level of 0.05 (i.e., the probability that the true value of a parameter does not lie within the indicated interval is 0.05).

For maximum water levels in the Neva River (1878–1994), the following estimates were obtained: $\breve\mu = 15.906$ and $\breve\beta = 16.283$. For these estimates, the confidence intervals at the confidence level of 0.95 are equal to (11.529; 20.283) and (12.359; 20.207), respectively.

Table 1. Characteristics of distributions for maximum water discharges

| River, observation point (sampling size)	Estimate of the distribution parameter (confidence interval)		Probabilities of exceeding the value X_*					
	$\breve\beta$ ($\breve\beta - 2\sigma_{\text{pow}}$; $\breve\beta + 2\sigma_{\text{pow}}$)	$\breve\mu$ ($\breve\mu - 2\sigma_\Gamma$; $\breve\mu + 2\sigma_\Gamma$)	2		3		4	
			P_{pow}	P_Γ	P_{pow}	P_Γ	P_{pow}	P_Γ
Zapadnaya Dvina River, Daugavpils (80)	8.90 (6.77; 11.14)	7.64 (5.27; 10.01)	0.0274	0.0114	0.0030	7×10^{-5}	5×10^{-4}	3.6×10^{-6}
Danube River (July), Stvor Orsova (Romania) (149)	11.96 (9.69; 14.23)	11.45 (8.83; 14.07)	0.0058	0.0010	0.00011	9.6×10^{-8}	4.5×10^{-6}	5.3×10^{-9}
Danube River (August) (149)	15.90 (12.71; 19.09)	14.65 (11.29; 18.01)	0.0321	0.0155	0.0042	0.00017	0.00082	1.3×10^{-5}
Tura River, Tyumen (70)	2.83 (2.59; 3.08)	1.52 (1.05; 1.98)	0.0885	0.1078	0.0456	0.0242	0.0279	0.0025
Yangtze River (November), Haikou [30.58°N, 114.28°W] (113)	27.56 (20.76; 34.36)	27.57 (20.22; 34.92)	0.00049	0.00015	–	–	–	–
Primorskiĭ-Kraĭ rivers								
Code 79 695 (67)	3.59 (3.45; 3.73)	2.92 (1.96; 3.88)	0.0854	0.0639	0.0360	0.0067	0.0187	0.00059
Code 78 141 (87)	6.14 (4.93; 7.35)	5.63 (3.97; 7.29)	0.0510	0.0233	0.0110	0.00053	0.0033	7.2×10^{-5}
Code 78 138 (58)	5.36 (4.17; 6.55)	4.20 (2.70; 5.70)	0.0606	0.0399	0.0160	0.0024	0.0056	0.00063
Code 78 144 (57)	6.21 (4.69; 7.72)	5.18 (3.29; 7.06)	0.0627	0.0275	0.0172	0.00085	0.0063	0.00014
Code 78 252 (51)	2.98 (2.97; 2.99)	1.86 (1.18; 2.54)	0.0904	0.1181	0.0451	0.0413	0.0270	0.0251
Code 01 801 (58)	20.19 (13.47; 26.90)	19.47 (12.27; 26.67)	0.0023	0.00021	1.6×10^{-5}	2.8×10^{-9}	2.7×10^{-7}	1.8×10^{-9}
Code 05 254 (55)	10.81 (7.51; 14.11)	10.76 (6.72; 14.81)	0.0178	0.0038	0.0012	3.5×10^{-6}	0.00014	5.3×10^{-8}
Code 05 287 (58)	8.71 (6.28; 11.15)	8.48 (5.39; 11.57)	0.0285	0.0084	0.0032	3.1×10^{-5}	0.00057	1.1×10^{-6}

Probability density distribution function
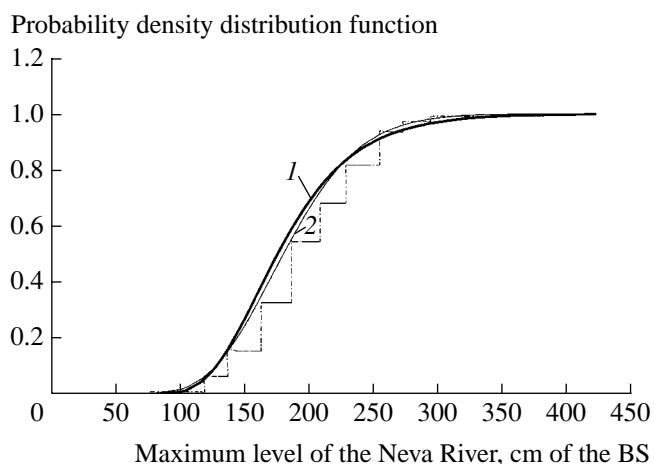
Fig. 2. Functions of the (*1*) power distribution and (*2*) gamma distribution both corresponding to the sampling distribution function (broken line) for the water level in Neva River [8]. $\breve{\beta} = 16.283$ and $\breve{\mu} = 15.906$.

The probabilities of exceeding the given level calculated from formulas (10) are displayed in Table 2 for the maximum levels in the Neva River.

On the basis of the analysis of various goodness-of-fit tests (Figs. 2 and 4), we can conclude that both gamma and power distributions satisfactorily correspond to the measurement data. However, the probabilities of catastrophic floods calculated on the basis of these distributions are substantially different (Fig. 3).

For example, according to the power distribution, the famous St. Petersburg flood, which occurred on November 19, 1824 (the Neva water level was 421 cm of the Baltic System (BS)), must take place once every 667 years. According to the gamma distribution, this event is virtually impossible (once every 22 222 years).

The flood which occurred on September 23, 1924 (the Neva water level of 380 cm of the BS) has a probability of 0.0039 (once every 256 years) according to the power distribution and 0.00036 (once every 2777 years) according to the gamma distribution; i.e., again, it is virtually impossible. However, these events did take place.

The flood of 1954 in the Yangtze River in China has a probability four times higher according to the power distribution (once every 167 years) than according to the gamma distribution (once every 667 years).

A further example. The probability of exceeding the catastrophic level of the flood in 1931 in the Zapadnaya Dvina River near Vitebsk is equal to 0.0144 (once every 69 years) and exceeds the probability according to the gamma distribution equal to 0.0032 (once every

Table 2. Probabilities of exceeding the maximum water level in the Neva River near the Institute of Mining

Level, cm of the BS	Probabilities of exceeding the water level		Level, cm of the BS	Probabilities of exceeding the water level		Level, cm of the BS	Probabilities of exceeding the water level	
	power distribution	gamma distribution		power distribution	gamma distribution		power distribution	gamma distribution
160	0.632	0.673	250	0.097	0.084	340	0.010	0.0024
165	0.593	0.630	255	0.086	0.071	345	0.0092	0.0019
170	0.547	0.586	260	0.076	0.060	350	0.0081	0.0015
175	0.501	0.540	265	0.067	0.050	355	0.0072	0.0012
180	0.460	0.498	270	0.059	0.042	360	0.0063	0.00095
185	0.417	0.454	275	0.052	0.035	365	0.0056	0.00075
190	0.379	0.412	280	0.046	0.029	370	0.0050	0.00059
195	0.342	0.371	285	0.041	0.024	375	0.0044	0.00046
200	0.308	0.333	290	0.036	0.020	380	0.0039	0.00036
205	0.277	0.297	295	0.032	0.016	385	0.0035	0.00028
210	0.248	0.264	300	0.028	0.013	390	0.0031	0.00022
215	0.221	0.232	305	0.025	0.011	395	0.0028	0.00017
220	0.197	0.204	310	0.022	0.009	400	0.0024	0.00013
225	0.176	0.178	315	0.019	0.0072	405	0.0022	0.00010
230	0.157	0.155	320	0.017	0.0058	410	0.0019	0.000079
235	0.140	0.134	325	0.015	0.0047	415	0.0017	0.000061
240	0.123	0.114	330	0.013	0.0038	420	0.00154	0.000047
245	0.109	0.098	335	0.012	0.0030	421	0.00151	0.000045

Probability densities for power
and gamma distributions

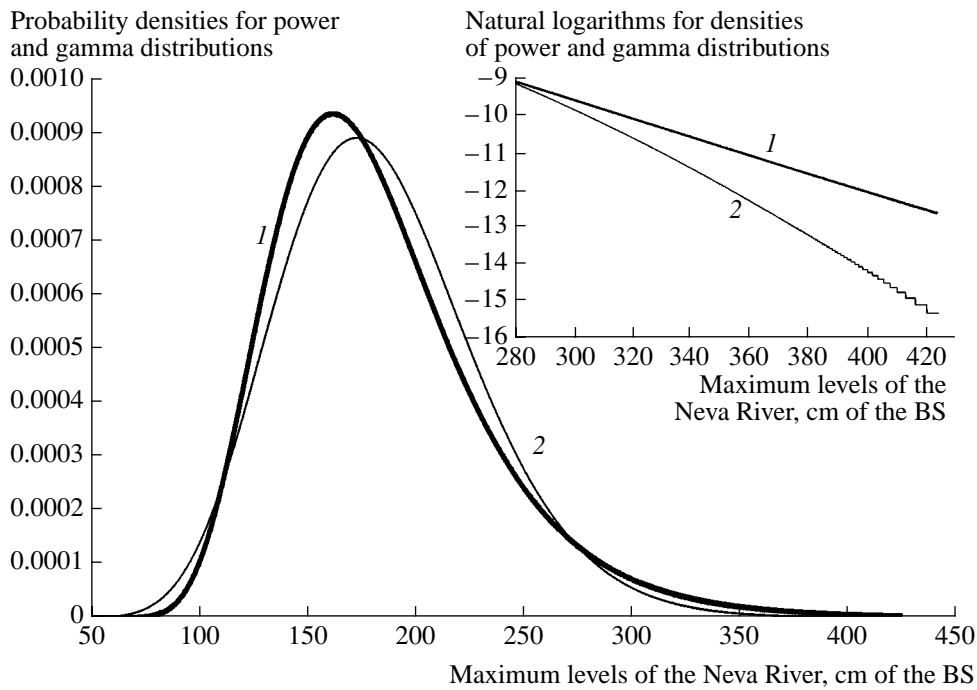Natural logarithms for densities
of power and gamma distributions

Fig. 3. Probability densities for (*1*) power distribution and (*2*) gamma distribution in the natural series of maximum levels in the Neva River (1878–1994). In the insert, the behavior of tails for the (*1*) power distribution and (*2*) gamma distribution in the region of catastrophic floods is shown.

312 years) by a factor of 4.5. It should be emphasized that the catastrophic rise of the water level in the Zapadnaya Dvina River was repeated in 1951.

The probability of exceeding the maximum water discharge in Missouri River in 1951 (12606 m^3/s) is 0.026 (once every 38 years) according to the power distribution and to 0.0055 (once every 181 years) according to the gamma distribution, i.e., five times lower.

Thus, the power-low statistic indicates that the catastrophic floods occurring on our planet are not such outstanding events and have a sufficiently high probability, which cannot be ignored.

Associated with the hydrological substantiation of certain projects destined to protect St. Petersburg and its nearest suburbs against floods, extensive investigations were carried out on the problem of predicting the maximum water levels of the Neva River [5–7].

We emphasize that, for calculating the probabilities of exceeding the levels cited in Table 3, we used the statistical data on the Neva River maximum levels only for the period of 1878–1994. The statistic of St. Petersburg floods for the period of 1703–1994 turned out to be well described by the power law, whose parameters have been calculated for a relatively short run of observations. This comparison shows that the concept of a low information content of serial floods is invalid.

We compared the results of these investigations and of the calculations using the statistical models (see Table 3). This comparison shows that the power distri-

bution well corresponds to the hydrodynamic models of floods.

If we introduce a new random value, for example, the material damage caused by floods, it is evident that this damage exponentially depends on physical scales of a disaster (water level or water discharge). From probability theory, it is well known that the distribution density of this quantity has a much longer tail than the distribution density for the maximum water level or for
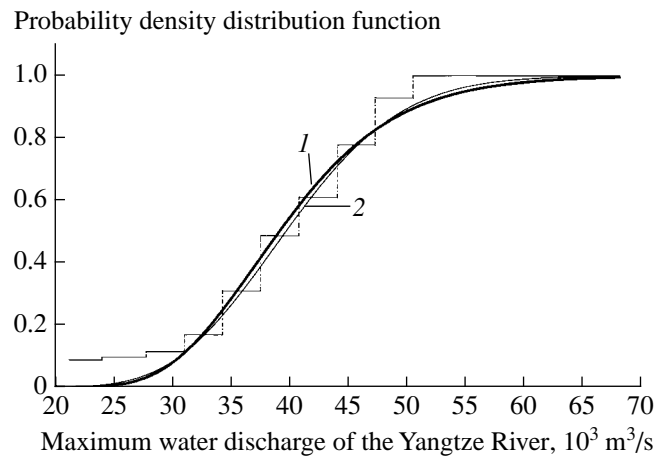
Probability density distribution function

Fig. 4. Functions of (*1*) power distribution and (*2*) gamma distribution both corresponding to the sampling distribution function (broken line) for the maximum water level in the Yangtze river (China); $\breve{\beta} = 27.56$ and $\breve{\mu} = 27.57$.

Table 3. Recurrence of water levels in the Neva River near the Institute of Mining

Recurrence of water levels	Hydrodynamic models	Power distribution	Gamma distribution
Once every: 10000 years	540	548	406
Once every: 1000 years	475	439	359
Once every: 100 years	345	341	307
Once every: 20 years	257	275	265
Once every: 5 years	215	219	220

the water discharge. This explains the power shape of histograms illustrating distributions of the number of victims and homeless people caused by floods of the last decades of the past century.

For example, let a damage value be $Y = X^m$ ($m \gg 1$). Then, the distribution density of this quantity has the form for $y = 0$,

$$p(y) = \frac{(\beta - 2)^{\beta - 1} \exp\left(-\frac{\beta - 2}{\sqrt[m]{y}}\right)}{m\Gamma(\beta - 1) y^{\frac{\beta - 1}{m} + 1}}.$$

The statistical estimates show that $\frac{\beta - 1}{m} < 1$.

ACKNOWLEDGMENTS

REFERENCES

1. V. I. Osipov, Vestn. Ross. Akad. Nauk **71**, 291 (2001).
2. G. G. Malinetskiĭ and S. P. Kurdyumov, Vestn. Ross. Akad. Nauk **71**, 210 (2001).
3. W. Horsthemke and R. Lefever, *Noise-Induced Transitions. Theory and Applications in Physics, Chemistry, and Biology* (Springer, Heidelberg, 1984; Mir, Moscow, 1987).
4. G. I. Ivchenko and Yu. I. Medvedev, *Mathematical Statistics* (Vyssh. Shkola, Moscow, 1992).
5. R. A. Nezhikhovskiĭ, *Problems of Hydrology of the Neva River and the Neva Gulf* (Gidrometeoizdat, Leningrad, 1988).
6. K. S. Pomeranets, Priroda, No. 10, 9 (1993).
7. K. S. Pomeranets, Meteorol. Gidrol., No. 8, 105 (1999).
8. *Goodness-of-Fit Techniques*, Ed. by R. B. D'Agostino and M. A. Stephens (M. Dekker, New York, 1986).

Translated by V. Bukhanov